5^{th} ORDER SIGMA DELTA MEMS ACCELEROMETER SYSTEM WITH ENHANCED LINEARITY

A THESIS SUBMITTED TO
THE GRADUATE SCHOOL OF NATURAL AND APPLIED SCIENCES
OF
MIDDLE EAST TECHNICAL UNIVERSITY

BY

ULAŞ AYKUTLU

IN PARTIAL FULFILLMENT OF THE REQUIREMENTS
FOR
THE DEGREE OF MASTER OF SCIENCE
IN
ELECTRICAL AND ELECTRONICS ENGINEERING

SEPTEMBER 2015

Approval of the thesis:

5th ORDER SIGMA DELTA MEMS ACCELEROMETER SYSTEM WITH ENHANCED LINEARITY

submitted by **ULAŞ AYKUTLU** in partial fulfillment of the requirements for the degree of **Master of Science in Electrical and Electronics Engineering Department**, **Middle East Technical University** by,

Prof. Dr. Gülbin Dural Ünver _____
Dean, Graduate School of **Natural and Applied Sciences**

Prof. Dr. Gönül Turhan Sayan _____
Head of Department, **Electrical and Electronics Eng.**

Prof. Dr. Tayfun Akın _____
Supervisor, **Electrical and Electronics Eng. Dept., METU**

Examining Committee Members

Prof. Dr. Haluk Külah _____
Electrical and Electronics Eng. Dept., METU

Prof. Dr. Tayfun Akın _____
Electrical and Electronics Eng. Dept., METU

Assist. Prof. Dr. Kıvanç Azgın _____
Mechanical Eng. Dept., METU

Assist. Prof. Dr. Mehmet Ünlü _____
Electrical and Electronics Eng. Dept., YBU

Assist. Prof. Dr. Mahmud Yusuf Tanrıkulu _____
Electrical and Electronics Eng. Dept., ADANA STU

Date: _____

I hereby declare that all information in this document has been obtained and presented in accordance with academic rules and ethical conduct. I also declare that, as required by these rules and conduct, I have fully cited and referenced all referenced material and results that are not original to this work.

Name, Surname: Ulaş Aykutlu

Signature:

ABSTRACT

5th ORDER SIGMA DELTA MEMS ACCELEROMETER SYSTEM WITH ENHANCED LINEARITY

Aykutlu, Ulaş

M.S., Department of Electrical and Electronics Engineering

Supervisor: Prof. Dr. Tayfun Akın

September 2015, 101 pages

This thesis reports the linearity enhanced 5th order sigma delta MEMS accelerometer readout circuit utilizing varying gap type capacitive MEMS accelerometer sensor. While varying gap type capacitive MEMS accelerometers provide high sensitivity, high reliability and high shock tolerance suitable for navigation grade applications, these types of mechanical sensors suffer from the non-linear input to output relation even in the closed loop operation due to the limited loop gain. Thus, this research aims to improve the linearity performance and eliminate the non-linear behavior of mechanical sensor by employing PI controller in the sigma delta interface circuit designed previously in METU-MEMS Center. In order to achieve this goal, firstly the non-linear behavior of the capacitive MEMS accelerometer is examined. Then, MATLAB-Simulink simulations are performed to demonstrate the enhancement in the linearity performance of the accelerometer system taking advantage of PI controller in the loop. Programmable PI controller which enables integration of various MEMS accelerometer with the readout circuit is implemented carefully using XFab 0.35µm CMOS process to guarantee low noise and bias instability while

providing enhanced linearity performance. Designed readout is integrated with the MEMS accelerometer which is fabricated at METU-MEMS Center in a 16-pin metal package to perform system level performance tests.

Measurement results show that the accelerometer system taking advantage of PI controller achieves non-linearity below 150 ppm even for the low loop gain configurations. Compared to the accelerometer system utilizing only P-controller, test results demonstrate that non-linearity is highly suppressed up to 20 times with the use of PI controller. Also, implemented accelerometer system accomplishes 12.5 $\mu g/\sqrt{Hz}$ noise floor, 5.8 μg bias instability, 792 $\mu g/°C$ bias temperature coefficient, below 1 mg turn on/off bias repeatability and ±29 g full scale range which verify high performance while providing enhanced linearity.

Keywords: Sigma Delta Modulator, Capacitive Readout, CMOS Controller Design, High Linearity Accelerometer

ÖZ

DOĞRUSALLIĞI GELİŞTİRİLMİŞ 5. DERECE SİGMA DELTA MEMS İVMEÖLÇER SİSTEMİ

Aykutlu, Ulaş

Yüksek Lisans, Elektrik ve Elektronik Mühendisliği Bölümü

Tez Yöneticisi: Prof. Dr. Tayfun Akın

Eylül 2015, 101 sayfa

Bu tez değişken açıklığa sahip sığasal MEMS ivmeölçer sensörü içeren doğrusallığı geliştirilmiş 5. derece sigma delta MEMS ivmeölçer okuma devresini anlatmaktadır. Değişken açıklığa sahip sığasal MEMS ivmeölçerler yüksek duyarlılık, güvenilirlik ve darbelere karşı dayanıklı olması itibariyle seyrüsefer uygulamalar için uygun olmasına rağmen, bu tip mekanik sensörler doğrusal olmayan girdi çıktı ilişkisine sahip olması nedeniyle kapalı döngü içerisinde çalıştırılsalar dahi düşük döngü kazancından ötürü performans kaybına uğrarlar. Bu sebeple bu araştırmanın amacı daha önce ODTÜ-MEMS Merkezinde tasarlanan sigma delta arayüz devresine orantılı-entegral kontrolcüsü ekleyerek ivmeölçerin doğrusallık performansını iyileştirmek ve mekanik sensörden kaynaklanan doğrusallık kaybını ortadan kaldırmaktır. Bu amaçla ilk olarak değişken açıklığa sahip sığasal ivmeölçerin doğrusallık özelliği çalışılmıştır. Sonrasında orantılı-entegral kontrolcüsü içeren ivmeölçer sistemindeki doğrusallık performansının iyileştiğini göstermek için MATLAB-Simulink simulasyonları yapılmıştır. Çeşitli ivmeölçerlerin okuma devresiyle birleştirilmesine olanak sağlayan orantılı-entegral kontrolcüsü, XFab

0.35 µm CMOS teknolojisi ile düşük gürültü, düşük offset kararsızlığı ve yüksek doğrusallık sağlayacak şekilde tasarlanmış ve ürettirilmiştir. Geliştirilen yeni okuma devresi ODTÜ-MEMS Merkezinde üretilen ivmeölçer ile 16 bacaklı metal paket içinde performans testleri yapılmak üzere birleştirilmiştir.

Testler, orantılı-entegral kontrolcüsü içeren ivmeölçer sisteminde düşük döngü kazancında dahi 150 ppm altında doğrusallık bozukluğu göstermiştir. Sadece orantı kontrolcüsü içeren ivmeölçer sistemine göre orantılı-entegral kontrolcüsü içeren ivmeölçer sistemi doğrusallık bozukluğunu 20 kata kadar iyileştirmiştir. Ayrıca, üretilen ivmeölçer 12.5 $\mu g/\sqrt{Hz}$ gürültü seviyesi, 5.8 μg offset kararsızlığı, 792 $\mu g/°C$ offset sıcaklık katsayısı, 1 mg altında açılıştan açılışa offset kararlılığı ve ±29 g ölçülebilir ivme aralığına ulaşmış, doğrusallık iyileştirmesi sağlarken yüksek performansını korumuştur.

Anahtar Kelimeler: Sigma Delta Modülatör, Sığasal Okuma Devresi, CMOS Kontrolcü Tasarımı, Yüksek Doğrusal İvmeölçer

To My Family

ACKNOWLEDGEMENTS

First and foremost, I would like thank to my thesis advisor Prof. Dr. Tayfun Akın for his support, guidance, and encouragement during my graduate studies. It is a great opportunity for me to work in his MEMS research group.

I also would like to thank to Dr. Said Emre Alper for sharing his deep knowledge and friendly attitude during my M.Sc study. Without his guidance and helps, this study could not exist.

I would like to express my gratitude to the members of the METU-MEMS inertial sensor group; Tunjar Askarlı, Burak Eminoğlu and Onur Yalçın for sharing knowledge on the capacitive interface circuits and for their technical guidance, and Yunus Terzioğlu, Ferhat Yeşil and Hasan Doğan Gavcar for fruitful discussion about the design of accelerometer system and for their invaluable friendship and support during this work.

Moreover, I would like to thank Talha Köse, Gülşah Demirhan and all members of the METU-MEMS VLSI research group for providing a nice research environment.

I also want to show my special thanks to Pınar Delibal for her patience and support during my studies, and my brother Umut Aykutlu for his helps throughout my life.

Last but not least, I would express my deepest gratitude to my parents Bedriye and Cevdet Aykutlu for their endless support, love and encouragement throughout my whole life.

TABLE OF CONTENTS

ABSTRACT v

ÖZ vii

ACKNOWLEDGEMENTS x

TABLE OF CONTENTS xi

LIST OF FIGURES xiv

LIST OF TABLES xviii

CHAPTERS

1 INTRODUCTION 1

1.1 Performance Specifications and Application Areas of MEMS Accelerometers 3

1.2 Overview of Sigma-Delta Interface Circuits for Capacitive MEMS Accelerometer Sensors 5

1.3 Linearity Performance Overview of Capacitive MEMS Accelerometers 6

1.4 Research Objectives and Thesis Organization 8

2 ELECTRO-MECHANICAL ΔΣ MODULATOR THEORY 11

2.1 Operation Principles of Electronic Sigma Delta Modulator 11

2.2 Electro-Mechanical Sigma Delta Modulator 15

2.2.1. Mechanical Block: Capacitive MEMS Accelerometer 16

2.2.2. Sensor Interface and Electronic Sigma Delta Modulator 18

2.3 Stability Analysis of the Electro-Mechanical ΣΔ Modulator 19

2.4 Noise Analysis of the Electro-Mechanical ΣΔ Modulator 22

2.5 Linearity Analysis of the Electro-Mechanical ΣΔ Modulator 24
2.6 Summary 29
3 DESIGN AND IMPLEMENTATION OF THE NEW READOUT CIRCUIT 31
3.1 Architecture of the New Readout Circuit 31
3.2 Proportional-Integral Controller Circuit 33
3.2.1. Proportional Controller 34
3.2.2. Integral Controller 38
3.3 Multiphase Clock Generator 42
3.4 Serial Programing Interface 43
3.5 Top Level Implementation and Simulation Results 44
3.6 Summary 48
4 DESIGN OF A 5TH ORDER ACCELEROMETER SYSTEM 49
4.1 5th Order Accelerometer System Parameters 50
4.2 Stability Analysis and Closed Loop Response 53
4.3 Noise Performance of the 5th Order Accelerometer System 56
4.4 Linearity Performance of 5th Order Accelerometer System 60
4.5 Summary 64
5 TEST RESULTS AND DISCUSSIONS 65
5.1 Data Acquisition Board 65
5.2 Scale Factor Stability Test 67
5.3 Linearity Test 70
5.4 Noise and Bias Drift Measurement 78
5.4.1. Feedback Voltage Optimization 83
5.5 Bias Repeatability Measurement 86
5.6 Temperature Test 89
5.7 Summary 91

6 CONCLUSIONS AND FUTURE WORK 93

REFERENCES 97

LIST OF FIGURES

FIGURES

Figure 2-1: A one bit sigma delta modulator used as an analog to digital converter. 12
Figure 2-2: Linear z-domain model of 1-bit sigma delta modulator. 13
Figure 2-3: In band noise power for L^{th} order sigma delta modulators with varying oversampling ratio [42]. 15
Figure 2-4: Structural drawing of capacitive MEMS accelerometer sensor [43]. 16
Figure 2-5: Linear model of electro-mechanical sigma delta accelerometer system presented in [45]. 20
Figure 2-6: Linear electro-mechanical sigma delta accelerometer system with noise sources. 23
Figure 2-7: Non-linearity of an accelerometer system as a function of input acceleration and u which is a ratio of displacement to finger gap. Loop gain of the system is adjusted to be 7 which is corresponding to a typical loop gain for accelerometer system studied in this thesis without including PI controller. 28
Figure 3-1: Architecture of the unconstrained mixed-feedback sigma delta modulator firstly proposed in [24] and realized as 4th order sigma delta modulator in [18]. 32
Figure 3-2: General architecture of unconstrained accelerometer system. 5^{th} order EM sigma delta modulator is realized by inserting PI controller into the loop. 33
Figure 3-3: Proportional controller block schematic with offset compensation. 35
Figure 3-4: Timing diagram of the proportional controller. 36
Figure 3-5: Noise spectrum of the P-controller showing flicker noise suppression for the unity gain configuration. 38
Figure 3-6: Integral controller block schematic with offset compensation. 39
Figure 3-7: Noise spectrum of the I-controller with $C3$ and $C4$ capacitors are selected to be $0.3pF\ and\ 24\ pF$. 41

Figure 3-8: Timing diagram of the complete readout chip adjusted by the multiphase clock generator. 43
Figure 3-9: Layout of the complete readout chip. 45
Figure 3-10: Pad level simulation result of the front-end amplifier. Output voltage is recorded as $75\ mV$ for $200\ fF$ mismatch in accelerometer capacitances. 46
Figure 3-11: Pad level simulation result of the P-controller with unity gain configuration registering $76\ mV$ output voltage which verifies the amplification operation. 46
Figure 3-12: Pad level simulation result of I controller with the gain of 0.824. The output voltage is observed as $32\ mV$ verifying proper integration operation at the end of 13 integration cycle. 47
Figure 3-13: Pad level simulation result of accelerometer electrodes, proof mass and digital output of readout chip. 48
Figure 4-1: SIMULINK model of the 5th order electro-mechanical sigma delta modulator. 53
Figure 4-2: Bode diagram of accelerometer system open loop transfer function showing 620 phase margin. 55
Figure 4-3: Transient response of the PI-controller showing less than $0.2\ msec$ settling time for 10g step input. 56
Figure 4-4: Noise spectral density of the simulated accelerometer system including feedback voltage and readout circuit noise. The simulation results are in good agreement with the calculated white noise floor. 59
Figure 4-5: Noise spectral density of the simulated accelerometer system including Brownian noise, feedback voltage and readout circuit noise. The simulation results are in good agreement with the calculated white noise floor. 59
Figure 4-6: Displacement output of the accelerometer sensor for 10g input acceleration showing almost zero steady state error for $Cint = 10\ pF$. 62
Figure 4-7: Displacement output of the accelerometer sensor for 10g input acceleration without I-controller for $Cint = 1\ pF$. Although accelerometer system is adjusted for maximum loop gain configuration, large amount of steady state error can be observed at the output of the accelerometer sensor. 63
Figure 5-1: Accelerometer data acquisition board consists of regulator PCB, accelerometer package and FPGA. 66

Figure 5-2: Accelerometer sensor integrated with the CMOS readout circuit in 16-pin metal accelerometer package. 66
Figure 5-3: Scale factor of the accelerometer system (Package#1) utilizing both P-controller and PI-controller for 12 different loop gain configurations. PI-controller manages to keep scale factor constant regardless of loop gain verifying effect of I-controller. 69
Figure 5-4: Test setup for the linearity performance measurement of the accelerometer system utilizing P-controller and PI-controller. Centrifugal acceleration is applied to the accelerometer package using rate table. 71
Figure 5-5: Response of the accelerometer system with both P-controller and PI-controller for varying input centrifugal acceleration and $Cint = 5\,pF$. For the data collected with P-controller, slope of the fitted line which corresponds to scale factor is less than slope of the data collected with PI controller due to the limited loop gain of the accelerometer system utilizing P-controller. 72
Figure 5-6: Residuals for the accelerometer system including PI controller with input acceleration varying from 0g to 3g. The linearity test is conducted for 3 different integration capacitance values to observe non-linear off the system with varying loop gain and maximum deviation is registered as 0.39 mg. 73
Figure 5-7: Residuals for the accelerometer system including PI controller with input acceleration varying from 0g to -3g. Maximum deviation is registered as 0.45 mg.. 74
Figure 5-8: Residuals for the accelerometer system including P controller with input acceleration varying from 0g to 3g. Maximum deviation is registered as 5.38 mg for $Cint = 9pF$ configuration. 74
Figure 5-9: Residuals for the accelerometer system including P controller with input acceleration varying from 0g to -3g. Maximum deviation is registered as 3.22 mg for $Cint = 9pF$ configuration. 75
Figure 5-10: Data acquisition board is placed into the Faraday cage in noise measurement test setup to avoid electromagnetic interference. 78
Figure 5-11: Power spectral density of the Package #1 with PI-controller showing approximately -98.3 dB which corresponds to 12.16 μgHz white noise floor. 79
Figure 5-12: Acceleration output of the Package #1 including PI controller under zero-g condition. Offset of the output is subtracted from acquired data to normalize acceleration output around zero. 80

Figure 5-13: A typical Allan Variance plot showing various slopes for different error sources [53]. 81
Figure 5-14: Allan Variance plot for the output of the Package#1 with and without including I-controller. The plot proves that additional I-controller block does not affect the system noise performance. 82
Figure 5-15: Scale factor of the accelerometer system (Package#1) utilizing both P-controller and PI-controller for 12 different loop gain configurations. Fitting is applied to the scale factor test results of accelerometer system utilizing P-controller according to the Equation 2.33, and effective spring constant is found to be 4.9 N/m. 85
Figure 5-16: Allan Variance plot of the Package #1 showing electronic flicker noise suppression by adjusting feedback voltage. Note that, correlated double sampling feature which eliminates flicker noise is disabled intentionally to illustrate effect of feedback voltage on the noise suppression. 86
Figure 5-17: Temperature dependent output of the accelerometer system utilizing PI controller. Temperature sensitivity of the output can be extracted as 792 µg/°C using linear fit. 90
Figure 5-18: Temperature dependent output of the accelerometer system utilizing P controller. Temperature sensitivity of the output can be extracted as 779 µg/°C using linear fit. 90

LIST OF TABLES

TABLES

Table 4-1: Parameters of the MEMS accelerometer which is designed and fabricated at METU-MEMS. MEMS accelerometer sensor is integrated with the readout circuit to form 5th order accelerometer system. 51

Table 4-2: Transfer functions and gain coefficients of the 5th order accelerometer system with predefined sampling frequency, feedback voltage and accelerometer sensor transfer function. Note that the adjustable circuit parameters are not determined yet. These adjustable parameters are selected considering the stability, noise and linearity in the further sections. 52

Table 4-3: Simulated noise contribution of each individual noise source for the configuration $Cint = 1\,pF, Cfb = 0.4\,pF, KP = 0.66\ and\ KI = 25000.$ 60

Table 4-4: Linearity simulation result of the accelerometer system with and without including I-controller. Also, the effect of a possible capacitance mismatch between the sensor electrodes is analyzed for different gain settings. 64

Table 5-1: Test configurations for the scale factor stability test. Expected loop gain is calculated at DC excluding effect of the electrostatic spring and I-controller gain. .. 68

Table 5-2: Linearity performance of the accelerometer system for both P-controller and PI controller with varying loop gain configuration. 76

Table 5-3: Linearity performance of the Package #2 for both P-controller and PI controller with varying loop gain configuration. 77

Table 5-4: Bias repeatability performance of the Package #2 with different feedback voltage levels and with and without I-controller. 88

Table 6-1: Non-linearity performance comparison of various accelerometers in the literature. 93

CHAPTER 1

INTRODUCTION

Invention of the transistor in Bell Research Laboratories [1] and development of fabrication techniques to create integrated circuits goes back to mid-20th century. While the advancement in the fabrication techniques has enabled production of compact electronic circuits in small area, it also formed basis for the evolution of the Micro-Electro-Mechanical Systems (MEMS). This technology has provided not only miniaturized mechanical and electro-mechanical devices but also large scale production with high performance, high reliability and low cost. With these advantages MEMS has found place in many diverse field including communication, inertial navigation, automotive, and healthcare.

Nowadays, MEMS market is rapidly growing due to the advantages of MEMS technology. In 2014, MEMS industry which is mostly dominated by inkjet printer heads, pressure sensors, microphones, inertial sensors, and optical devices represented an $11.1B revenue with the MEMS based devices and it is expected to exceed $20B by 2020 [2]. Inertial sensors including accelerometers and gyroscopes constitute large and dynamic market by dominating one quarter of the whole MEMS market. Automotive industry leads inertial sensors market for the airbag control, electronic stability control and automatic braking control applications requiring accelerometers or gyroscopes. Also, inertial sensors are increasingly started to take place in consumer electronics including cell phones and laptops. Although the inertial sensors are widely used in the automotive industry and commercial products meeting tactical grade performance are available in the market, MEMS inertial sensors are recently approaching navigation grade performance with the

enhancement in the mechanical design of the sensors and improvement in the interface circuits [3].

MEMS accelerometers are getting close to the navigation grade performance more rapidly compared to the MEMS gyroscopes due to their simpler mechanical structures and electronic interface. On the other side, macro-electromechanical and quartz resonating accelerometers provide an excellent dynamic range and high performance suitable for the inertial navigation grade applications [4, 5]. However, these accelerometers are expensive and suffer from degraded stability performance and limited shock tolerance. Among all the MEMS accelerometer sensors including piezoresistive, thermal, magnetic, piezoelectric and resonant type accelerometer sensors, capacitive MEMS accelerometers sensors have the potential to overcome aforementioned problems by providing high dynamic range and low noise.

While capacitive MEMS accelerometers are attractive due to their low temperature sensitivity, low cost and high sensitivity [6-8], varying gap type capacitive accelerometer sensors suffer from non-linear mechanical behavior. Also, there is still need for the dedicated high performance electronic interface integrated with the mechanical accelerometer sensor to reach navigation grade accelerometers. In addition, in the literature, special die attachment methods and stress isolation methods [9-11] are utilized during the packaging process, and various compensation methods are developed to suppress effect of the temperature, offset and wire bond capacitance drift to further improve the performance of accelerometers [12-15]. Apparently, different approaches are important to get close to accelerometers satisfying navigation grade performance.

Although varying gap capacitive MEMS accelerometers provide high sensitivity, high reliability and high shock tolerance, non-linear input-output transfer function of mechanical sensor may limit the linearity performance of the overall system and may pose an obstacle to achieve navigation grade performance. In order to eliminate the non-linear behavior and keep the proof mass of the mechanical sensor steady, MEMS accelerometer sensor are employed in closed loop operation in the literature as well as commercial products aiming high performance accelerometer system. While the non-linearity can be improved significantly compared to the open loop operation, it is

not possible to completely eliminate the non-linearity due to the limited loop gain using closed loop system, especially with sigma-delta type capacitive sensor interfaces. Therefore, in the scope of this thesis, it is aimed to eliminate non-linear behavior of mechanical sensor by employing a PI controller in the sigma delta type interface circuit to achieve perfect linearity while taking advantage of varying gap type capacitive MEMS accelerometer.

The organization of this chapter is as follows. Section 1.1 explains the definitions of the performance parameters for the accelerometers and specifies the requirements for the applications. Section 1.2 gives historical overview of interface circuits integrated with the capacitive MEMS accelerometer, also discusses the last status of the commercially available high performance accelerometers. Finally, Section 1.3 provides the research objectives and organization of the thesis.

1.1 Performance Specifications and Application Areas of MEMS Accelerometers

Today's MEMS accelerometers are finding place in wide range of applications ranging from automotive applications to aerospace and navigation application thanks to the reliable, high accuracy and low cost micro-fabrication techniques. Since requirements of the each application are different, the performance of the accelerometer is a key factor that determines the quality of the accelerometer and its application area. Scale factor, velocity random walk (VRW), resolution, input bandwidth, measurement range, and non-linearity are some of the performance parameters specifying quality of the accelerometer given in [16].

Scale Factor: Scale factor can be defined as sensitivity of the output to the input acceleration. The scale factor of the accelerometer is determined by the slope of the output vs input acceleration with the help of fitted line. While, for the accelerometer with analog output scale factor is expressed in V/g, unit of the scale factor is represented in counts/g for the accelerometers with digital output.

Measurement Range: Maximum detectable input acceleration without saturation defines the measurement range of the accelerometer.

Input Bandwidth: It is the frequency range that accelerometer operates in. Accelerometer can respond to the input acceleration in the input bandwidth without any loss while the sensitivity of the accelerometer vanishes for the out of band frequencies. Generally, accelerometer sensor behaves like low pass filter. Thus, input bandwidth of the accelerometer operating in open loop is mostly limited by the low pass characteristic of the accelerometer sensor. On the other hand, input bandwidth can be increased by adjusting frequency response of the mechanical filter or by operating the accelerometer in closed loop configuration.

Velocity Random Walk (VRW): It defines the velocity error related with the white noise in the acceleration output. The unit for the VRW is $g/\sqrt{Hz}$. Also, white noise floor of the accelerometer system can be found by multiplying the VRW which is determined for 1s averaging time interval by $\sqrt{2}$.

Resolution: Resolution can be defined as minimum detectable acceleration change. Noise floor of the accelerometer in the input bandwidth directly affects the resolution of the system. So, filtering can be used to improve resolution of the accelerometer. By decreasing the bandwidth of the output filter, noise can be suppressed out of filter bandwidth resulting in enhanced resolution at the cost of narrower input bandwidth.

Bias Instability: Accelerometer exhibits a non-zero output even in the absence of input acceleration. This non-zero output of the accelerometer is defined as bias. Due to the environmental effects, intrinsic behavior of mechanical accelerometer sensor and electronic interface bias of the accelerometer can shift to one side randomly. Bias instability describes the random variation of the bias for specified averaging time intervals in g.

Non-Linearity: Input to output transfer function of the accelerometer is not perfectly linear. So, the maximum deviation of the output data from the least squares linear fit of the input-output data determines the non-linearity of the accelerometer. Maximum deviation of the accelerometer is generally expressed in percentage of maximum input acceleration.

Animal tracking, airbag safety systems in automotive, structural monitoring, image stabilization, tilt sensing, seismic detection and inertial navigation and guidance can

be given as some of the application areas of MEMS accelerometers. For each application the performance specifications of accelerometer listed above is different and should be considered separately. For example, since tilt measurement application measures the static acceleration referencing gravity of earth, 2g measurement range is sufficient with low input bandwidth. On the other side, airbag safety system requires larger measurement range up to $\pm 50g$ with 400 Hz input bandwidth [17]. Since the accelerometer employed in the airbag system experiences high shock in the crash, resolution and non-linearity can be tolerable up to 100mg and 5%. Performance specifications of the MEMS accelerometer are quite strict for the inertial navigation and military applications. Resolution and measurement range of the accelerometer system are the critical parameter for the military applications. For the inertial navigation system, bias instability, resolution and non-linearity are the demanding factors and required to be below $10\mu g$, $4\mu g$ and 0.1% respectively [17, 18].

In order to meet the strict performance specification for the high-end application different approaches have been developed until now for both mechanical structure and electronic interface. Among all the interface circuits, switched capacitor type sigma delta modulators gained high popularity due to their high performance and direct digital output. Sigma delta modulator is employed as interface circuit in the scope of this thesis. So, next section gives the brief overview of sigma delta interface circuits before stating objectives of this thesis.

1.2 Overview of Sigma-Delta Interface Circuits for Capacitive MEMS Accelerometer Sensors

The first sigma delta circuit employing mechanical MEMS sensor in the loop was presented in a paper published in 1990 by W. Henrion et. al. to acquire direct digital output form the accelerometer [19]. In this paper, analysis of sigma delta circuit utilizing mechanical sensor element was given and noise floor was reported as $10\ \mu g/\sqrt{Hz}$ for the $\pm 0.1\ g$ full scale range. In 1995, B. E. Boser reported the implementation of MEMS accelerometer with readout circuit in a monolithic die achieving $1.6\ mg/\sqrt{Hz}$ noise floor for the $\pm 5\ g$ full scale range [20]. This study had important place in the literature with the discussions including mass residual

motion and lead compensator utilized in the loop to provide stable operation. In 2004, Carnegie Mellon University demonstrated surface micro-machined monolithic accelerometer operating in fully differential configuration with 4 separate sense capacitors [21]. This accelerometer accomplished $50\ \mu g/\sqrt{Hz}$ noise floor for $\pm 6\ g$ linear output range. In 2005, Petkov et. al. published a paper discussing fourth order sigma delta interface circuit designed for both accelerometer and gyroscopes [22]. This study showed the necessity of the high order sigma delta interface topologies to improve quantization noise. In 2006, H. Kulah et. al. published an another critical paper on the noise analysis of the second order sigma delta modulated accelerometer by including every possible noise sources [23]. In this work, accelerometer system achieved $10\ \mu g/\sqrt{Hz}$ noise floor for $\pm 10\ g$ output range with the closed loop operation. In 2011, U. Sonmez reported accelerometer system achieving $6\ \mu g/\sqrt{Hz}$ noise floor for $\pm 15\ g$ output range in [18] with the help of fourth order unconstrained sigma delta modulator topology which was firstly proposed by Raman et. al. in [24].

There are large numbers of accelerometer available in the market offered by various companies [25-27]. However most of these commercial products aim for low performance applications due to the large market share. On the other hand, Colibrys targeted for the high-end accelerometers and published several papers related with the enhancements in the scale factor stability, bias accuracy and resolution [28-30]. In 2011 this company announced a sigma delta modulated capacitive MEMS accelerometer achieving $1.7\ \mu g/\sqrt{Hz}$ noise floor for $\pm 15\ g$. Also, in 2014, Colibrys announced a new generation of accelerometer operating reliably under strong radiation and high temperature [31]. With the new generation accelerometer, Colibrys achieved to operate accelerometer up to $175\ °C$ with 0.05% nonlinearity which is well suited for guidance applications in space vehicles.

1.3 Linearity Performance Overview of Capacitive MEMS Accelerometers

Although varying gap capacitive MEMS accelerometers are preferred due to their high reliability and high sensitivity, non-linear mechanical sensor may limit the overall linearity performance of the accelerometer. In order to avoid such a

non-linear behavior of an accelerometer, these types of accelerometer sensors are generally operated in closed loop in order to balance the external acceleration and keep the proof mass stationary. However, closed loop operation itself contributes to the non-linearity and dominates the overall performance due to the non-linear voltage to force conversion taking place in feedback loop. To eliminate this feedback non-linearity problem, sigma delta control mechanism is favored method since pulse density modulation linearizes the voltage to force conversion by applying two level quantized voltages [32, 33]. In literature, integral controller is not employed in accelerometer system utilizing sigma delta control. Thus, overall linearity performance of such a system is limited with a proportional gain of an accelerometer system and non-linear MEMS accelerometer although it is operated in closed loop operation. On the other hand, closed loop operation with continuous or switched capacitor sensing mechanism combined with the analog force feedback can also be utilized while eliminating non-linear relation between voltage and force [34]. PID controller is mostly in use for these closed loop system utilizing analog force feedback to adjust closed loop response of an accelerometer system. Thus, linear analog force feedback together with I controller action which provides high gain at low frequencies may results in high linearity performance for an accelerometer system.

In 1994, T. Smith et. al. published a paper on the 3^{th} order accelerometer system with sigma delta control loop and reported the non-linearity as 1500 ppm [35]. In 2010, L. Aaltonen et. al. reported an accelerometer system with continuous time sensing and analog force feedback combined with the PID controller [36]. This work achieved 140 ppm non-linearity with ±1.5 g full scale input range. In 2010, M. Yucetas et. al. obtained 3300 ppm non-linearity with the utilization of switched capacitor sensing network, analog force feedback and PD controller [37]. In 2011, Y. Liang et. al. published a paper obtaining 500 ppm non-linearity by utilizing switched capacitor sensing, PID controller and analog force feedback loop [38]. In same year, Y. Liu et. al. obtained 600 ppm non-linearity with PID controller and switched capacitor sensing network [39]. In 2015, H. Xu et. all published a paper achieving 1500 ppm non-linearity with the utilization of sigma delta control for ± 1.2 g input range [40].

1.4 Research Objectives and Thesis Organization

The main purpose of this thesis is to demonstrate the improvement in the linearity performance for an electro-mechanical sigma delta accelerometer system utilizing PI controller in the loop. The specific objectives can be listed as follows:

1. Design and implementation of the PI controller that will be inserted into an electro-mechanical sigma delta accelerometer system. Controller block should be flexible enough in order to obtain stable operation by adjusting zero location of the controller, for interfacing with a wide range of capacitive accelerometers.
2. Noise is another concern while designing and implementing PI controller. Since input referred noise of this block directly affects the noise performance of the overall system, it should not exceed $500\ nV/\sqrt{Hz}$.
3. The circuit should be operated with both PI controller and P controller configuration in order to observe effect of additional integral action on the linearity performance of the system. So, P controller and I controller blocks will be implemented as two separate blocks and summation of the output signals will be carried out by the following electronic sigma delta modulator stage.
4. The non-linear behavior of the MEMS accelerometer is expected to be significantly reduced by the readout circuit employing the PI controller without degrading the performance parameters such as noise, bias instability bias temperature coefficient.
5. An experimental method shall be developed in order to determine the optimum feedback voltage, in order to improve the noise and bias stability of the accelerometer system.
6. A MATLAB-Simulink model shall be constructed and used for the verification of the stable operation and linearity enhancement.
7. The system level testing of the accelerometer with the readout circuit shall be performed including linearity, noise, temperature and bias stability. Linearity measurement test setup will be established by employing rate table and FPGA. Also, C++ code will be developed for the data acquisition.

The organization for the remainder of this thesis and contents of the chapters are as follows.

Chapter 2 introduces the theory of electro-mechanical sigma delta modulation starting from pure electrical sigma delta modulators. After presenting basic information related with the pulse density modulation behavior of the sigma delta modulators stability, noise and linearity analysis is carried out.

Chapter 3 presents the design and implementation of the PI controller block. Also, sub-blocks of the complete readout circuit is introduced in this chapter to explain operation of the readout circuit.

Chapter 4 gives the MEMS accelerometer parameters, design procedure and on-chip capacitance selection for the adjustable circuit blocks. Detailed noise and stability analysis is discussed to ensure stability with high performance. Also, linearity enhancement is demonstrated for the readout circuit taking advantage of PI controller with the calculations and simulations.

Chapter 5 gives the experimental test results of the designed accelerometer circuit integrated with the capacitive MEMS accelerometer sensor for both PI controller and excluding I-controller. Experimental test setup is described for each test and verification of enhancement in linearity performance is demonstrated with the test results. Also, experimental feedback voltage optimization procedure is explained in this chapter.

Finally, Chapter 6 summarizes the achievements presented in this thesis study, and discusses the possible future work to further improve accelerometer performance.

CHAPTER 2

ELECTRO-MECHANICAL ΔΣ MODULATOR THEORY

This chapter presents the theory and analysis of the electro-mechanical sigma delta modulator system. Section 2.1 presents the basic operation principles of electronic sigma delta modulator and gives basic formulation related with the quantization error. Section 2.2 provides information on the mechanical and electronic blocks forming electro-mechanical system. Section 2.3 gives stability analysis methods for the electro-mechanical sigma delta modulators and introduces the linear accelerometer model that is used to estimate transient behavior of a system. Section 2.4 establishes output referred noise calculations for electronic and mechanical noise sources. Section 2.5 gives the detailed non-linearity sources for electro-mechanical sigma delta modulators utilizing varying gap type accelerometer, and offers a solution to overcome non-linearity problem. Finally, Section 2.6 summarizes this chapter.

2.1 Operation Principles of Electronic Sigma Delta Modulator

Although sigma delta modulation technique was established in many years ago [41], sigma delta modulators gained popularity with the developing VLSI technology in the recent years. Cost effectiveness, robustness against imperfections to the fabrication depended imperfections, and high resolution output have made this type of data converters superior over Nyquist-rate converters in applications requiring limited bandwidth operation. Despite the fact that sigma delta modulators provide high resolution by using oversampling and noise shaping concepts, output of the modulator has limited bandwidth. Thus, sigma delta converters offer slow and

medium speed conversion, and they are well suited for the processing of baseband signals with high resolution.

Figure 2-1 shows a one bit first order sigma delta modulator which is used to explain the basic operation principles of sigma delta modulators. First order sigma delta structure employs an integrator and quantizer in the feed-forward path and feedback is provided by two level output of the quantizer to the integrator inputs.

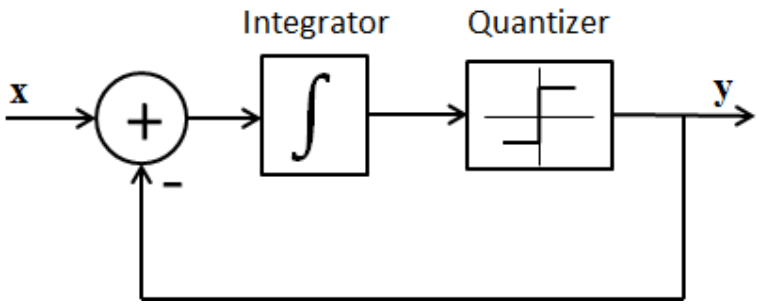

Figure 2-1: A one bit sigma delta modulator used as an analog to digital converter.

Quantizer decides its output by comparing the integrator output with the predetermined threshold for each cycle, and tries to keep the integrator output close to the threshold by reversing its output. Consequently time average of quantizer output forces integrator input to be zero. Note that only the time average of the quantizer output approaches to the zero while the output of the integrator oscillate around quantizer threshold. As seen in Figure 2-1 quantizer introduces non-linear behavior to the system, and to simplify the analysis, linear model needs to be constructed by applying white noise assumption for the quantization error signal [42]. Figure 2-2 presents the linear z-domain model of 1-bit sigma delta modulator that is used for the analysis.

While constructing linear model of the sigma delta converter, it is assumed that integrator output is uniformly distributed between maximum and minimum range so that quantizer can be modeled as additive white noise in the linear model. Then, power and RMS value of this additive white noise referred as quantizer error can be given as

$$e_{RMS}^2 = \frac{1}{q}\int_{-q/2}^{q/2} e^2 de = \frac{q^2}{12} \quad 2.1$$

$$e_{RMS} = \frac{q}{\sqrt{12}} \quad 2.2$$

where q is the quantization interval. Quantization noise folds into the frequency determined by the sampling frequency of the quantizer. Again assuming quantization noise is random the spectral density of the quantization noise and RMS noise in the bandwidth of interest takes the form

$$E(f) = e_{RMS}(\frac{2}{f_s})^{0.5} \quad 2.3$$

$$n_{QB(RMS)} = e_{RMS}(\frac{2f_B}{f_s})^{0.5} \quad 2.4$$

where f_s is the sampling frequency of the quantizer and f_B is the bandwidth of interest. Note that $f_s/2f_B$ is known as oversampling ratio, and increasing oversampling ratio reduces the in band quantization error according to Equation 2.4.

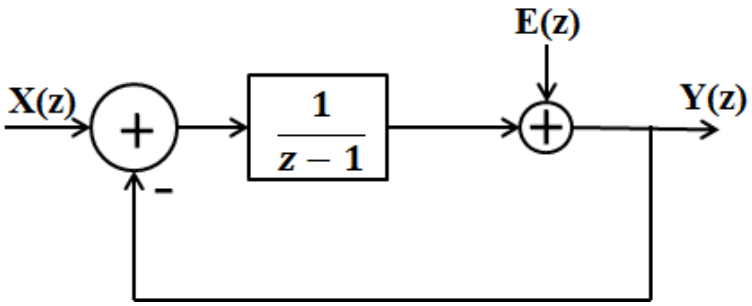

Figure 2-2: Linear z-domain model of 1-bit sigma delta modulator.

After deriving the linear model for the quantizer and introducing quantization error formulations, sigma delta modulator in Figure 2-2 needs to be analyzed to calculate the sigma delta modulator quantization noise. The output of the sigma delta modulator can be found in z- domain as

$$Y(z) = z^{-1}X(z) + (1 - z^{-1})E(z) \quad 2.5$$

According to the Equation 2.5 input signal is delayed by one sample, on the other side quantization noise is filtered by transfer function of $1 - z^{-1}$. Filtering of

quantization error by transfer function of $1 - z^{-1}$ is known as noise shaping, and transfer function $1 - z^{-1}$ is referred as noise transfer function (NTF). Thus, noise shaping removes the quantizer noise from bandwidth of interest to the high frequency band by placing zero at DC, and it proves the importance of the sigma delta modulator to obtain a high resolution signal in a narrow bandwidth.

Noise shaping analysis can be extended further for the higher order sigma delta converters to reveal the importance of the noise shaping concept. By adding more integrators in the form of $1/(z-1)$ and feedback branches to the system higher order sigma delta modulators can be obtained. For higher order modulator, resulting noise transfer function and in band noise power is given in [42] as

$$NTF = (1 - z^{-1})^N \tag{2.6}$$

$$n_{B(RMS)} = e_{RMS} \frac{\pi^N M^{-(L+0.5)}}{\sqrt{2L+1}} \tag{2.7}$$

where L is the number of integrator utilized in the sigma delta modulator and M is the oversampling ratio. Equation 2.7 reveals the fact that oversampling ratio and order of the sigma delta modulator are critical two factors to reduce in band quantization noise. Figure 2-3 shows the in band noise power for L^{th} order sigma delta modulators to illustrate the effect of oversampling ratio and modulator order [42].

Sigma delta modulators depicted in Figure 2-1 outputs 1-bit digital signals that consist of input signal information and quantization noise building up mostly in high frequencies rather than bandwidth of interest as a result of noise shaping. However, this one bit output is not meaningful since it has low resolution with high sampling rate without processing. Therefore, input signal information in the bandwidth of interest which has low quantization noise power should be extracted by digital low pass filtering or band pass filtering. This digital filtering process does not change the sampling frequency of the output whereas sampling rate is too high compared to the Nyquist frequency to represent the input signal. Thus, decimation is required for reducing sampling rate of output to ease further digital processing by decreasing number of data. In addition to ease further digital processing, decimation allows to reduce in-band rms noise at the expense of narrower system bandwidth.

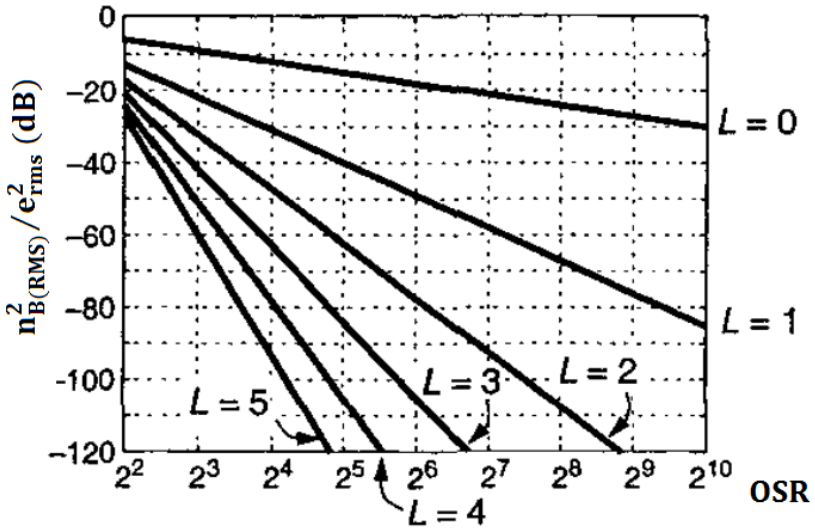

Figure 2-3: In band noise power for L[th] order sigma delta modulators with varying oversampling ratio [42].

2.2 Electro-Mechanical Sigma Delta Modulator

The sigma-delta converters comprising mechanical sensor element are named as electro-mechanical sigma delta converters. These types of converters may consist of single mechanical sensor element or they may involve additional electronic integrators connected with the mechanical sensor element to form higher order electro-mechanical sigma delta converters.

It is important to examine mechanical behavior of the MEMS accelerometer sensor to analyze the noise shaping, stability and noise of electro-mechanical system while integrating MEMS accelerometer sensor element to the system. Thus, the mechanical behavior of the capacitive MEMS accelerometer must be well understood. In the following section, sensing mechanism and capacitive actuation mechanism that enable closed loop operation is briefly introduced to have a better understanding of relation between the mechanical MEMS accelerometer and electronic sigma delta block. Also, electronic blocks used in the electro-mechanical system are briefly introduced.

2.2.1. Mechanical Block: Capacitive MEMS Accelerometer

In order to describe the operation of MEMS accelerometer sensor, structural drawing of capacitive sensor utilized in this thesis is shown in Figure 2-4. The capacitive sensor is made of pair of electrodes fixed to the base and proof mass which is suspended by spring. Pair of capacitor is formed between proof mass and two separate conductive stationary electrodes. Capacitance between conductive proof mass and two electrodes changes with respect to the position of the movable proof. So this type of accelerometer sensor is known as a capacitive sensor.

In capacitive accelerometer sensor, external acceleration acting on suspended proof mass results in force according to Newton's law:

$$F_{ext} = ma_{ext} \tag{2.8}$$

where m is the mass of proof mass.

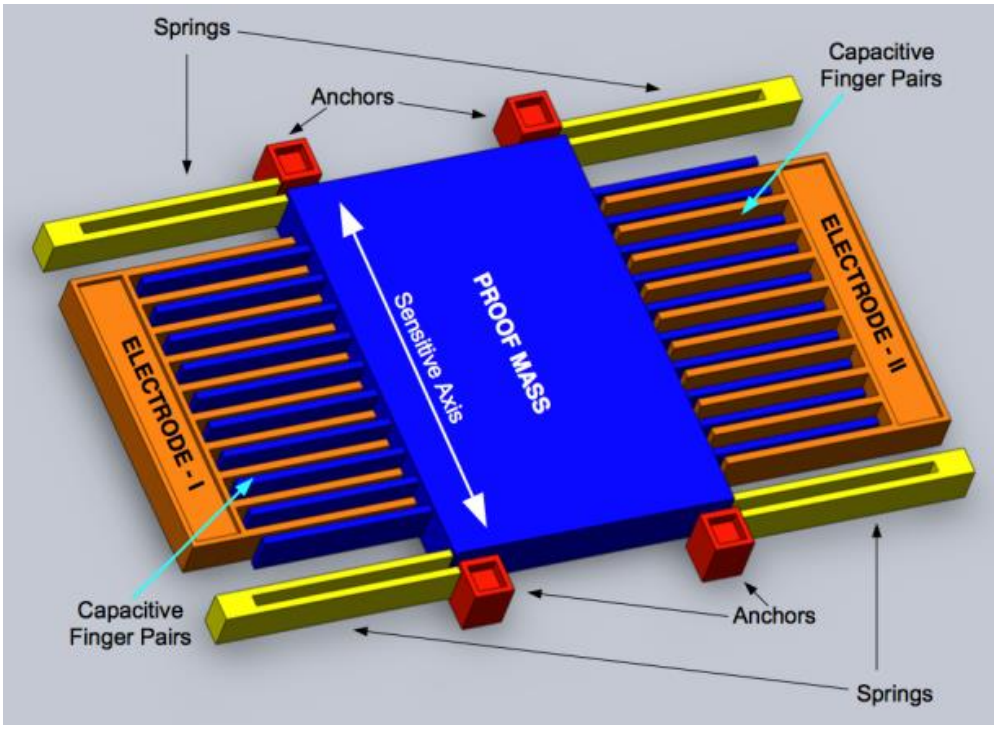

Figure 2-4: Structural drawing of capacitive MEMS accelerometer sensor [43].

Since proof mass is suspended via mechanical springs, an external force applied along the sensitive axis of the accelerometer results in a displacement from its initial position according to the Newton's law:

$$m\ddot{x} + b\dot{x} + kx - F_{ext} = 0 \tag{2.9}$$

where k is the spring constant, b is the damping coefficient, $\dot{x}$ and $\ddot{x}$ are the first and second derivatives of displacement respectively. Then, force to displacement transfer function of spring damper model of capacitive accelerometer is defined as

$$H_{F/x}(s) = \frac{1/m}{s^2 + \frac{b}{m}s + \frac{k}{m}} = \frac{1/m}{s^2 + \frac{w_0}{Q}s + {w_0}^2} \tag{2.10}$$

In the spring damper system transfer function, natural frequency and quality factor are also defined as

$$w_0 = \sqrt{\frac{k}{m}} \tag{2.11}$$

$$Q = \frac{\sqrt{km}}{b} \tag{2.12}$$

Displacement output of the mechanical accelerometer system should be converted into electrical domain by means of capacitor formed between proof mass and electrodes to be detected by capacitive electronic interface. By considering the displacement dependent capacitance between each proof mass finger and adjoining electrode fingers, the total capacitance between the proof mass and a single fixed electrode for varying gap type MEMS accelerometer of Figure 2-4 is given as

$$C = \varepsilon_0 \frac{NA}{d_1 - x} + \varepsilon_0 \frac{(N-1)A}{d_2 + x} \tag{2.13}$$

where ε_0 is the permittivity of the air, A is the capacitive overlap area of single finger pair, N is the number of finger pair, d_1 is the gap between finger pairs, d_2 is the anti-gap distance between proof mass finger and electrode finger of adjacent finger pair and x is the displacement resulting from applied external force. It can be seen that capacitances between proof mass and electrodes are non-linear functions of displacement. This non-linear behavior of utilized varying gap type MEMS accelerometer sensor is investigated in the following section. Under the small displacement of proof mass, sensitivity of capacitance to the displacement can be

found by taking the derivative of Equation 2.13 with respect to displacement and assuming $x = 0$. Then the sensitivity of the capacitance can be formulated by

$$\frac{dC}{dx} = \varepsilon_0 A \left(\frac{N}{d_1^2} - \frac{N-1}{d_2^2} \right) \quad 2.14$$

Electrostatic force is another important phenomenon to understand the actuation mechanism of capacitive MEMS accelerometer sensor. Firstly, energy stored in the capacitor should be considered to explain the electrostatic force. Every capacitive element contain at least two conductive plates to store energy in the form of electrostatic field between its plates, and energy stored in the capacitor can be expressed by well-known formula

$$E = \frac{1}{2} C V^2 \quad 2.15$$

where C is he capacitance and V is the potential difference between capacitor plates. Finally, to express electrostatic force generated between plates of varying gap type capacitive MEMS accelerometer, capacitance formula in Equation 2.13 needs to be substituted into Equation 2.15 and derivative of energy with respect to displacement should be calculated to define electrostatic force as

$$F = \frac{1}{2} \frac{dC}{dx} V^2 \quad 2.16$$

where dC/dx is the sensitivity of the capacitance derived in Equation 2.14 for varying gap type accelerometer sensor. Electrostatic force given in Equation 2.16 is always attractive, and it enables closed loop operation by means of capacitive actuation. Also, note that voltage to force conversion introduces non-linear effect due to the V^2 term which is eliminated by inherently linear behavior of single bit sigma delta modulator.

2.2.2. Sensor Interface and Electronic Sigma Delta Modulator

Since electro-mechanical sigma delta modulator system comprises both mechanical and electronic blocks, the output of the mechanical sensor should be converted to electrical domain. Previously in Equation 2.13, it is stated that capacitances between accelerometer sensor electrodes directly depend on the displacement vector which is the output of the mechanical accelerometer sensor. Thus, capacitance deviation is

observed in the case of external stimulation. Electronic sensor interface which will be referred as front-end amplifier from now on, converts this capacitance change into voltage which is transferred to the electronic sigma delta modulator. It is important to note that front-end amplifier's poles and zeros are at much higher frequency compared to the operating frequency of the accelerometer system. Thus, front-end amplifier is modeled as a simple gain stage which does not introduce any pole and zero into the accelerometer system.

Electronic sigma delta converter is cascaded to the front-end amplifier and its output is fed back to mechanical sensor to form complete electro-mechanical sigma delta modulator. Main task of this block is to encode the front-end amplifier output as pulse density modulated 1-bit digital signal. The order of the complete system is determined by the number of integrators in the loop. Since N^{th} order electronic sigma delta modulator includes N number of integrator and accelerometer sensor is modeled as 2 leaky integrators in Equation 2.10, the order of the complete accelerometer system is generally referred as $(N+2)^{th}$ electro-mechanical sigma delta modulator. Remember that, similar to the electronic sigma delta modulator, quantization noise suppression becomes more and more aggressive as the order of electro-mechanical system is increased. However, it gets harder to ensure system stability with the increasing number of integrators. Thus, system order should be adjusted in such a way that, quantization noise in the base band is suppressed below overall circuit noise to achieve maximum resolution while guaranteeing stable operation.

2.3 Stability Analysis of the Electro-Mechanical ΣΔ Modulator

All sigma delta modulators include non-linear quantizer element which performs high speed digitization in the loop. Although this non-linear element can be linearized as in Figure 2-2 by assuming quantizer with additive white noise, the linear model of the modulator is not sufficient to determine stability of the system. So, stability of the system is a major concern for the sigma delta modulator during the design phase. Many researches have been conducted to determine the stability of the sigma delta modulator. However, proven results are generally valid for specific modulators and input signal with constant amplitude which is not accurate in most

cases. Thus, there is no exact and complete analysis technique exists in the literature to ensure stable operation of the electronic sigma delta modulators. On the other hand, Lee criterion which states modulator with noise transfer function NTF satisfying $||NTF||_\infty < 1.5$ for all frequencies is likely to be stable is the best known and widely used criterion during the design phase [44].

As in the case with electronic sigma delta modulators, electro-mechanical sigma delta modulators also suffer from absence of exact analytical methods to examine the stability of the system. While Lee criterion can be applied in the analysis of electro-mechanical system to achieve stable operation, another linear model to determine stability and settling response of the electro-mechanical system is presented in [45]. This linear model also does not guarantee the stability of the electro-mechanical system, but it establishes a well matched transient response for the electro-mechanical sigma delta accelerometer system. Figure 2-5 shows the linearized model of the electro-mechanical sigma delta accelerometer system.

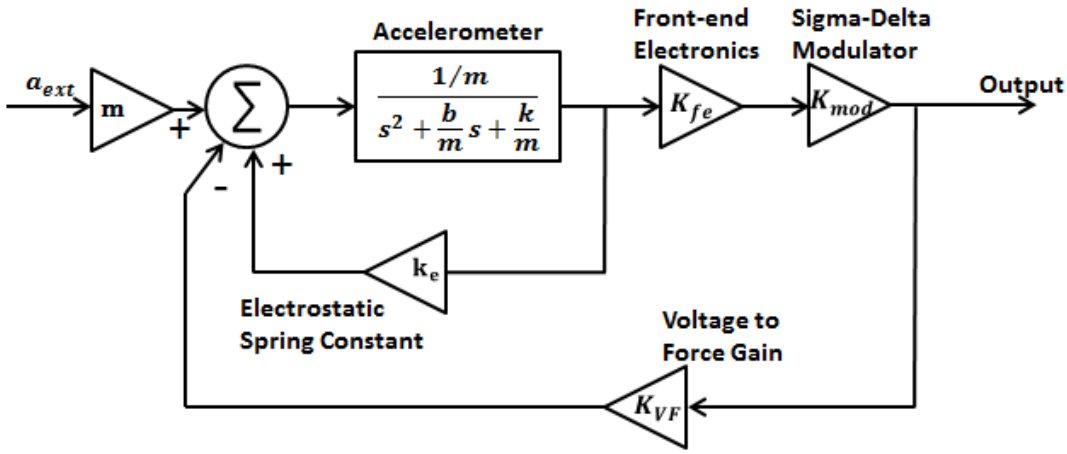

Figure 2-5: Linear model of electro-mechanical sigma delta accelerometer system presented in [45].

In Figure 2-5 $K_{fe}, K_{mod,}\ K_{VF}, and\ k_e$ represents the front-end electronics, electronic sigma delta modulator, voltage to force gain and electrostatic spring constant respectively. While electronic sigma delta modulator block is modeled as simple gain stage, its stability is not considered during the linear model construction. Since

electronic sigma delta modulator performs high speed conversion, and its output is pulse density modulated form of its input, high frequency components does not affect the accelerometer sensor which has low pass filter characteristic. Thus, representing electronic sigma delta modulator as a simple gain stage is quite valid and accurate assumption for frequencies below a few kHz.

On the other hand, linearization takes place during the calculation of voltage to gain conversion and electrostatic spring constant. In Equation 2.16 voltage to force conversion formula includes dC/dx term. This term introduces non-linearity in the voltage to force conversion due to the displacement dependent sensitivity of the varying gap type accelerometer sensor. Thus, linearization of the voltage to force conversion is performed by taking $x = 0$. Then, resulting voltage to force gain can be given as

$$K_{VF} = \frac{V^2}{2}\varepsilon_0 A\left(\frac{N}{d_1^2} - \frac{N-1}{d_2^2}\right) \tag{2.17}$$

Note that there is also a non-linear term V^2 in the Equation 2.17 which is naturally linearized by the pulse density modulated output of the electronic sigma delta modulator [46]. The first term of the Taylor series expansion of the capacitance sensitivity dC/dx is considered in Equation 2.17 by taking $x = 0$ to calculate voltage to force gain. In addition, linearization of the voltage to force conversion is strengthened by taking the second term of the Taylor series expansion of the capacitance sensitivity dC/dx in this model. The second term of Taylor series expansion which is referred as electrostatic spring constant is given by the formula:

$$k_e = \frac{V^2}{2}\frac{d^2C}{dx^2} = V^2\varepsilon_0 A\left(\frac{N}{d_1^3} + \frac{N-1}{d_2^3}\right) \tag{2.18}$$

Electrostatic spring constant given in Equation 2.18 acts as a positive feedback on the varying gap type accelerometer sensor and it introduces displacement dependent feedback force on the sensor. Due to the positive feedback effect of electrostatic spring constant, overall spring constant of accelerometer decreases which is a well-known phenomenon referred to as the spring softening effect for varying gap type capacitive accelerometer sensors.

Despite the fact that linearized model shown in the Figure 2-5 does not completely ensure the stability of the complete system, it can be used for adjusting the phase margin to achieve fast settling at the output by using well known LTI techniques. Additionally, this linear model can be used to estimate noise contribution of each block at the baseband while quantization noise should be calculated based on non-linear system simulations.

2.4 Noise Analysis of the Electro-Mechanical ΣΔ Modulator

System level noise analysis is not an easy task for electro-mechanical sigma delta modulator with non-linear model. While it is required to analyze the noise contribution of each block in the non-linear model simulations for verification and optimization, linear model presented in the Figure 2-5 can be used for quick noise calculation. Figure 2-6 shows the linear electro-mechanical sigma delta accelerometer system with all noise sources included in the model.

Linearized model with noise sources illustrated in Figure 2-6 is used to analyze the noise contributions of Brownian noise, front-end amplifier output referred noise, and feedback voltage noise. Note that linearized model of accelerometer system is not suitable to extract the noise contribution of quantization error. Also, Equation 2.7 is not completely accurate to estimate the RMS value of quantization noise in the band of interest. Because, behavior of accelerometer sensor utilized in the electro-mechanical sigma delta modulator does not completely match with the electronic integrator due to the leaky behavior and low gain of the sensor element. Therefore, quantization noise contribution at the output should be estimated based on non-linear model simulations with different input conditions.

Brownian noise denoted as $a_{n,b}$in Figure 2-6 is one of the noise sources in the accelerometer system which is caused by random mechanical motion of the sensor. Input referred Brownian noise of the accelerometer is given by the equation

$$a_{n,b} = \frac{\sqrt{4k_B T b}}{m} \tag{2.19}$$

where m is the mass of the proof mass, T is the absolute temperature in Kelvins, b is the damping coefficient of the accelerometer in Ns/m, and k_B is the Boltzmann's

constant in Nm/K. Brownian noise acts as an external input to the system, and it is transmitted to the output directly. So output referred Brownian noise also can be directly calculated as in Equation 2.19 in $m/s^2/\sqrt{Hz}$.

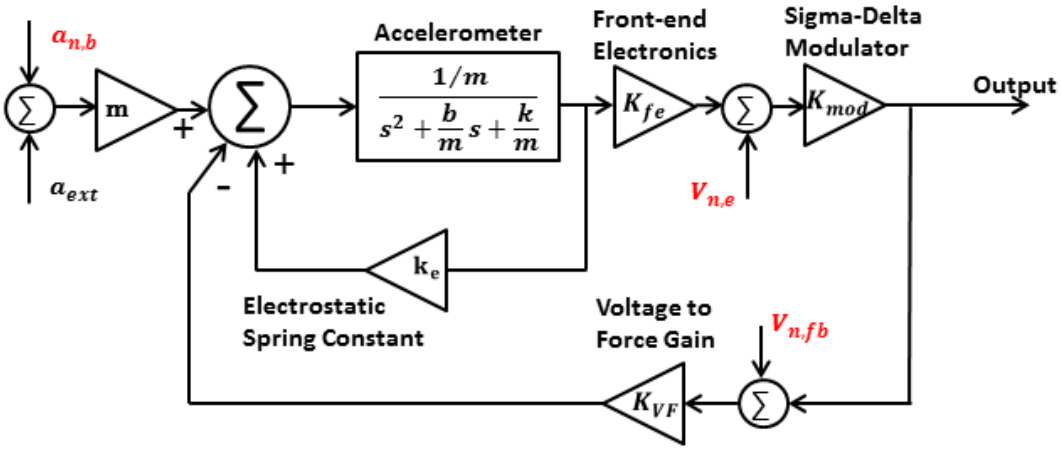

Figure 2-6: Linear electro-mechanical sigma delta accelerometer system with noise sources.

Feedback voltage is used for balancing external acceleration, and noise on the feedback voltage directly transforms into the force acting on the proof mass. Hence, this voltage is one of the limiting factors for achieving low noise performance. Input referred acceleration equivalent feedback voltage noise can be calculated as

$$a_{n,fb} = \frac{v_{n,fb}V_{fb}}{m}\varepsilon_0 A\left(\frac{N}{d_1^2}-\frac{N-1}{d_2^2}\right) \qquad 2.20$$

where $V_{fb}\ and\ v_{n,fb}$ are the feedback voltage amplitude and the noise on the feedback voltage, respectively. Equation 2.20 asserts that feedback voltage dependent noise is directly proportional to applied voltage amplitude. So, output noise of the accelerometer system is likely dominated by the feedback voltage for increased feedback voltage amplitude. This phenomenon should be considered during the design phase of the system to achieve low noise operation while keeping the output range as high as possible in order to increase the dynamic range of the accelerometer system.

Lastly, front-end amplifier output-referred electronic noise contribution is analyzed using linear electro-mechanical accelerometer model. Electronic noise consists of output-referred noise of front-end amplifier and input-referred noise of the electronic sigma delta modulator. Equation 2.21 gives the acceleration equivalent output noise resulting from the electronic noise at DC.

$$a_{n,e} = \frac{1}{m}\frac{K_{VF}K_{mod}(k-k_e)}{K_{VF}K_{fe}K_{mod}+(k-k_e)}v_{n,e} \qquad 2.21$$

In Equation 2.21 it can be clearly seen that output referred noise of the electronic noise can be reduced by adjusting the $k-k_e$ term which is referred as effective spring constant . k is the mechanical spring constant of the accelerometer sensor, and cannot be changed after the sensor fabrication. On the other hand, the electrostatic spring constant can be tuned by manipulating feedback voltage using Equation 2.18 to lower the electronic noise effect at baseband. Thus, spring softening phenomenon observed in varying gap type accelerometer sensor makes it possible to suppress the electronic noise below the Brownian noise limit and relaxes the design of the electronic blocks. In fact effective spring constant can be adjusted to be zero which cancels out the flicker noise significantly. Noise cancelling effect is proven and an experimental method to determine effective spring constant is presented together with the test results in Chapter 5.

2.5 Linearity Analysis of the Electro-Mechanical ΣΔ Modulator

Varying gap type capacitive accelerometer sensors are widely preferred in the accelerometer system compared to varying overlap type capacitive accelerometer sensors due to their high sensitivity. However, the open loop accelerometer system utilizing varying gap type capacitive accelerometer suffers from the linearity degradation due to the displacement dependent sensitivity which takes part in front-end amplification as a proportional term. On the other hand, the closed loop accelerometer system minimizes the non-linearity resulting from the displacement dependent sensitivity by keeping the proof mass steady in the act of external acceleration.

Systems differ from each other according to the number of poles at DC which directly affect the steady state error of that system. A system with n poles at DC is

said to be type-n system. While closed loop accelerometers with the transfer function in the form of Type-1 or Type-2 systems keep the proof mass stationary with zero steady state error, Type-0 systems illustrated in the Figure 2-5 cannot perfectly balance the external acceleration due to the limited loop gain at DC and causes steady state error [47]. The loop gain of the accelerometer system and steady state error for the system in Figure 2-5 can be given as

$$A_L = \frac{1}{k}\left(K_{fe}K_{mod}K_{VF} - k_e\right) \tag{2.22}$$

$$e_{SS} = \frac{1}{1 + A_L} \tag{2.23}$$

It can be clearly seen that limited loop gain at DC which is the main concern to achieve adequate linearity performance causes non-zero displacement in the act of external acceleration. Due to this non-zero displacement, the displacement dependent sensitivity term introduces a non-linearity to the system via voltage to force conversion and front-end amplifier gain term. Displacement to voltage and voltage to force conversions needs to be examined to reveal the non-linear terms emerging from the steady state error.

Displacement to voltage conversion, which is performed in the front-end electronics, depends on the difference between two capacitors formed in the accelerometer sensor and can be defined as

$$V_{fe,out} = \alpha(C_1 - C_2) = K_{fe,NL}x \tag{2.24}$$

where α is the amplification constant, $C_{1,2}$ are the capacitances formed between proof mass and electrodes and $K_{fe,NL}$ is the displacement to voltage conversion constant. By assuming anti-gap is sufficiently large compared to the gap, the capacitances can be expressed using Taylor series expansion as

$$C_{1,2} = \frac{\varepsilon_0 AN}{d_1}\left(\frac{1}{1 \mp u}\right) = \frac{\varepsilon_0 AN}{d_1}(1 \pm u + u^2 \pm u^3 + u^4 \pm \ldots) \tag{2.25}$$

where $u = x/d_1$. If the Equation 2.24 is reconsidered using Taylor series expansion of the capacitances, $K_{fe,NL}$ takes the form

$$K_{fe,NL} = 2\alpha\frac{\varepsilon_0 AN}{d_1^2}(1 + u^2 + u^4 + \ldots) \tag{2.26}$$

The first term in the parenthesis is the linear term and the remaining terms are the even harmonics that causes non-linear behavior. For a u value of 0.01 (%1) and 0.1 (%10), ratio of non-linear terms to linear terms are 0.0001 (%0.01) and 0.01 (%1) respectively which shows the highly non-linear behavior of displacement to voltage conversion.

Closed loop operation that is established to reduce non-linearity by keeping the proof mass stationary introduces a non-linearity itself due to the non-linear voltage to force feedback path. This feedback path dominates the linearity performance of the system if the loop gain of the system is not sufficient to counterbalance the external acceleration. Input voltage to output force conversion that defines feedback force term can be extracted as

$$F_{VF,out} = \frac{V_{fb}^2}{2}\left(\frac{V_{VF,in}+1}{2}\frac{dC_1}{dx}+\frac{V_{VF,in}-1}{2}\frac{dC_2}{dx}\right) \quad 2.27$$

where $F_{VF,out}$ is the output force, $V_{VF,in}$ is the input voltage $dC_{1,2}/dx$ are the sensitivity of the capacitances formed between proof mass and electrodes. Again by assuming anti-gap is sufficiently large, sum and difference of sensitivity terms can be expressed by the Equation 2.28 and Equation 2.29 using Taylor series expansion:

$$\left(\frac{dC_1}{dx}+\frac{dC_2}{dx}\right) = 2\frac{\varepsilon_0 AN}{d_1^2}(1+3u^2+5u^4+\ldots) \quad 2.28$$

$$\left(\frac{dC_1}{dx}-\frac{dC_2}{dx}\right) = 4\frac{\varepsilon_0 AN}{d_1^3}x(1+2u^2+3u^4+\ldots) \quad 2.29$$

Equations 2.30, 2.31 and 2.32 can be obtained by substituting Equation 2.28 and Equation 2.29 into Equation 2.27:

$$K_{VF,NL} = \frac{V_{fb}^2}{2}\frac{\varepsilon_0 AN}{d_1^2}(1+3u^2+5u^4+\ldots) \quad 2.30$$

$$k_{e,NL} = V_{fb}^2\frac{\varepsilon_0 AN}{d_1^3}(1+2u^2+3u^4+\ldots) \quad 2.31$$

$$F_{VF,out} = K_{VF,NL}V_{VF,in} + k_{e,NL}x \quad 2.32$$

where $K_{VF,NL}$ is the voltage to force constant and $k_{e,NL}$ is the displacement to force constant which is known as electrostatic spring constant. For a u value of 0.01 (%1) and 0.1 (%10), ratio of non-linear terms to linear terms are 0.0003 (%0.03) and 0.03

(%3) respectively for the voltage to force constant. For same u values ratio of non-linear terms to linear terms appear as 0.0002 (%0.02) and 0.02 (%2) respectively for the displacement to force constant. It is clear that overall voltage to force conversion is also highly non-linear and it should be considered for not to degrade the linearity performance of the system.

Lastly, transfer function of the system should be calculated in order to comment on the linearity performance of the electro-mechanical accelerometer system. Transfer function of the accelerometer system can be extracted by using non-linear coefficients and linear accelerometer system illustrated in Figure 2-5. Equation 2.33 represents the closed loop transfer function of the accelerometer system at DC.

$$A_{CL} = \frac{mK_{fe,NL}K_{mod}}{(k - k_{e,NL}) + K_{fe,NL}K_{mod}K_{VF,NL}} \quad 2.33$$

Closed loop transfer function of the accelerometer system includes three non-linear terms $K_{fe,NL}$, $K_{VF,NL}$ and $k_{e,NL}$ in the denominator and one non-linear term $K_{fe,NL}$ in the numerator. It is not easy to extract direct non-linearity formula based on Equation 2.33, however it can be clearly seen that closed loop transfer function is highly dependent on the non-linear terms which likely causes severe non-linear behavior.

To illustrate the effect of the non-linear terms MATLAB code is written and non-linearity of the accelerometer output is plotted as a function of input acceleration and u which is x/d_1 using Equation 2.33. Figure 2-7 shows the non-linearity of an accelerometer system with varying input acceleration and displacement. Note that, loop gain of the accelerometer system is adjusted to be 7 which is corresponding to a typical loop gain in accelerometer system studied in this thesis in order to evaluate non-linearity.

While non-linearity can be kept at minimal for small amount of displacement with a varying input acceleration, the non-linearity of the system degrades severely with the increasing displacement and input acceleration. It is possible to keep the non-linearity of the accelerometer system at a minimum by boosting the loop gain. However, it is not practical to raise the loop gain over some threshold due to the stability issues. On the other hand, employing an additional integrator using PI

controller in the loop is simply yet effective solution to overcome the non-linearity problem which is firstly proposed in [46]. Phase margin of the system and the stability requirements can also be fulfilled by adjusting the zero location of the PI controller, while boosting the loop gain at DC. However, the contribution of non-linear terms of the mechanical sensor and finite gain of op-amp employed in the controller to the overall non-linearity performance of an accelerometer system are not examined analytically, and there is not any test results demonstrating high linearity performance of designed accelerometer system taking advantage of PI controller in the aforementioned study [46].

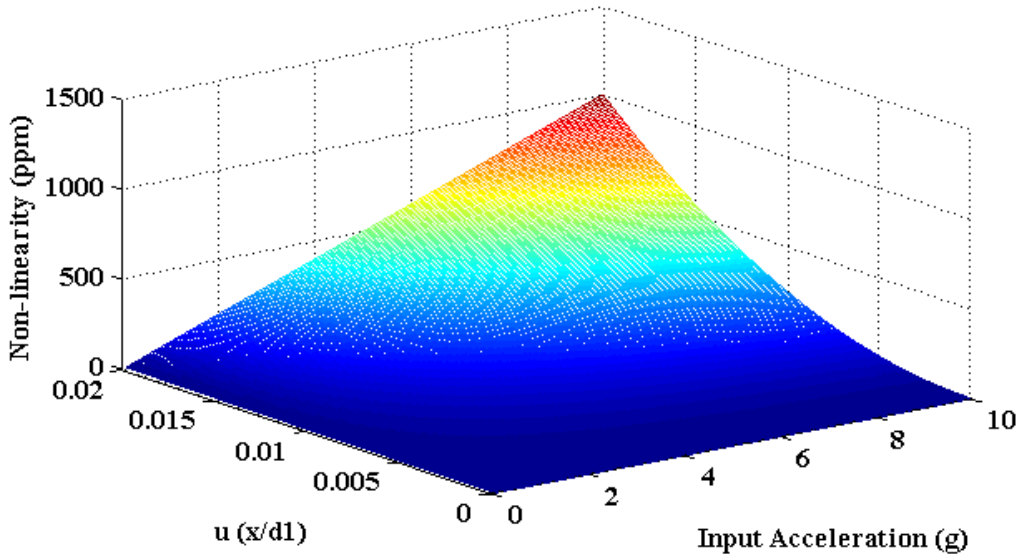

Figure 2-7: Non-linearity of an accelerometer system as a function of input acceleration and u which is a ratio of displacement to finger gap. Loop gain of the system is adjusted to be 7 which is corresponding to a typical loop gain for accelerometer system studied in this thesis without including PI controller.

Loop transfer function of classical electro-mechanical sigma delta modulator is established in Equation 2.22 which states that loop transfer function comprises solely constant terms at DC. The system is transformed into Type-1 system by integrating PI controller which eliminates the steady state error for all input range by keeping the proof mass displacement $x = 0$. Thus, it is possible to achieve theoretically perfect

linear accelerometer system as illustrated in Figure 2-7 for the solution sets where $x = 0$.

2.6 Summary

In this chapter, electro-mechanical sigma delta modulation is introduced by examining the capacitive actuation and sensing mechanisms for the varying gap type MEMS accelerometer sensor and electronic sigma delta modulation. Methods to ensure stability of the electro-mechanical system are presented. Then, the effect of mechanical and electronic noise sources on the output are investigated by providing the output-referred noise formulations. Finally, non-linearity sources are revealed by analyzing the electro-mechanical accelerometer system, and simple yet elegant solution is presented to achieve zero steady-state error which results in perfectly linear electro-mechanical accelerometer system.

In the next chapter implementation of PI controller in to the electro-mechanical sigma delta accelerometer system is presented. There, the constructed 5^{th} order Type-1 electro-mechanical accelerometer system is analyzed, and improvement in the linearity performance is demonstrated together with the test results, for the first time in the literature.

CHAPTER 3

DESIGN AND IMPLEMENTATION OF THE NEW READOUT CIRCUIT

Effects of the PI controller on the linearity performance of the electro-mechanical sigma delta modulator are revealed in Chapter 2. There, it is stated that the displacement-dependent all non-linearity terms can be eliminated by inserting a PI controller into the electro-mechanical sigma delta accelerometer system. With this information in mind, design and implementation of an electro-mechanical sigma delta loop taking advantage of a PI controller is explained throughout this chapter, in order to achieve a high linearity performance. Section 3.1 gives information on the readout circuit studied in this thesis and the topology of electro-mechanical sigma delta modulator with PI controller. Section 3.2 provides design details of the proportional and integral controller inserted in to the sigma delta modulator loop. Section 3.3 explains the timing of the complete accelerometer system. Section 3.4 presents the serial interface to be used for adjusting on chip capacitors. Section 3.5 gives a top level layout and simulation results of the accelerometer readout circuit to demonstrate the functionality of the complete system. Finally, Section 3.6 summarizes this chapter.

3.1 Architecture of the New Readout Circuit

Main purposes of this thesis are to emphasize the importance of the PI controller in the electro-mechanical sigma delta modulator loops, and show the enhancement in the linearity performance of the accelerometer system. Thus, in the scope of this thesis 4^{th} order accelerometer system which was implemented in [18] is chosen as a

base circuit, and PI controller is inserted into this 4th order electro-mechanical sigma delta accelerometer system to achieve the high linearity performance.

Base circuit which was implemented as 4th order accelerometer system [18] uses unconstrained electro-mechanical sigma delta modulator topology which is firstly introduced by Raman et. al. [24]. Figure 3-1 presents the unconstrained electro-mechanical sigma delta modulator architecture firstly proposed in [24] and implemented as 4th order sigma delta modulator in [18].

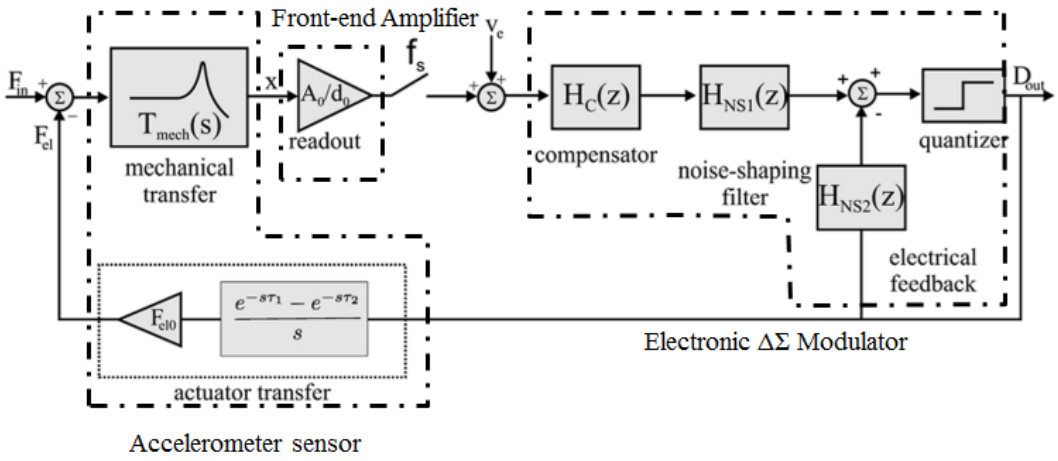

Figure 3-1: Architecture of the unconstrained mixed-feedback sigma delta modulator firstly proposed in [24] and realized as 4th order sigma delta modulator in [18].

There are two main block in the 4th order unconstrained sigma delta modulator which are front-end amplifier and 2nd order electronic sigma delta modulator. Front-end amplifier senses the capacitance difference between the accelerometer sensor electrodes, and converts the capacitance difference to voltage. Next, the 2nd order electronic sigma delta modulator encodes the incoming analog signal to pulse density modulated low resolution 1-bit digital signal which is fed back to the accelerometer sensor to keep the proof mass of the accelerometer sensor stationary.

In the scope of this thesis a PI controller is implemented, and inserted between the front-end amplifier and the 2nd order electronic sigma delta modulator. With the PI-controller included in the electro-mechanical sigma delta loop, a 5th order system

is realized. Figure 3-2 shows the complete architecture of unconstrained accelerometer system including PI controller, MEMS accelerometer sensor and supporting blocks. Multiphase clock generator is modified to provide required timing signal to each block, and also serial programming interface is included in the readout circuit to adjust internal on-chip capacitances easily.

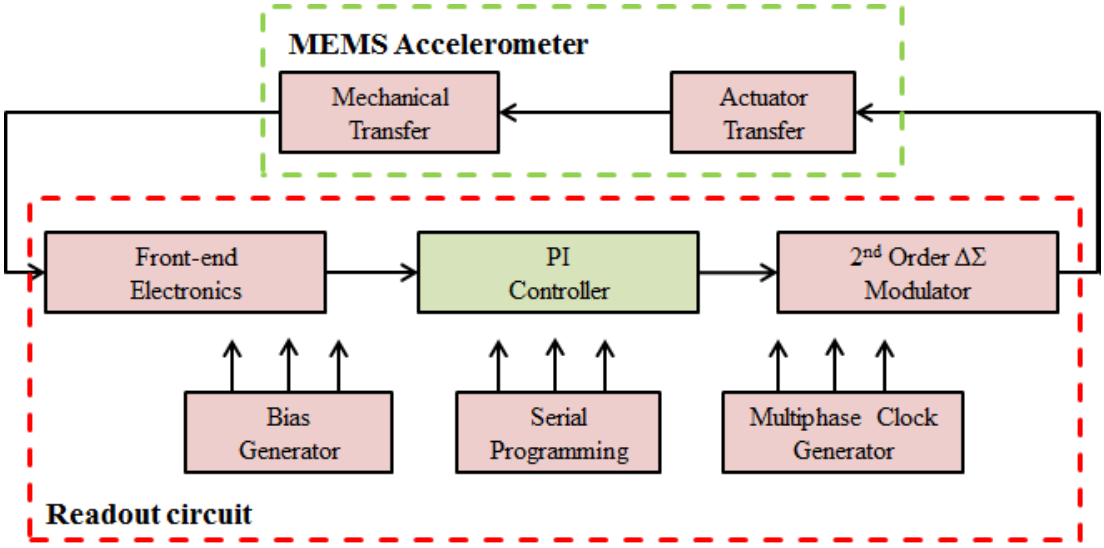

Figure 3-2: General architecture of unconstrained accelerometer system. 5th order EM sigma delta modulator is realized by inserting PI controller into the loop.

3.2 Proportional-Integral Controller Circuit

Proportional-integral controller is a critical circuit block in the electro-mechanical sigma delta modulator to eliminate the non-linearity problem arising from non-zero steady state error. This block is inserted between the front-end amplifier and the electronic sigma delta modulator blocks to linearize the accelerometer system with a high loop gain and to fulfill the stability requirements by adjusting the zero location of the controller.

During the design phase of the PI controller, electronic noise sources must be considered since the input referred noise of this block significantly degrades the overall noise performance of the accelerometer system. While the input referred noise can be suppressed with the help of electrostatic spring softening effect, special

care should be taken to minimize the effect of the offset and flicker noise of the PI controller block.

PI controller is implemented as two separate blocks, namely the proportional controller and integral controller. While the proportional controller is realized with a switched capacitor amplifier, the integral action is achieved by an auto-zero switched capacitor integrator. In order to observe the enhancement in the linearity performance of the system, the test results of the system while operating accelerometer system either with the P controller or with the PI controller needs to be compared. In order to conduct test either with the P controller or PI controller, the static switches are employed at the output nodes of the I-controller. These switches are controlled by user to enable/disable the connection between I-controller and following sigma delta modulator block. Thus, it is possible for user to enable/disable the integral action which is carried out by I-controller. Addition of proportional and integral controller output signals are carried out by the following multiple input electronic sigma delta modulator stage to realize the transfer function

$$H_{PI}(s) = K_P + \frac{K_I}{s} \tag{3.1}$$

where K_P and K_I are the proportional and integral gain.

Since the readout chip reported in [18] is utilized as the base circuit to insert PI controller, built in OTAs which are already employed in the front-end electronics and sigma delta modulator blocks of the readout chip reported in [18] are used to construct proportional and integral controller. In the subsections the operation of the controller is described and circuit analysis is presented to point out auto-zero action which eliminates input offset and flicker noise.

3.2.1. Proportional Controller

Offset compensated switched capacitor amplifier which is firstly introduced by [48] is realized to carry out proportional controller action. Figure 3-3 shows the schematic of the offset compensated proportional controller. The operation of the proportional controller in Figure 3-3 is quite simple. The circuit operation is described using the timing diagram presented in Figure 3-4.

P-controller operation starts with the ϕ_{rst} phase. In this phase inputs of the OTA are directly connected to the ground to help the OTA to correct its input common mode voltages. By this way, regular OTA operation is assured in the succeeding ϕ_{smp} phase.

After ϕ_{rst} phase, the circuit goes in to ϕ_{smp} phase. In this phase inputs of the OTA are disconnected from ground. OTA takes the buffer configuration and input voltage of the P-controller starts to be sampled on the C_1 capacitors. Note that common mode and differential offset values can be directly observed in the inputs of OTA since it is in buffer configuration. So, C_2 capacitor samples input offset voltages of the OTA during ϕ_{smp} phase. The total charge accumulated on the capacitors C_1 and C_2 during the ϕ_{smp} phase can be given as

$$Q_{C_1^+} = C_1(V_{in+} - V_{CM} - V_{DF+}) \quad 3.2$$

$$Q_{C_1^-} = C_1(V_{in-} - V_{CM} - V_{DF-}) \quad 3.3$$

$$Q_{C_2^+} = -C_2(V_{CM} + V_{DF+}) \quad 3.4$$

$$Q_{C_2^-} = -C_2(V_{CM} + V_{DF-}) \quad 3.5$$

where V_{CM}, V_{DF+} and V_{DF-} are the common mode offset voltage and differential offset voltages respectively.

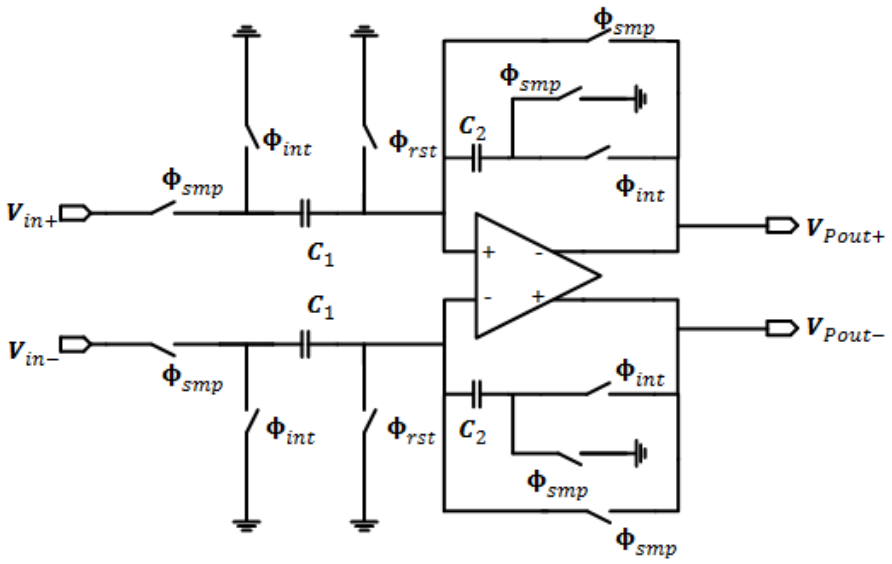

Figure 3-3: Proportional controller block schematic with offset compensation.

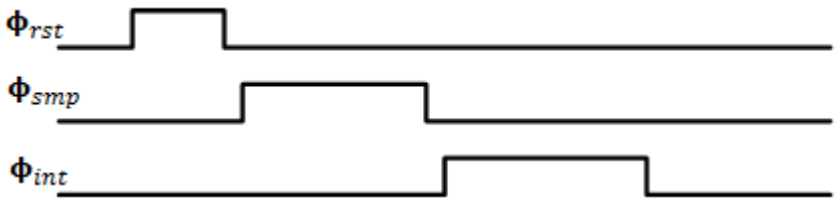

Figure 3-4: Timing diagram of the proportional controller.

Following to the sampling phase, integration phase of the amplifier starts with the ϕ_{int}. In this phase sampling C_1 capacitors are disconnected from the input voltage and its bottom plate is connected to ground. OTA leaves buffer configuration in integration phase, and C_2 capacitors are connected between the input and output terminals of the OTA. Charge transfer is accomplished between the C_1 and C_2 capacitors according to the charge conservation principle. Thus, assuming the offset voltages at the input terminal of the OTA remain constant, the remaining charges on the C_1 can be expressed as

$$Q_{C_1^+} = C_1(-V_{CM} - V_{DF+}) \quad 3.6$$

$$Q_{C_1^-} = C_1(-V_{CM} - V_{DF-}) \quad 3.7$$

By applying charge conservation principle and equating total charges in sampling and integration phase, the total charge on the C_2 capacitors can be found as in Equation 3.8 and Equation 3.9 at the end of integration phase.

$$Q_{C_2^+} = -C_2(V_{CM} + V_{DF+}) + C_1V_{in+} \quad 3.8$$

$$Q_{C_2^-} = -C_2(V_{CM} + V_{DF-}) + C_1V_{in-} \quad 3.9$$

Equation 3.10 and Equation 3.11 show the resulting output voltage level according to the charge transfer, and Equation 3.12 states the relation between input and output voltage levels.

$$V_{Pout+} = \frac{-C_2(V_{CM} + V_{DF+}) + C_1V_{in+}}{C_2} - (V_{CM} + V_{DF+}) \quad 3.10$$

$$V_{Pout-} = \frac{-C_2(V_{CM} + V_{DF-}) + C_1V_{in-}}{C_2} - (V_{CM} + V_{DF-}) \quad 3.11$$

$$\Delta V_{Pout} = \frac{C_1}{C_2}\Delta V_{in} \quad 3.12$$

With the Equation 3.12, proportional gain term with perfect offset cancellation is obtained. However, OTA has finite open loop gain in reality and this finite loop gain prevents complete offset cancellation. If the finite loop gain is considered in the calculation, the input to output voltage relation is given as

$$\Delta V_{Pout} = \frac{C_1/C_2}{1+(1+C_1/C_2)/A}\Delta V_{in} + \frac{V_{DF+}-V_{DF-}}{(1+C_1/C_2)A} \quad 3.13$$

where A is the open loop gain of the OTA. Equation 3.13 shows that although offset cancellation is limited with the open loop gain of the amplifier, significant amount of offset and $1/f$ noise cancellation is achievable with the auto-zero switched capacitor amplifier.

In the layout implementation of the P-controller, C_2 capacitors are selected to be $1.5\,pF$, and C_1 capacitors are realized with capacitor banks which can be adjustable between $0.5\,pF$ to $7.5\,pF$ with the $0.5\,pF$ steps. By using adjustable capacitor banks, P-controller gain can be altered between 1/3 and 5 which brings great flexibility to the system while tuning zero location of PI controller.

Cadence SpectreRF PSS and Pnoise analyses are conducted to extract the input referred noise of the P-controller. For the noise analysis of the switched capacitor amplifier, $maxacfreq$ and $maxsideband$ parameters in the SpectreRF is selected to be $100\,MHz$ and 20 respectively. Also, $analog\ reltol, vabstol$ and $iabstol$ parameters are set to $1e-5, 3e-8$ and $1e-13$ respectively in order to obtain accurate simulation results [49]. Figure 3-5 depicts the noise spectrum of the P-controller with unity gain configuration. Effect of the auto-zero action can be clearly seen in the noise spectrum of the P controller. Overall noise of the amplifier including the $1/f$ noise is suppressed below $100\ nV/\sqrt{Hz}$ at 1 Hz which is close to $95\ nV/\sqrt{Hz}$ thermal noise level of the system.

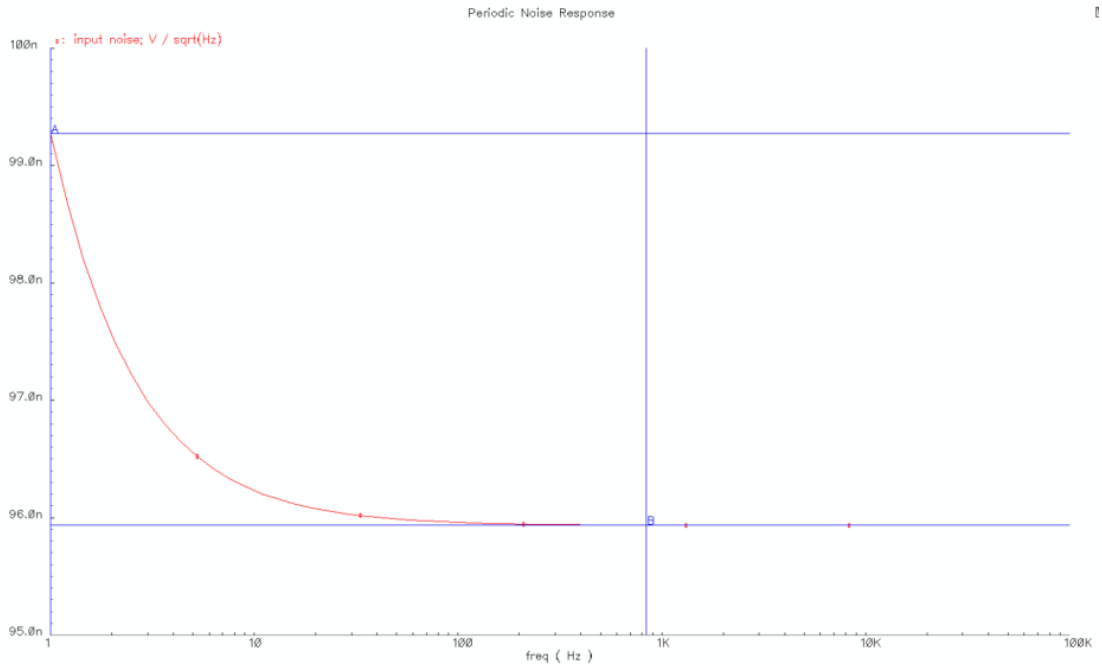

Figure 3-5: Noise spectrum of the P-controller showing flicker noise suppression for the unity gain configuration.

3.2.2. Integral Controller

Similar to the P-controller, I-controller also utilizes auto-zero function to cancel out offset and $1/f$ noise component at the baseband. Figure 3-6 illustrates the schematic of the auto-zero switched capacitor integrator. Operation principle of the integral controller is also simple and similar to the P-controller. Since both controllers have the same timing sequence, timing diagram in Figure 3-4 shall be considered while describing operation of the I-controller.

Operation of the I-controller also starts with ϕ_{rst} phase to help the OTA to balance its common mode voltages. After ϕ_{rst} phase, sampling (ϕ_{smp}) phase follows. In this phase OTA is altered to buffer configuration, and bottom plates of the C_4 capacitors are left floating to avoid any charge transfer on to these capacitors. C_3 capacitors are connected to the input terminals to sample input voltage in this phase. Considering OTA input offset voltages, in the sampling phase total charge accumulated on the C_3 capacitors are:

$$Q_{C_3^+} = C_3(V_{in+} - V_{CM} - V_{DF+}) \quad 3.14$$

$$Q_{C_3^-} = C_3(V_{in-} - V_{CM} - V_{DF-}) \quad 3.15$$

After ϕ_{smp} phase, the circuit enters ϕ_{int} phase by turning of sampling switches. In this phase, charges sampled on the C_3 capacitors are transferred to the C_4 capacitors according to the charge conservation principle. Note that bottom plates of the C_3 capacitors are still connected to the input nodes of the OTA showing same offset voltages with the previous sampling phase. Thus, at the end of integration phase total charge on the C_4 capacitors can be found as

$$Q_{C_4^+} = C_3 V_{in+} + Q_{prev,C_4^+} \quad 3.16$$

$$Q_{C_4^-} = C_3 V_{in-} - Q_{prev,C_4^-} \quad 3.17$$

where Q_{prev} is the previous charge on the C_4 capacitor.

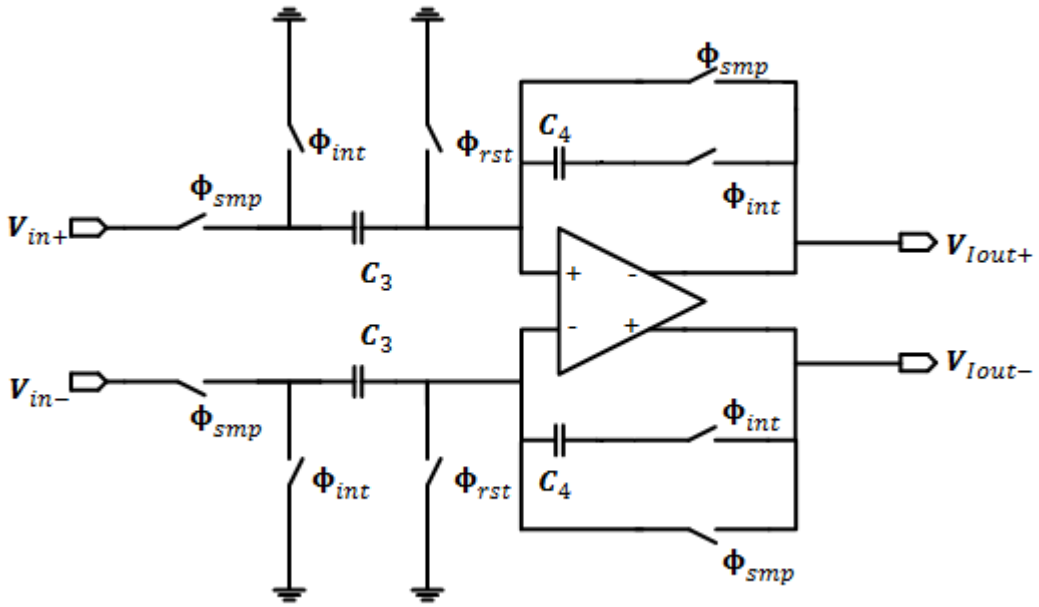

Figure 3-6: Integral controller block schematic with offset compensation.

Since previous charge on these capacitors never transferred, only charges sampled on C_3 capacitors are added to integration capacitors for each cycle. Assuming C_4

capacitors are discharged at the beginning of the integration operation, at the end of N cycle output voltages can be given as

$$V_{Iout+} = \sum_{i=1}^{N} \frac{C_3 V_{in+}(i)}{C_4} + V_{CM} + V_{DF+} \quad 3.18$$

$$V_{Iout-} = \sum_{i=1}^{N} \frac{C_3 V_{in-}(i)}{C_4} + V_{CM} + V_{DF-} \quad 3.19$$

Finally, Equation 3.20 gives the output voltage as a function of the input voltage,

$$\Delta V_{Iout} = \frac{C_3}{C_4} \sum_{i=1}^{N} \Delta V_{in}(i) + V_{DF} \quad 3.20$$

where V_{DF} is the differential offset voltage. Although integration action is validated with the summation term, there is still a differential offset term exists in the Equation 3.20. In order to emphasize the effect of auto-zeroing in the switched capacitor integrator, the output voltage needs to be considered at the end of N cycles assuming constant input voltage level. At the end of N cycle, the output voltage is expressed as

$$\Delta V_{Iout} = N \frac{C_3}{C_4} \Delta V_{in} + V_{DF} \quad 3.21$$

Equation 3.21 states that input voltage is amplified by $N\, C_3/C_4$ while the differential offset voltage is kept constant. This fact shows the suppression of the differential offset voltage by $N\, C_3/C_4$. Thus, the auto zeroing feature of the integrator plays an important role in the suppression of the offset and $1/f$ flicker noise observed in the baseband.

In the layout implementation of the I-controller, C_4 capacitors are selected to be $24\ pF$, and C_3 capacitors are realized with capacitor banks which can be adjustable between $0.1\ pF$ to $1.5\ pF$ with the $0.1\ pF$ steps.

Cadence SpectreRF PSS, Pnoise analysis is also conducted to extract input referred noise of the integrator using same simulation configuration described in the previous section. Figure 3-7 shows the input referred Pnoise analysis result of the integrator for C_3 and C_4 capacitors are adjusted to be $0.3pF$ *and* $24\ pF$.

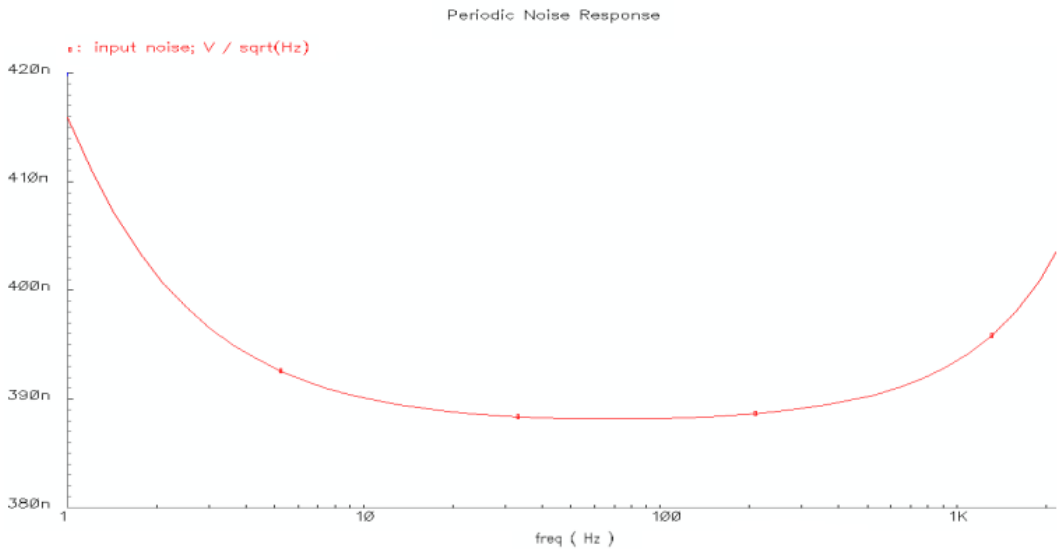

Figure 3-7: Noise spectrum of the I-controller with C_3 and C_4 capacitors are selected to be $0.3pF\ and\ 24\ pF$.

Integrator noise including $1/f$ noise is found to be $415\ nV/\sqrt{Hz}$ at 1 Hz in the simulations. For the auto zero integrator, $1/f$ and offset cancellation depends on the integrator gain as stated before. Thus, partial $1/f$ noise cancellation is achieved with the implemented I-controller.

Lastly, the input to output transfer function of PI controller in z-domain is formed. Remember that outputs of the P-controller and I controller are added in the multiple input electronic sigma delta modulator. Thus, the Equation 3.12 and Equation 3.21 can be combined in order to reveal the PI controller action. By neglecting the finite OTA gain and differential offset voltage, PI controller transfer function can be expressed in z-domain as

$$\frac{V_{out}}{V_{in}}(z) = \frac{C_1}{C_2} + \frac{C_3}{C_4}\frac{1}{z-1} \qquad 3.22$$

It is trivial to convert the Equation 3.22 into continuous time by substituting $z = e^{jwT_s}$. In the final form of transfer function approximate proportional gain K_p and integral gain K_I can be written as

$$K_P = \frac{C_1}{C_2} \qquad 3.23$$

$$K_I = \frac{C_3}{C_4 T_s} \quad 3.24$$

where T_s is the sampling frequency of PI controller. It can be clearly seen that the PI controller transfer function can be easily adjusted via the C_1 and C_3 capacitors which are implemented as capacitor banks.

3.3 Multiphase Clock Generator

The readout circuit consists of switched capacitor amplifiers and integrators, so multiphase clock generator is necessary to arrange the required timing signals to drive the switches employed inside the circuit blocks. Main clock source is supplied from the external PLL to drive multiphase clock generator precisely. Multiphase clock generator forms a series of timing signals to be used via each circuit block by referencing external clock source.

Readout circuit operation consists of successive feedback and sense phases. In the feedback phase readout circuit delivers constant amount of energy to the accelerometer sensor, while the electronic blocks operate one by one in the sense phase. If the one period of the external clock source is defined as a 1 cycle, multiphase clock generator reserves 23 cycles of time for the feedback and 23 cycles of time for the sense phase which is used by electronic blocks. Thus, the readout circuit needs a total of 46 clock cycles to carry out the feedback and sense phases. Also note that the readout circuit determines the 1-bit digital output at the end of 46 cycles which defines the sampling rate of the electro-mechanical sigma delta modulator.

The readout circuit comprises totally four stages that perform amplification or integration namely the front-end amplifier, PI controller block and electronic sigma delta modulator that includes two integrator stages. Therefore, all the electronic blocks should perform their task within sense phase which takes a total of 23 clock cycles. Figure 3-8 shows the timing diagram indicating number of cycles reserved by the multiphase clock generator for feedback phase, reset phase and each electronic block in the amplification or integration mode. Note that the settling time of the blocks plays an important role in the overall circuit performance. So that, the number

of cycles reserved for each electronic block are adjusted based on the capacitive loading and settling behavior of each block.

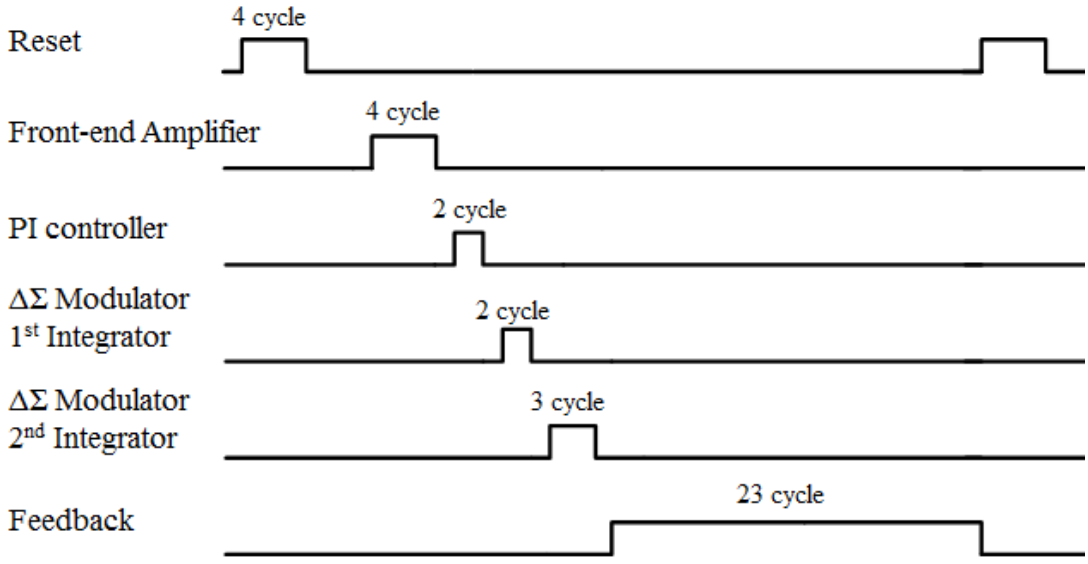

Figure 3-8: Timing diagram of the complete readout chip adjusted by the multiphase clock generator.

3.4 Serial Programing Interface

PI controller is realized with the capacitor banks which bring flexibility while adjusting zero location and gain of this block. Similarly, front-end amplifier and electronic sigma delta blocks include capacitor banks which are used for calibrating system stability and front-end gain. With this high programmability capacity, readout circuit can be integrated and operated with wide range of different accelerometer sensors. On the other hand, the high programmability capacity requires quite a few pads which should be connected to the inputs via wire bonds. This hardware-based programming feature increases the wire bonding work load, and wire bonds cannot be reconfigured to operate the accelerometer system for different conditions once the system package is sealed. In order to overcome these problems, a serial programming interface block, which was originally implemented in [50], is employed in the readout circuit. Hereby, the capacitor banks can be easily programmed prior to startup of readout circuit with the serial programming interface block as required.

Serial programming interface contains 20 cascaded register blocks which are formed by a $2x1$ multiplexer and a D flip-flop, and uses four input wires namely reset, clock, serial data and serial enable. Serial data wire is connected to the input of the first register while the remaining registers are fed by output of preceding register. Also, clock, serial enable and reset wires are connected to each register block separately.

The operation of serial programming interface is pretty simple. The data is fed to the input of the first register when serial enable is high. Similarly, the output of each register is fed to the input of the following register. Consequently, at the negative edge of the clock, input data is transferred to the output of the register. If the serial enable is low, then each register holds its value until the serial enable becomes high. Also, a reset pin is used to reset the flip flops. At the end of the programming, the serial enable is adjusted to be low. Thus, the output of each register determines the capacitor selection.

3.5 Top Level Implementation and Simulation Results

The top level implementation of the sigma delta modulator including PI controller is realized with the 0.35 µm XFAB CMOS process. Layout of the readout chip is given in Figure 3-9 including placement of each electronic block. Designed readout chip occupies an area of 2240 µm x 3450 µm and uses 49 pads. 4 pads are reserved for inspecting the output of the front-end amplifier and P-controller output while 2 pads are used for observing register outputs at the serial programming interface. 12 pads are employed in the top level layout as dummy pads, and the remaining pads are utilized for the supply voltages, serial programming interface, clock, reset and sensor interface.

It is important to verify the functionality of the readout chip at the end of implementation with post-layout simulations. Therefore, apart from the sub-block simulation of the P controller and I controller, a transient simulation is conducted for the complete readout chip. Two capacitors mimicking the accelerometer sensor are placed and connected with the accelerometer readout. These capacitors are adjusted to be $16\,pF$ with an approximately $0.2\,pF$ mismatch to observe the amplification of the capacitance difference at the output of front-end amplifier. Also, the outputs of

the P controller and I controller are recorded to demonstrate proper operation. Figure 3-10 shows the output of the front-end amplifier with $8pF$ integration capacitance when $200\,fF$ capacitance mismatch is introduced to the capacitances mimicking accelerometer sensor. The difference between the negative and positive output terminals of the front end amplifier is 75 mV which indicates approximately $17\,fF$ mismatch at the input terminals. With these simulations, the functionality of the sense mechanism which is the capacitance to voltage conversion taking place in sensor interface electronics is verified. It is also important to highlight that the capacitance mismatch at the input terminals are aimed to be kept at minimal level in order to avoid offset at the output of the accelerometer system.

Figure 3-11 and Figure 3-12 present the output of the P-controller block with unity gain configuration and output of the I-controller after 13 integration cycles with the gain of $0.8/24$. Voltage levels at the output of the controller blocks are recorded as 76 mV and 32 mV indicating proper integration and amplification operation at the end of 13 integration cycle.

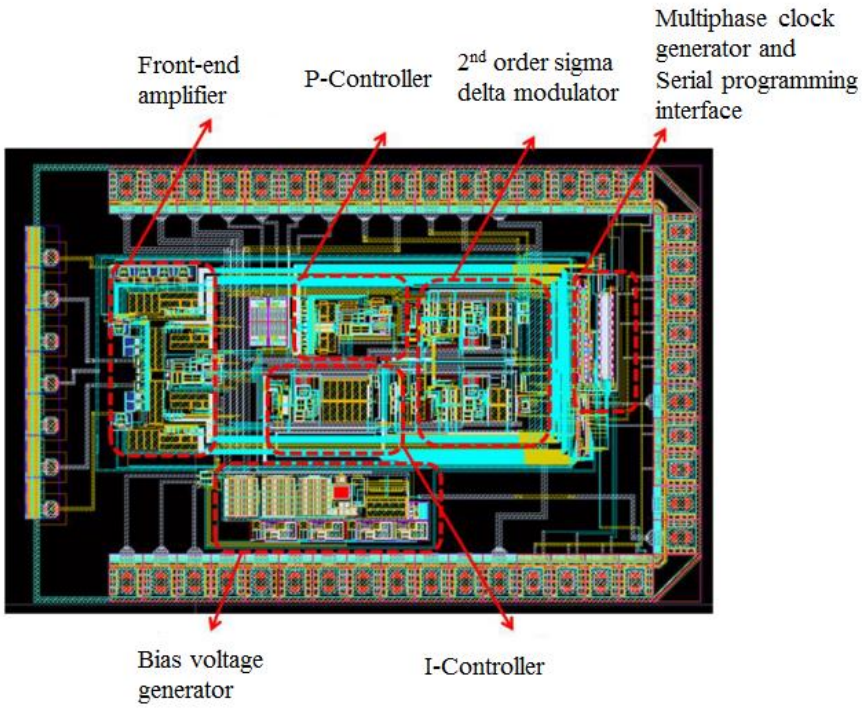

Figure 3-9: Layout of the complete readout chip.

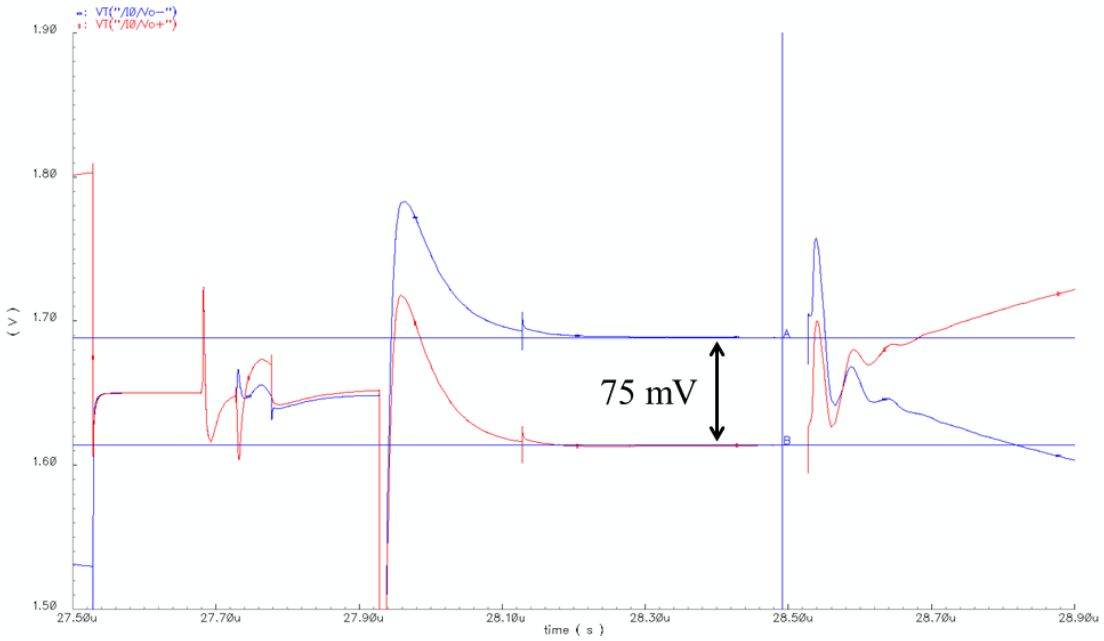

Figure 3-10: Pad level simulation result of the front-end amplifier. Output voltage is recorded as 75 mV for 200 fF mismatch in accelerometer capacitances.

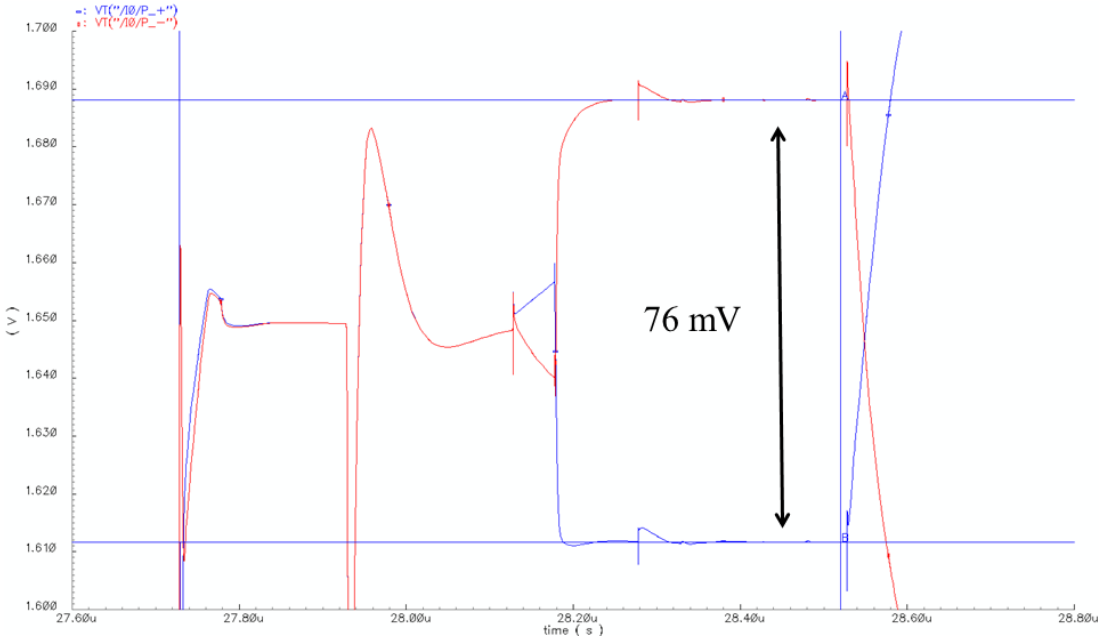

Figure 3-11: Pad level simulation result of the P-controller with unity gain configuration registering 76 mV output voltage which verifies the amplification operation.

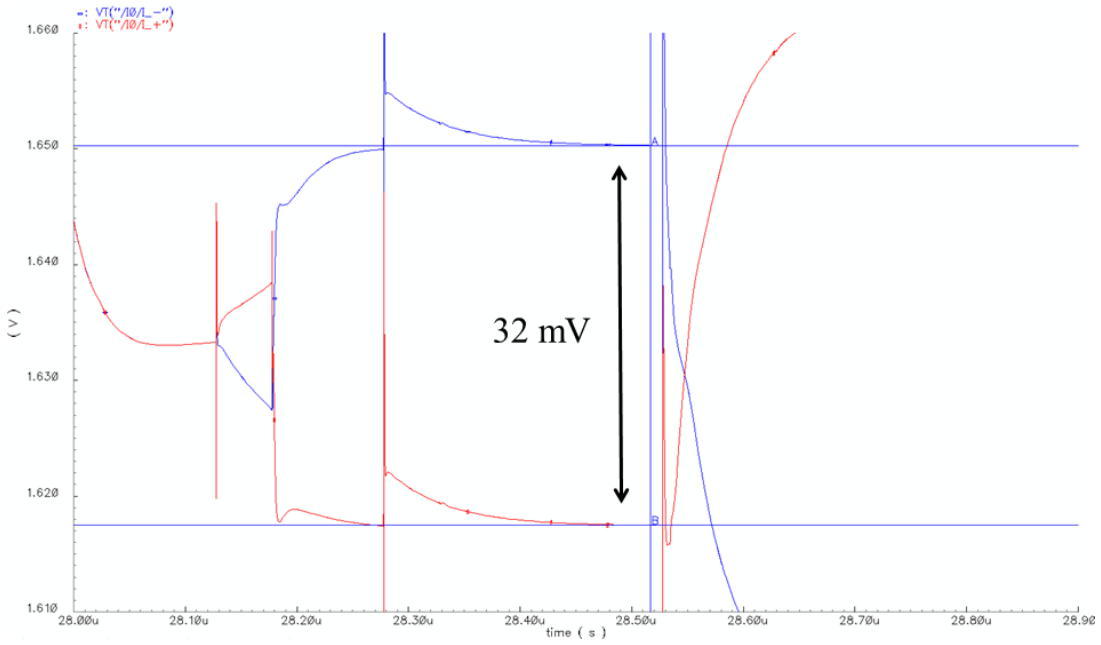

Figure 3-12: Pad level simulation result of I controller with the gain of $0.8/24$. The output voltage is observed as $32\ mV$ verifying proper integration operation at the end of 13 integration cycle.

Additionally, the digital output of the readout chip and transient voltage levels at the sensor interface need to be monitored to verify the feedback mechanism and pulse density modulation feature of sigma delta modulator. Figure 3-13 shows the voltage levels at the sensor interface and digital output of the readout chip. The pulse train with a peak amplitude of 3.3 V is seen at the proof mass which is referred as VB in the Figure 3-13. These pulses are applied at the sense phase to transfer the charge accumulated on the sensor plates to the front-end amplifier. Also, it is seen that the voltage levels at the electrodes are either 9 V which is the feedback voltage or 0 V. Pulse density modulated feedback pulses observed on the electrodes proves the proper feedback mechanism. Similarly, pulse density modulation behavior of the sigma delta modulator is confirmed by monitoring feedback pulse sequence of electrodes and the digital output of the readout circuit.

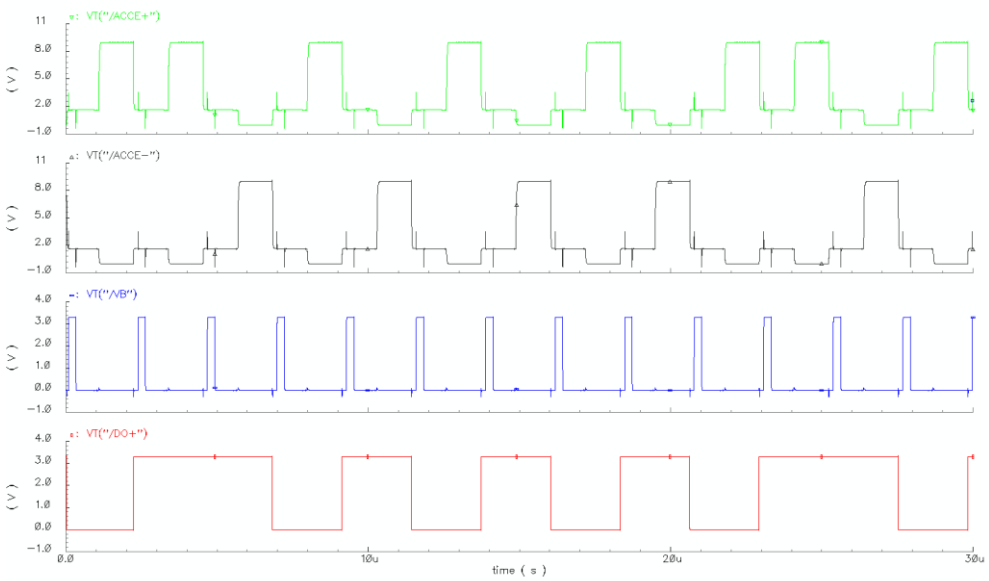

Figure 3-13: Pad level simulation result of accelerometer electrodes, proof mass and digital output of readout chip.

3.6 Summary

After revealing the importance of the PI controller in Chapter 2 for an ordinary electro-mechanical sigma delta modulator to achieve high linearity performance, design and implementation of a readout chip taking advantage of PI controller to achieve zero steady state error is presented in this chapter. The architecture of the base circuit which is implemented as unconstrained 4th order system [18] is introduced briefly, and the new readout circuit architecture including PI controller is explained. The main focus in this chapter is the implementation of the PI controller. Thus, a detailed analysis on the P-controller and I-controller is performed to clarify the operation principle of these blocks and auto-zero action for reducing the flicker noise. Noise simulation techniques for SpectreRF are also discussed for the PI controller block. Finally, transient simulation results of the complete readout chip are given to prove the functionality of the readout chip.

The next chapter focuses on the non-linear model simulation results for the implemented readout chip including the PI controller. These simulation results are compared with the previous work, and improvement on the linearity performance is accomplished without degrading noise performance of the accelerometer system.

CHAPTER 4

DESIGN OF A 5TH ORDER ACCELEROMETER SYSTEM

The implementation of the flexible 5th order accelerometer system is described in Chapter 3. The next step is the design of the system parameters to achieve the maximum performance for a specific MEMS accelerometer sensor. The high-order sigma delta modulator suffers from stability as the order of modulator increases, and it requires careful design to ensure stability while suppressing the quantization noise below overall circuit noise. The linearity of the system is the main concern for this thesis as well as the overall circuit noise, so PI controller parameters should be adjusted to achieve minimal steady state error while considering closed-loop response of the system. Shortly, the system parameters need to be determined to ensure proper operation during the experiments.

This chapter focuses on the design of the 5th order accelerometer system. Section 4.1 provides information of the MEMS accelerometer sensor utilized in the accelerometer system, also introduces adjustable system parameters. Section 4.2 analyzes the stability of the accelerometer system with non-linear model simulations and presents the transient response of the system for varying system parameters. Section 4.3 gives the noise performance of the designed accelerometer system by comparing the non-linear model simulations and hand calculation. Section 4.4 gives the linearity performance of the 5th order accelerometer system and compares the results with the accelerometer utilizing only P-controller. Finally, Section 4.5 summarizes the chapter.

4.1 5th Order Accelerometer System Parameters

In Chapter 2, the theory of the electro-mechanical sigma delta modulator system is established. Now it is time to calculate system gain coefficients and mechanical transfer function for a specific MEMS accelerometer. In the scope of this thesis, capacitive MEMS accelerometer which is designed and fabricated in METU-MEMS is utilized in the construction of the 5th order accelerometer system. Table 4-1 presents the parameters of the capacitive MEMS accelerometer.

With the parameters for this specific accelerometer, feedback voltage, sampling time and duty cycle of the readout chip need to be determined to calculate the transfer functions of blocks that is used in the analysis of the system performance. The readout circuit needs a feedback voltage between 6 V and 14 V for operational sensor interface, and feedback voltage noise increases according to the Equation 2.20 as the feedback voltage amplitude rises. Thus, the feedback voltage is chosen to be its minimal amplitude $V_{fb} = 6V$ for the analysis and non-linear simulations to keep the contribution of feedback voltage noise at its minimum. In addition, the selected feedback voltage is not an optimum voltage amplitude zeroing effective spring constant but it sufficiently reduces the effective spring constant to keep the electronic noise below Brownian noise level. Note that in the case of excessive electronic noise or need for a higher detectable input range, this voltage can be further optimized to decrease the electronic noise and to increase input range according to the Equation 2.16.

It is also important to consider the duty cycle of the feedback and sense mechanisms during the calculation of transfer functions. The readout circuit cannot continuously apply feedback voltage onto the electrodes of the MEMS accelerometers since the capacitive sensing is also performed with the same electrodes. Thus, feedback duty cycle is adjusted to be 50% in the readout circuit. 50% feedback duty cycle is considered by multiplying the derived equations with 0.5 during the calculation of voltage to force gain and electrostatic spring constant.

Table 4-1: Parameters of the MEMS accelerometer which is designed and fabricated at METU-MEMS. MEMS accelerometer sensor is integrated with the readout circuit to form 5th order accelerometer system.

Parameter	Units
m	73.2 μg
k	24.9 N/m
b	0.004 Ns/m
d_1	2.7 μm
d_2	6.7 μm
A	3.33 μm^2
Number of Fingers	576

Other than the feedback voltage, the sampling frequency of the system should be determined prior to the analysis. The sampling frequency of the system is limited with the speed of the electronic blocks, and it should be set as high as possible to suppress the quantization noise of the system while giving adequate time to electronic block to settle. Therefore external clock frequency is selected to be $23\,MHz$ which results in a sampling frequency of $500\,kHz$ by considering the readout circuit speed. Actually the speed of the system can be increased up to $1\,MHz$; however 500 kHz sampling time is used in order to be on the safe side. With the predefined feedback voltage and sampling frequency settings, transfer functions and gain coefficients can be tabulated as in the Table 4-2 using the equations derived in Chapter 2. Note that C_{int} and $C_{fb}$are the adjustable integration and feedback capacitances employed in the front-end amplifier and electronic sigma delta modulator respectively. While, these adjustable capacitors are used to alter loop gain, C_{fb} plays an important role to adjust the stability of the sigma delta modulator as discussed in [18]. Since adjustable circuit parameters which are integration capacitance, feedback capacitance, proportional gain and integral gain are not determined yet, transfer functions which contain adjustable parameters are given in terms of adjustable circuit parameters in the Table 4-2. It can be clearly seen that, almost all of the gain coefficients and transfer functions of readout circuit can be altered to establish stable operation according to the mechanical transfer function.

This feature of the readout circuit brings great flexibility to achieve a stable accelerometer system with low noise and high linearity.

Table 4-2: Transfer functions and gain coefficients of the 5th order accelerometer system with predefined sampling frequency, feedback voltage and accelerometer sensor transfer function. Note that the adjustable circuit parameters are not determined yet. These adjustable parameters are selected considering the stability, noise and linearity in the further sections.

Symbol	**Equation**	**Definition**
t_s	$500\ kHz$	Sampling frequency
V_{fb}	$6\ V$	Feedback voltage
dC/dx	$1.95e-6\ F/m$	Capacitance sensitivity
k_e	$16.5\ N/m$	Electrostatic spring constant
K_{fe}	$\frac{1.29e-5}{C_{int}}$	Front-end amplifier gain C_{int} can be adjusted between 1 pF and 15 pF with 1 pF steps
K_{mod}	$\frac{0.46e-12}{C_{fb}}$	Electronic sigma delta modulator gain C_{fb} can be adjusted between 0.1 pF and 1.5 pF with 0.1 pF steps
K_{VF}	$1.75e-5$	Voltage to force gain
H_{PI}	$K_P+\frac{K_I}{s}$	Transfer function of PI controller K_p can be adjusted between $1/3$ and 5 K_I can be adjusted between $2e3$ and 31e3
H_{comp}	$\frac{11.67z-10.67}{z}$	Transfer function of lead compensator embedded into sigma delta modulator
H_{acce}	$\frac{1.366e7}{s^2+\ 5.464e4s+3.402e8}$	Force to displacement transfer function of accelerometer sensor

Most of the accelerometer system in the sigma delta modulator employs separate lead compensation circuit inserted into the loop, but it is embedded into the electronic sigma delta modulator with extra feed-forward path in the unconstrained

mixed-feedback sigma delta modulator architecture [24]. Since the accelerometer system implemented in unconstrained mixed-feedback architecture, lead compensator transfer function is derived according to the parameters given in [18]. Also note that while the lead compensator provide considerable amount of phase margin at frequencies above few kHz, it does not affect the phase and gain of the system at baseband. So, the lead compensation effect can be neglected in the noise and linearity calculations while it should be included in the formulations for stability analysis.

4.2 Stability Analysis and Closed Loop Response

Stability of the system is a major concern for the high-order electro-mechanical sigma delta modulators. Thus, the complete system should be analyzed thoroughly and non-linear model simulations should be performed to verify the stability of the 5^{th} order accelerometer system. Figure 4-1 shows the MATLAB-Simulink model to of the 5^{th} order electro-mechanical sigma delta modulator which is utilized to verify system stability. Accelerometer sensor, electronic sigma delta modulator and PI controller is included as transfer function in this model while front-end amplifier is realized as simple gain stage.

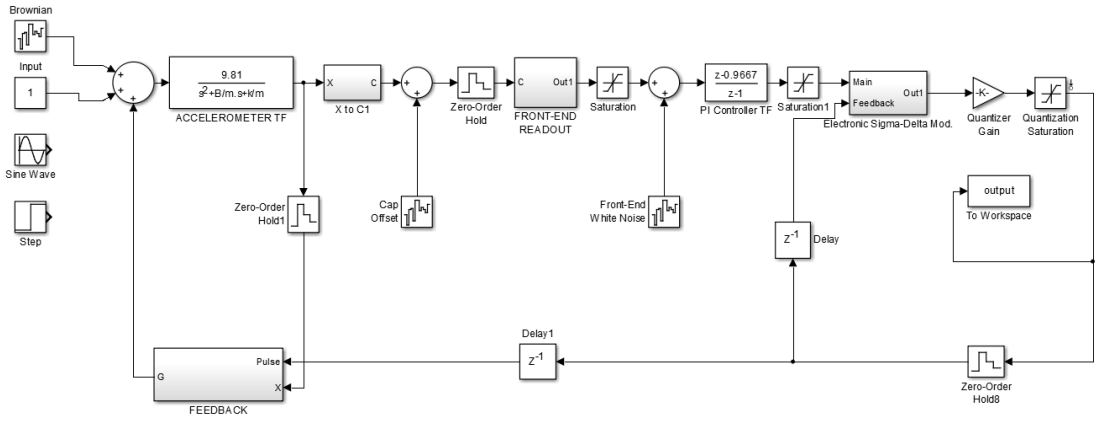

Figure 4-1: SIMULINK model of the 5th order electro-mechanical sigma delta modulator.

Feedback capacitance which is employed in the electronic sigma delta modulator is the most critical adjustable circuit parameter due to the chaotic behavior of sigma delta modulators to achieve stable operation. While larger feedback capacitance values enhance the stability of the sigma delta modulator by improving the tolerance of the accelerometer system to gain variations and varying input signal amplitudes, increase in the feedback capacitance causes degraded noise shaping performance resulting in higher in-band quantization noise. So, for the initial simulations of the non-linear model, front-end amplifier and controller gain are maximized by selecting $C_{int} = 1\,pF$ and $K_P = 5$, since the maximum gain configuration is the most susceptible configuration to unstable operation. In addition, feedback capacitor is selected to be $C_{fb} = 0.1\,pF$ which is the minimum capacitor size to push the system to its stability limit while experiencing minimum quantization noise.

In sigma delta modulators or electro-mechanical systems including electronic sigma delta modulator, system instability can be directly understood by observing the quantizer output. If the quantizer output is saturated at a constant level, the system is said to be instable. In order to examine the stability of the accelerometer system with $C_{int} = 1\,pF, K_P = 5$ and $C_{fb} = 0.1\,pF$ configuration, quantizer output is observed in non-linear model simulations. However, instable transient response which appears as saturated quantizer output is observed in these simulations conducted for different K_I values. After that feedback capacitance value is increased up to $C_{fb} = 0.3\,pF$ to obtain stable transient response. While increasing C_{fb} provides unconditionally stable system, there is a tradeoff between stability and the quantization noise. For smaller feedback capacitance noise shaping behavior of the system gets aggressive, and inversely in band quantization noise becomes visible for higher values of feedback capacitance. Also, since integrator output of the controller is directly connected to the electronic sigma delta modulator, saturation condition of the PI controller should be considered. Increasing the feedback capacitance indefinitely causes the PI-controller to saturate with small inputs. Thus, it is important to set the feedback capacitance to a minimum value considering stability. Based on the tradeoff between stability, quantization noise and PI-controller saturation, $C_{fb} = 0.4\,pF$ configuration is the best choice which achieves stable operation with maximum input range and low quantization noise.

While maintaining stable operation, it is also important to minimize the effect of electronic noise. Thus, front-end amplifier gain should be increased by decreasing the integration capacitor size to minimize the effect of electronic noise. For this reason, minimum integration capacitor which is $C_{int} = 1\,pF$ is selected. After a few iterations, controller parameters K_P *and* $K_I$are set to 0.66 and 25000 respectively to achieve approximately 60^0 phase margin. With the determined circuit parameters open loop transfer function becomes

$$H_{OL} = \frac{5.23\text{e}10s^2 + 4.51e15s + 8.743e19}{s^4 + 1.055\text{e}06\,s^3 + 5.498\text{e}10\,s^2 + 3.402\text{e}14\,\text{s}} \qquad 4.1$$

Bode diagram of the open loop transfer function stated in Equation 4.2 is given in Figure 4-2 which shows 62^0 phase margin for the 5th order sigma delta modulator. Transient response of the controller can be obtained with the non-linear model simulation to observe the settling behavior of the accelerometer system for the configuration $C_{int} = 1\,pF, C_{fb} = 0.4\,pF, K_P = 0.66$ and $K_I = 25000$. Figure 4-3 shows the response of the controller for $10g$ step input achieving approximately 0.2 $msec$ settling time.

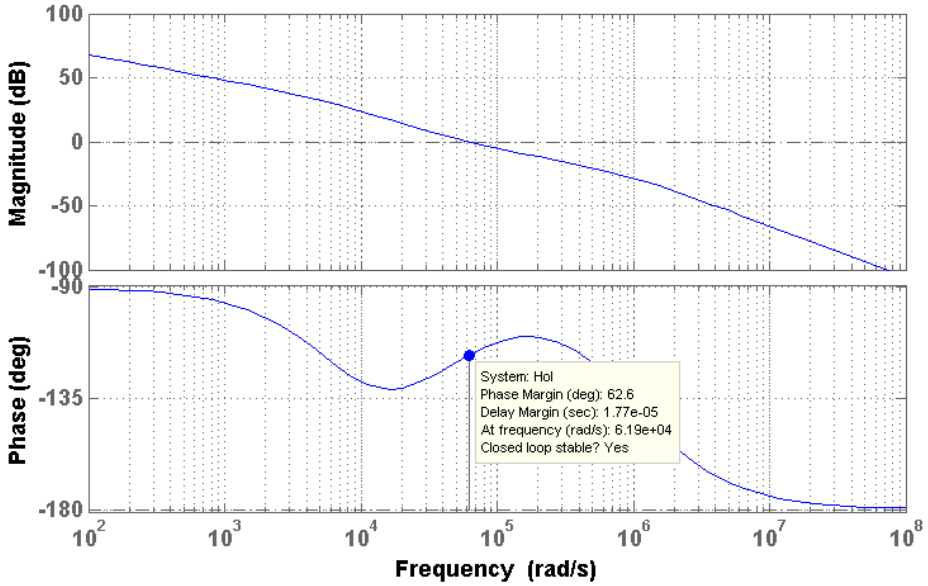

Figure 4-2: Bode diagram of accelerometer system open loop transfer function showing 62^0 phase margin.

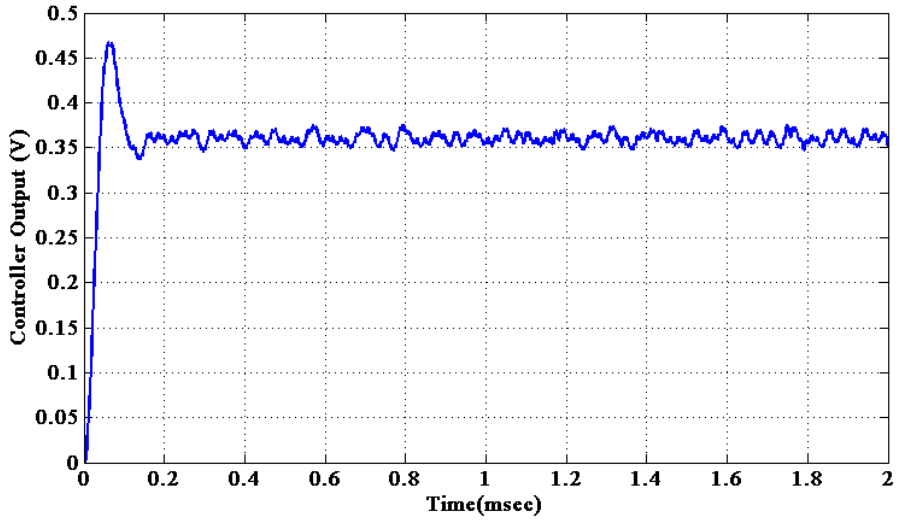

Figure 4-3: Transient response of the PI-controller showing less than $0.2\,msec$ settling time for 10g step input.

In summary, in order to select adjustable circuit parameters, transient response of the quantizer is observed to ensure the stability of the sigma delta modulator and bode diagram is used to achieve approximately 60^0 phase margin. Firstly, feedback capacitance is increased until stable operation is obtained, and feedback capacitance is adjusted to its minimum value to increase noise shaping performance ensuring stable operation. Then, front-end gain is maximized to reduce effect of electronic noise. Lastly, controller parameters are selected to tune phase margin around 60^0, and design phase of circuit which is the determination of adjustable circuit parameters is finalized.

4.3 Noise Performance of the 5th Order Accelerometer System

Noise simulations and calculation of each noise source is necessary for the 5th order accelerometer system to determine the contribution of each noise source and reveal the tradeoff between readout circuit parameters and noise performance. Non-linear model constructed in MATLAB-Simulink environment are used to extract the contribution of each individual noise source and simulation results are compared with the calculations. Calculations and simulation are performed for $C_{int} = 1\,pF$,

$C_{fb} = 0.4\,pF, K_P = 0.66\ and\ K_I = 25000$ configuration which is determined considering stability of the system.

The Brownian noise level of the MEMS accelerometer can be calculated as $11.4\ \mu g/\sqrt{Hz}$ by using Equation 2.19 and parameters tabulated in Table 4-1. Since the mechanical noise level of the accelerometer sensor directly depends on the sensor parameters, optimization of any readout circuit parameters does not help reducing the Brownian noise level. But, it is possible to push the electronic noise down to a level below the mechanical Brownian noise limit.

By estimating the feedback voltage noise as $400\ nV/\sqrt{Hz}$ [51], the contribution of the feedback voltage source can be calculated as $3.3\ \mu g/\sqrt{Hz}$ using Equation 2.20 which is derived for the electro-mechanical accelerometer system. Remember that the contribution of feedback voltage noise stated in Equation 2.20 is directly proportional to the voltage level. Besides, voltage noise of the feedback supply also increases almost proportionally with the feedback voltage level. These two facts reveal the tradeoff between the input range and noise of the overall system. Both the noise level and input range of the system are proportional to V_{fb}^2. So, low noise operation could be achieved by decreasing the feedback voltage amplitude until the contribution of supply noise is dominated by other noise sources. On the contrary by increasing the feedback voltage amplitude and insuring the overall noise floor is dominated by the feedback supply noise, maximum dynamic range can be achieved.

Finally, electronic noise which is referred to the front-end amplifier output is considered. By using the designed system parameters, electronic white noise of the system is approximately extracted as $300\ nV/\sqrt{Hz}$ mostly dominated by the I-controller block in SpectreRF simulations. The contribution of the electronic noise is calculated as $0.3\ \mu g/\sqrt{Hz}$ with the help of Equation 2.21.

By using the spring softening effect it is possible to reduce contribution of electronic noise according to the Equation 2.21 in the case of excessive electronic noise dominating overall input referred noise. However, spring softening effect is not the only way to avoid contribution of electronic noise. In 5th order electro-mechanical system, electronic noise illustrated in Figure 2-6 is mostly dominated by I-controller.

Therefore, front-end amplifier gain can be increased to minimize the effect of the electronic noise or adjustable capacitance controlling integral gain can be configured at much larger values in the case of excessive electronic noise until contribution of electronic noise gets smaller than Brownian noise level without using electrostatic spring softening effect.

Effective spring constant term exists as a proportional term in the Equation 2.21. In the case of a MEMS accelerometer with a high spring constant and an insufficient front-end amplifier gain, the system noise performance suffers from the electronic noise due to this effective spring constant term. The solution for such a system is simple: electrostatic spring softening effect. The feedback voltage level should be adjusted to lower the effective spring constant such that the overall noise of the system is dominated by other noise sources. Note that, while increasing feedback voltage to take the advantage of electrostatic spring effect and suppress electronic noise, the effect of feedback voltage noise should also be considered to obtain low noise performance.

Figure 4-4 and Figure 4-5 shows the noise simulation results of the designed accelerometer system. Figure 4-4 presents the noise PSD including feedback voltage noise and front-end amplifier output referred electronic noise compared with the calculated white noise floor at baseband. Figure 4-5 also presents the noise PSD with all noise sources included in the simulation. It can be seen that noise calculation that is performed to extract the white noise floor at baseband is in good agreement with the simulation results. Note that, calculation for the quantization noise level is not performed. Instead, it is observed with the simulations that the quantization level of the 5th order accelerometer system is below 0.5 $\mu g/\sqrt{Hz}$.

From the calculations and simulation results, the overall noise of the 5th order accelerometer system is expected to be $-98.5\ dBg/\sqrt{Hz}$ which corresponds to 11.9 $\mu g/\sqrt{Hz}$. The total noise value is dominated by the Brownian noise which is calculated as 11.4 $\mu g/\sqrt{Hz}$ using Equation 2.19 and sensor parameters tabulated in Table 4.1. Finally, Table 4-3 summarizes the contribution of each noise source for designed accelerometer system.

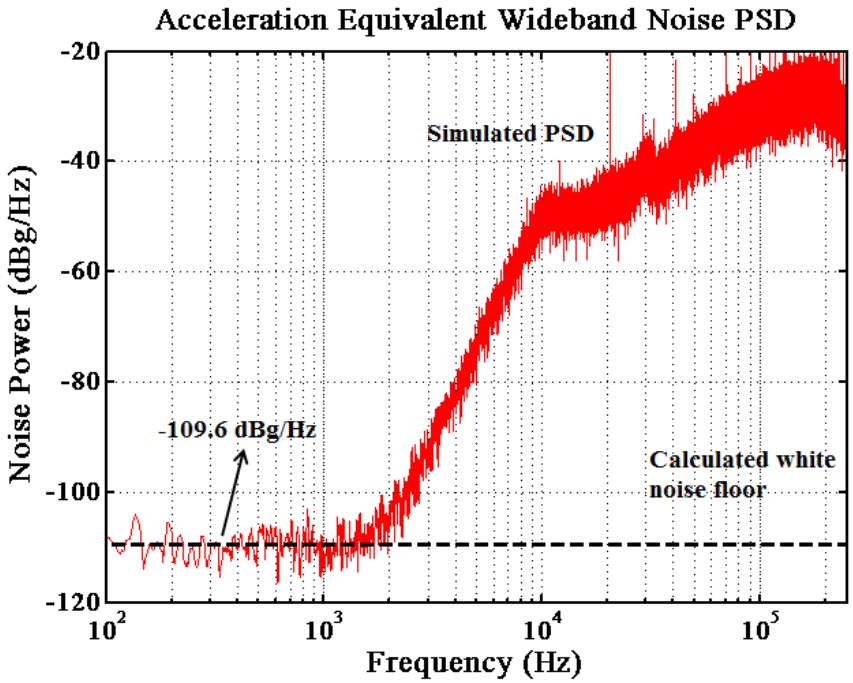

Figure 4-4: Noise spectral density of the simulated accelerometer system including feedback voltage and readout circuit noise. The simulation results are in good agreement with the calculated white noise floor.

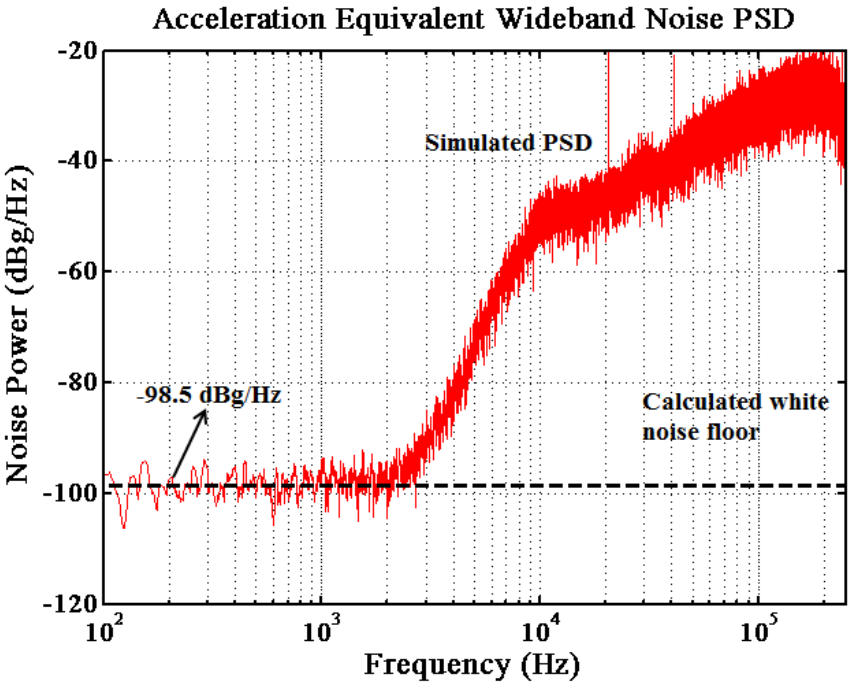

Figure 4-5: Noise spectral density of the simulated accelerometer system including Brownian noise, feedback voltage and readout circuit noise. The simulation results are in good agreement with the calculated white noise floor.

Table 4-3: Simulated noise contribution of each individual noise source for the configuration $C_{int} = 1\ pF, C_{fb} = 0.4\ pF, K_P = 0.66\ and\ K_I = 25000$.

Noise Source	Noise Magnitude	Acceleration equivalent noise power
Brownian Noise	$11.4\ \mu g/\sqrt{Hz}$	$-98.8\ dBg/\sqrt{Hz}$
Feedback Voltage Noise	$400\ nV/\sqrt{Hz}$	$-109.6\ dBg/\sqrt{Hz}$
Readout Circuit Noise	$300\ nV/\sqrt{Hz}$	$-130.4\ dBg/\sqrt{Hz}$
Quantization Noise	$0.5\ \mu g/\sqrt{Hz}$	$-126.0\ dBg/\sqrt{Hz}$
Overall Output Noise	$11.9\ \mu g/\sqrt{Hz}$	$-98.5\ dBg/\sqrt{Hz}$

4.4 Linearity Performance of 5th Order Accelerometer System

The linearity performance of the 5th order accelerometer is simulated with the non-linear MATLAB-Simulink model. Also, calculations are performed based on the theory established in Chapter 2.

Considering Figure 2-7 and the ideal integrator model with infinite OTA gain, it is expected to achieve a perfect linear system. However due to the finite gain of the OTA employed in the I-controller, this block shows a leaky behavior which limits the maximum integral gain at DC. Although the effect of leaky behavior is negligible on the linearity performance of the system, this effect is considered for the sake of completeness.

The OTA utilized in the I-controller has a gain of $80\ dB$. By considering this finite gain of the OTA, transfer function of I-controller with $K_I = 25000$ can be roughly approximated as

$$H_I = \frac{0.05z}{z - 0.9999} \tag{4.1}$$

Equation 4.1 states that due to the leaky integrator behavior, the gain of this block is limited with the $54\ dB$ at low frequency band including DC. Apart from gain of the I-controller, the loop gain of the system can also be calculated using Equation 2.22 as 16 dB for the designed system with $C_{int} = 1\ pF, C_{fb} = 0.4\ pF, K_P = 0.66$

and $K_I = 25000$ excluding contribution of I-controller. It can be seen that I-controller significantly boosts the loop gain of the system to 70 dB despite the fact that leaky integrator behavior limits the gain at DC.

The formulation stating steady state error is given in Equation 2.23. By using this equation, displacement of the proof mass can be found as $0.08\,nm$ for the condition of $10\,g$ input acceleration and 70dB loop gain as in the case with the designed accelerometer system. The displacement vector is calculated in the -10g to 10g range with 1g steps and closed loop output of the system is extracted using Equation 2.33. With the obtained output acceleration vector ranging from -10g to 10g, non-linearity of the accelerometer system is extracted to be below 1 ppm after applying linear fitting. To illustrate the effect of I-controller, system loop gain is decreased to 50 dB by configuring $C_{int} = 10\,pF$ which results in $0.8\,nm$ displacement for the same 10g input condition. The non-linearity of the system is still calculated to be below $1\,ppm$ using the same approach.

In order to compare the calculation results with the simulations, the input acceleration is applied to the system in the range of -10g to 10g with 1g steps. Then, non-linearity of the system is extracted to be below $1\,ppm$ which shows good agreement with the calculation by applying linear curve fitting

Also, 10g static input acceleration is applied to the system to compare the calculated displacement which is the main source of non-linearity in the MATLAB Simulink simulation. Figure 4-6 shows the displacement output of the accelerometer sensor for $C_{int} = 10\,pF, C_{fb} = 0.4\,pF, K_P = 0.66$ and $K_I = 25000$. Since the steady state error at the displacement output is small, integration capacitor C_{int} is set to $10\,pF$ intentionally for this simulation to ease the comparison. Steady state error is extracted as $0.6\,nm$ which shows adequately good agreement with the calculations.

As illustrated in Figure 4-6, 5^{th} order electro-mechanical sigma delta modulator achieves almost zero steady state error with the help of I-controller and manages to linearize accelerometer system perfectly even with the low front-end amplifier gain. Although perfect linear system is obtained by including I-controller in the loop, calculations and simulations without including I-controller need to be performed to emphasize the enhancement in linearity performance.

The loop gain of the accelerometer system excluding the I-controller can be found as 6.2 for $C_{int} = 1\,pF$ using Equation 2.22. For 10 g input acceleration the resulting displacement is found to be $40\,nm$ using Equation 2.23. Figure 4-7 presents the simulation result presenting displacement output of the accelerometer for the $C_{int} = 1\,pF$ configuration showing good agreement with the simulation results.

Displacement values are also calculated for the -10g to 10g range and output response of the system is recorded with the help of Equation 2.33. By using same linear curve fitting method, the non-linearity of the system is calculated to be $91\,ppm$. Additionally, calculations are repeated for the $C_{int} = 10\,pF$ resulting in a non-linearity of $1368\,ppm$. MATLAB-Simulink simulations are also performed for $C_{int} = 1\,pF$ and $C_{int} = 10\,pF$ configuration which result in 119 ppm and 1350 ppm non-linearity respectively. As can be seen calculation and simulation results are in good agreement.

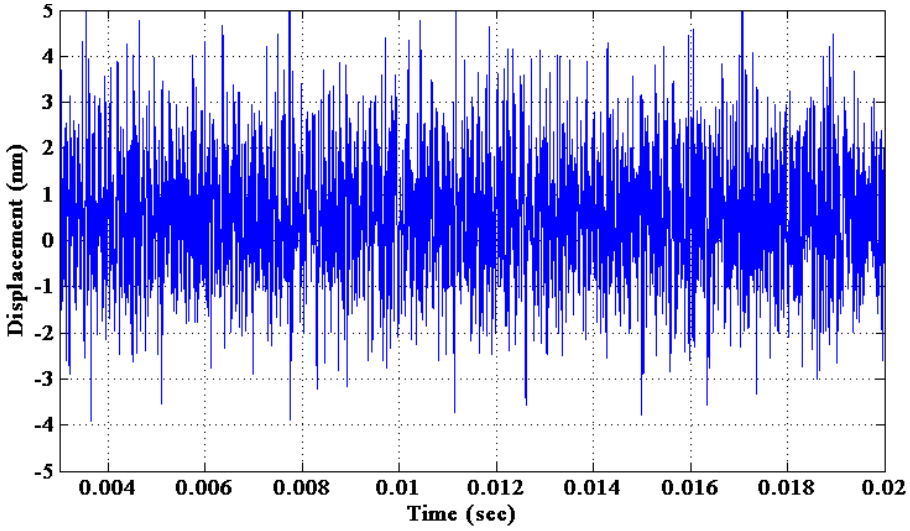

Figure 4-6: Displacement output of the accelerometer sensor for 10g input acceleration showing almost zero steady state error for $C_{int} = 10\,pF$.

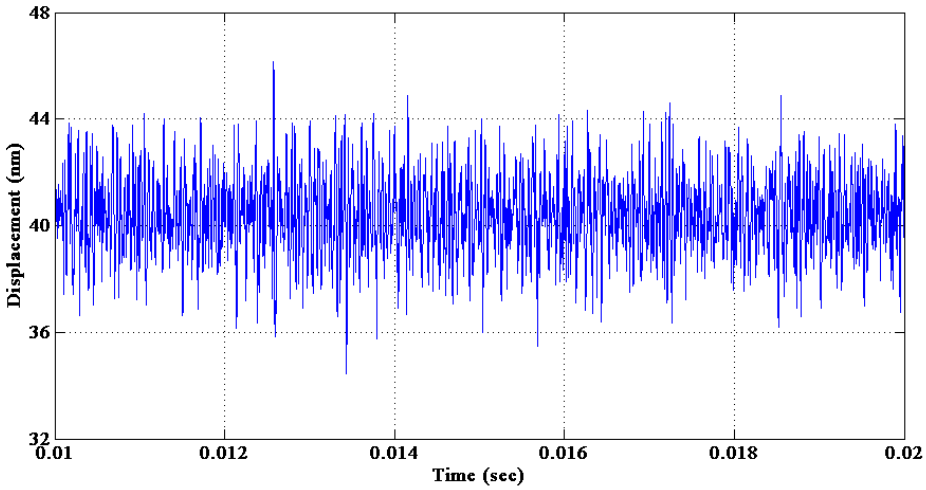

Figure 4-7: Displacement output of the accelerometer sensor for 10g input acceleration without I-controller for $C_{int} = 1\ pF$. Although accelerometer system is adjusted for maximum loop gain configuration, large amount of steady state error can be observed at the output of the accelerometer sensor.

Capacitances of the MEMS accelerometer sensor do not perfectly match with each other due to the fabrication process tolerances, resulting in a sensitivity difference for the positive and negative sensor electrodes. It is also expected to affect the linearity performance of the system. A MATLAB-Simulink simulation is conducted to illustrate the effect of capacitance mismatch on the accelerometer system with and without I-controller. Deliberately, $100\ fF$ capacitance mismatch is included in the simulation, also C_{int} is altered between 1 pF and 10 pF to combine the effect of low loop gain. Table 4-4 shows the overall linearity simulation results of the accelerometer system.

Clearly, capacitance mismatch severely degrades the linearity performance of the accelerometer in the absence of I-controller and its effect is further amplified with low loop gain configuration as illustrated in Table 4-4. On the other hand, I-controller achieves nearly perfect linear accelerometer system by keeping the proof mass stationary.

Table 4-4: Linearity simulation result of the accelerometer system with and without including I-controller. Also, the effect of a possible capacitance mismatch between the sensor electrodes is analyzed for different gain settings.

	P Controller				PI Controller			
C_{int} (pF)	1	10	1	10	1	10	1	10
Capacitive mismatch (fF)	0	0	100	100	0	0	100	100
Non-linearity (ppm) for (0g) - (10g)	182	2077	64	2180	<1			9
Non-linearity (ppm) for (0g) - (-10g)	180	2072	297	1971	<1			9
Non-linearity (ppm) for (-10g) - (10g)	119	1350	365	1604	<1			18
Offset (g)	0	0	0.14	0.15	0	0	-0.14	-0.14

4.5 Summary

In this chapter, accelerometer sensor parameters utilized in the 5th order accelerometer system are given and transfer function and important circuit parameter are calculated based on the equations given in Chapter 2. By considering stability of the 5th order system and closed loop response, circuit parameters are adjusted to achieve optimum settling time and low electronic noise. Also, noise contributions of each individual noise source are calculated and calculations are validated with the non-linear MATLAB-Simulink simulations.

The main focus of this chapter is to emphasize the importance of I-controller to achieve linear system. Thus, MATLAB-Simulink simulations are performed with the input acceleration ranging from -10g to 10g with 1g steps and linearity of the system is calculated based on linear fitting. Also, same simulation is conducted on the accelerometer system excluding I-controller to compare two systems. It is revealed that while linearity performance of the accelerometer system suffers from capacitance mismatch and low loop gain in the absence of I-controller, it is possible to achieve almost perfect linear system by including I-controller in the loop.

Next step is to validate the simulation results and present the improvements in linearity performance of the accelerometer system taking advantage of I-controller with the implemented readout circuit.

CHAPTER 5

TEST RESULTS AND DISCUSSIONS

This chapter presents the test results of the implemented readout circuit taking the advantage of PI controller and compares the results of accelerometer system with and without I-controller. Section 5.1 describes the data acquisition board which is used to acquire 1-bit digital output of the accelerometer package and transmit high resolution acceleration information by filtering 1-bit digital output of the accelerometer package. Section 5.2 gives the test result of the scale factor stability test which verifies the functionality of the readout circuit. Section 5.3 demonstrates the test results of the centrifugal acceleration test which proves enhancement in the linearity performance of the system taking advantage of I-controller. Section 5.4 gives the noise performance of the system and describes the way to find optimum feedback voltage achieving zero effective spring constant. Section 5.5 presents the bias repeatability performance of the accelerometer system. Section 5.6 gives the temperature dependent output characteristic of the accelerometer. Finally, Section 5.7 summarizes the chapter.

5.1 Data Acquisition Board

Data acquisition board includes commercial XEM 3010 FPGA board, regulator PCB and 16-pin metal accelerometer package in which the readout circuit and MEMS accelerometer sensor are integrated provides all the necessary connections between sub-blocks. Figure 5-1 shows the data acquisition board which is also responsible for transferring the high resolution acceleration data to PC.

Figure 5-2 shows the 16-pin metal accelerometer package including glass substrate, readout circuit and MEMS accelerometer sensor. Glass substrate, which is mounted

on the metal package, is used as a base for the component integration, and accelerometer sensor as well as the readout circuit are connected to the glass base via wire bonds, which are then connected to each other with the thin film metal lines laid over the glass base. Part of the readout circuit connections are carried towards the package pins with the help of metallization laid over the glass base.

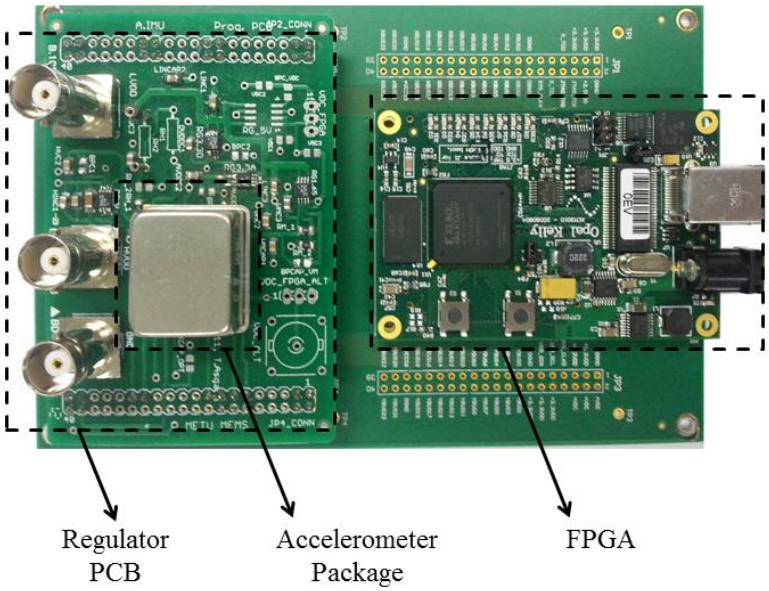

Figure 5-1: Accelerometer data acquisition board consists of regulator PCB, accelerometer package and FPGA.

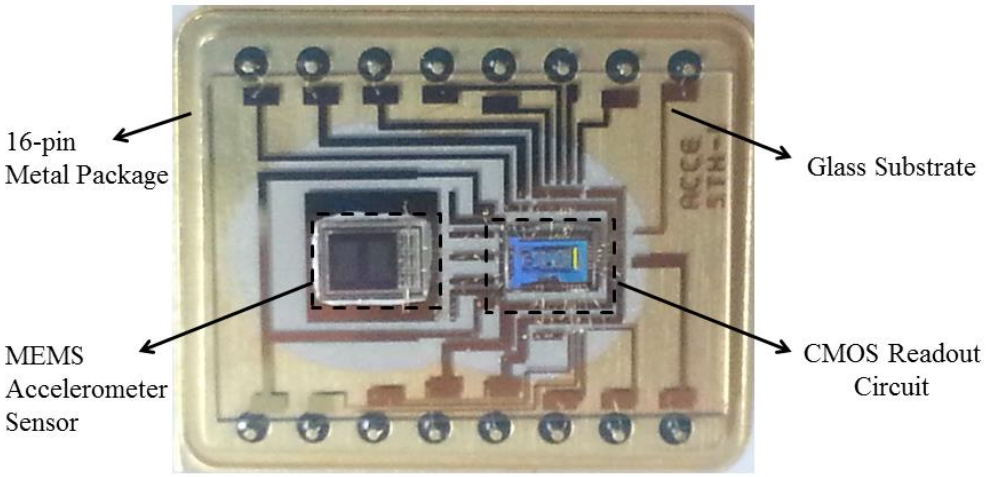

Figure 5-2: Accelerometer sensor integrated with the CMOS readout circuit in 16-pin metal accelerometer package.

Accelerometer package which is mounted on the regulator PCB needs several voltage inputs, clock and control signals to obtain proper operation. Thus, peripheral electronic block, FPGA and regulator PCB, are used to provide required signals and supply voltages to the accelerometer package.

Regulator PCB includes totally 4 regulators to supply essential low noise voltages to the accelerometer package. While two of the regulators generate 3.3V to provide digital and analog supply voltages to the readout circuit, remaining two voltage regulators supply 1.65V and feedback voltage V_{fb} which can be adjustable between 6V and 15V.

FPGA board is the main sub-block which controls and collects data from the accelerometer package. It provides high precision clock to the readout circuit with the help of PLL mounted on the commercial FPGA board. Additionally, it is also responsible for providing serial interface programming signals, since accelerometer readout circuit includes serial interface programming block that needs to be configured prior to start-up.

After configuring accelerometer readout circuit, FPGA sends the "start" command by pulling the reset pin to low and it begins collecting 1-bit low resolution output of the accelerometer package. In parallel with the acquisition of 1-bit digital data, decimation process of 1-bit signal take place in FPGA resulting in high resolution acceleration information. Then, FPGA transmits the high resolution data to the PC via a USB cable.

5.2 Scale Factor Stability Test

Prior to performance test of the implemented accelerometer readout circuit, scale factor stability test is conducted for the accelerometer system both utilizing P-controller and PI-controller to verify the functionality of the readout circuit. Readout circuit is configured for different loop gain configurations, and scale factor of the system is extracted for each configuration for the scale factor stability test. With this test, it is expected to obtain a constant scale factor for different loop gain configurations utilizing PI-controller. On the other hand, varying scale factor is expected for the accelerometer system with P-controller since the feedback amount

which is the output of the accelerometer system is directly related with the loop gain of the system.

Scale factor can be defined as the deviation in the digital accelerometer output for 1g change in the input acceleration. While it is possible to find the scale factor by subtracting the acceleration data collected at 0g and 1g condition, it is better to calculate scale factor by data acquired at -1g and 1g, since the accelerometer sensor is prone to alignment error in 0g condition. Thus, accelerometer system is positioned in 1g and -1g condition to acquire acceleration in each configuration and difference of the accelerometer output at 1g and -1g conditions divided by two in order to determine scale factor.

I-controller gain, feedback voltage sampling frequency and feedback capacitance are fixed to the $K_I = 25000, V_{fb} = 6\,V, t_s = 500kHz\ and\ C_{fb} = 0.4\,pF$ during the scale factor test. C_{int} and P-controller gain is altered to achieve different loop gain configurations. Table 5-1 presents the C_{int} values and P-controller gain configurations and resulting loop gain for 12 different test conditions. Expected loop gain is calculated at DC excluding the effect of the electrostatic spring and I-controller gain with the help of Equation 2.22.

Table 5-1: Test configurations for the scale factor stability test. Expected loop gain is calculated at DC excluding effect of the electrostatic spring and I-controller gain.

Test ID	#1	#2	#3	#4	#5	#6	#7	#8	#9	#10	#11	#12
C_{INT}	15	12	15	12	9	6	3	1	1	1	1	1
P-gain	2/3	2/3	1	1	1	1	1	1	2	3	4	5
Expected Loop Gain	0.2	0.3	0.4	0.5	0.6	0.9	1.8	5.4	10.7	16.1	21.5	26.9

Figure 5-3 shows the test results of the scale factor stability test for Package#1 in which accelerometer sensor and readout circuit is integrated with both P-controller and PI controller. It is obvious that, scale factor of the system including only P-controller is severely affected by the variations in the system loop gain. For the minimum loop gain configuration, scale factor of the accelerometer including

P-controller can be approximately found to be half of the scale factor obtained with I-controller. It means that the accelerometer system cannot counterbalance the input acceleration completely and it can only generate a force corresponding to 0.5g for 1g input acceleration. The remaining unbalanced 0.5g acceleration causes proof mass to move in the input direction. On the other hand, the accelerometer system including the PI controller keeps the proof mass stationary regardless of loop gain guarantying a constant scale factor.

Main purpose of the scale factor test is to verify the functionality of the readout circuit and effect of I-controller by comparing accelerometer system utilizing P-controller and PI-controller. With the test results given in Figure 5-3, the functionality of the readout circuit is verified. Also, it is observed that I-controller keeps the proof mass stationary as desired assuring a high linearity.

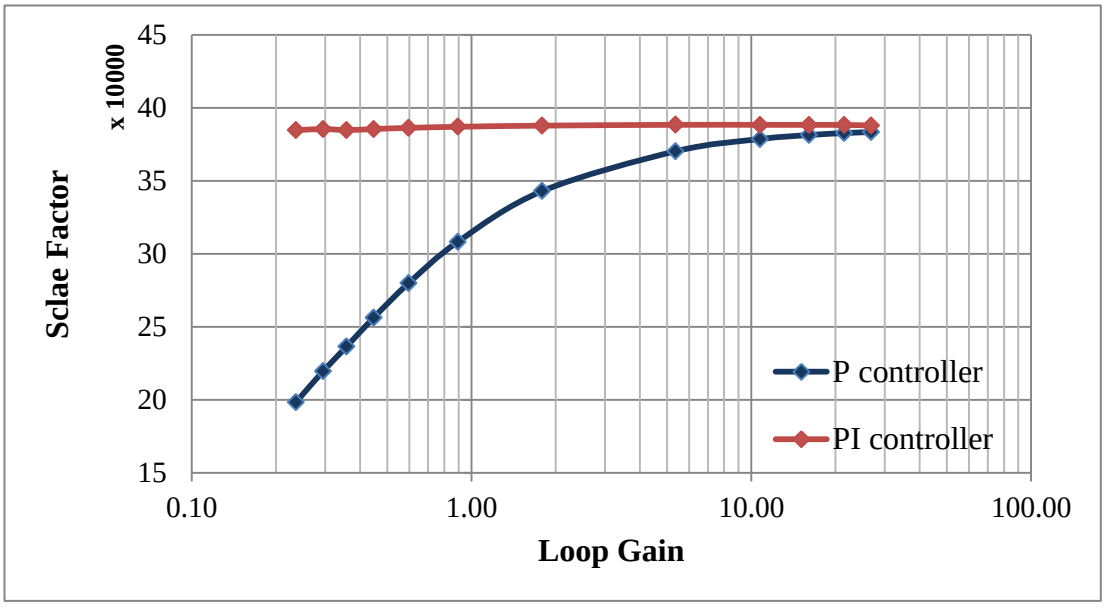

Figure 5-3: Scale factor of the accelerometer system (Package#1) utilizing both P-controller and PI-controller for 12 different loop gain configurations. PI-controller manages to keep scale factor constant regardless of loop gain verifying effect of I-controller.

5.3 Linearity Test

After verifying the functionality of readout circuit and I-controller with the scale factor stability test, a linearity test is conducted on the accelerometer package to find the linearity performance of the accelerometer system including P-controller and PI-controller.

Figure 5-4 shows the linearity measurement test setup that includes data acquisition board, data acquisition PC, power supply and rate table. Rate table connection cables are employed in the test setup to supply power to the data acquisition board via slip rings. Normally, high resolution acceleration data is transmitted from FPGA to the PC via USB cable. However, USB cable operates at high frequency, and it is not possible to transfer acceleration data via slip rings of the rate table while applying a centrifugal acceleration to the sensor. To solve this problem, a Verilog code is prepared to store the high resolution acceleration data in the SDRAM which is one of the peripheral utilized on the commercial FPGA board during the linearity test. Then, at the end of the linearity test, the stored acceleration information is transmitted to the PC via a USB cable.

Rate table is employed in the setup to apply centrifugal acceleration to the accelerometer package. The centrifugal acceleration can be found by the a formula

$$a = w^2 r \tag{5.1}$$

where, a, w and r are the centrifugal acceleration, angular velocity, and the distance between accelerometer sensor to center of the rate table, respectively. By setting the angular velocity of the rate table it is possible to apply varying centrifugal acceleration to the accelerometer package. Thus, data acquisition board is placed at an off-centered position over the rate table, and a centrifugal acceleration from 0g to 3g is obtained by sweeping angular rate to find linearity performance of the system. Since the centrifugal acceleration appears as outward acceleration in the rotating rate table, the data acquisition board is fixed to the rate table in reverse orientation to acquire data with acceleration input changing between 0g to-3g.

I-controller gain, proportional gain, feedback voltage, sampling frequency and feedback capacitance are fixed to $K_I = 25000, K_P = 2/3, V_{fb} = 6\,V$

$t_s = 500kHz\ and\ C_{fb} = 0.4\ pF$ during the linearity measurement test of Package#1. C_{int} is altered to achieve different loop gain configurations for accelerometer system including P-controller and PI controller.

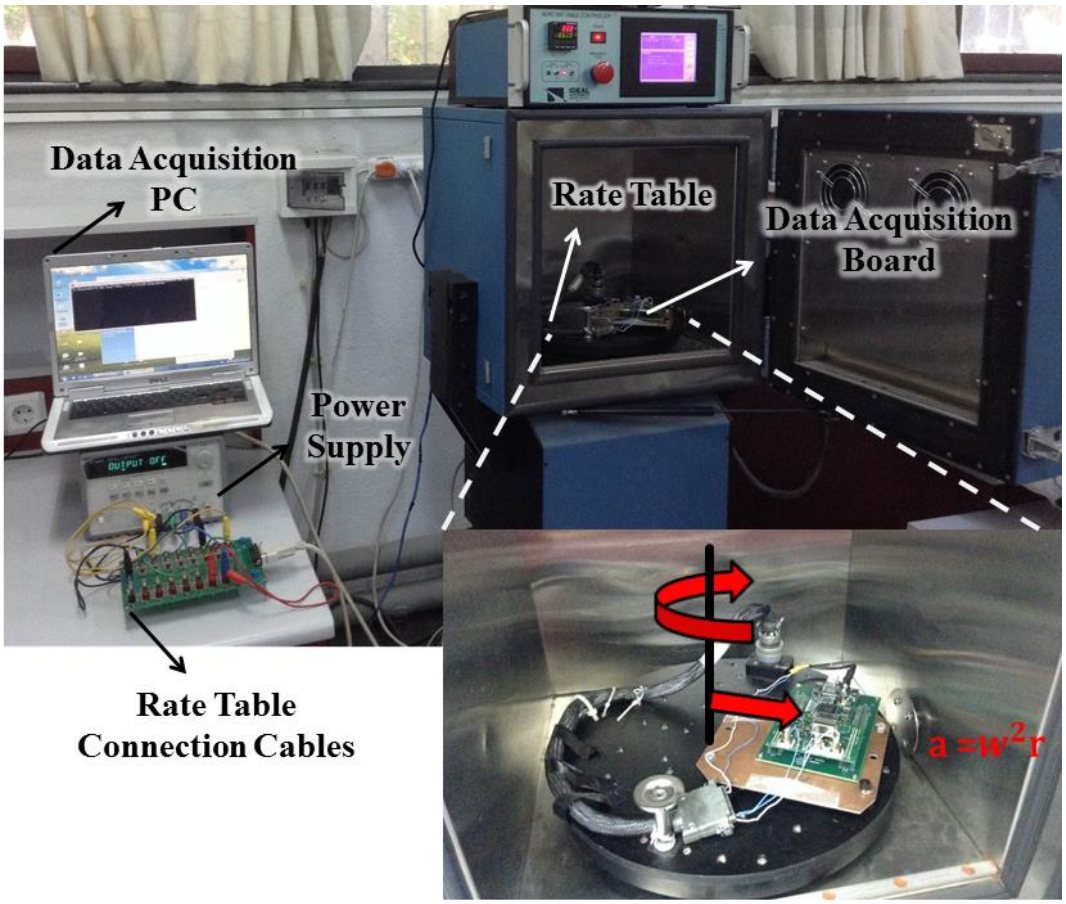

Figure 5-4: Test setup for the linearity performance measurement of the accelerometer system utilizing P-controller and PI-controller. Centrifugal acceleration is applied to the accelerometer package using rate table.

In order to avoid turn on behavior of the accelerometer which is the rapid drift of an accelerometer output observed for some time following to the startup of an operation due to the environmental factor such as temperature, centrifugal acceleration is applied on to the accelerometer 5 minutes after power on. The acceleration data is collected at 18 different angular rates corresponding to a centrifugal acceleration range from 0g to 3g, and then from 0g to -3g by reversing the accelerometer mounting direction . Then, the accelerometer output is processed by averaging the

acceleration data at each angular rate. Finally, in order to find non-linearity of the accelerometer system, linear fitting is performed with least square fitting method and residuals which are the difference between accelerometer outputs and fitted values provided by a model are calculated. Non-linearity of the system is recorded by dividing the residual having maximum value to the input range.

Figure 5-5 presents the measured data of the system for both P-controller and PI-controller with varying input acceleration and $C_{int} = 5pF$ configuration. Also, fitted lines can be observed in the figure for each measurement. Slope of the fitted lines corresponds to the scale factor of the accelerometer system for specific configuration. As revealed in the scale factor stability test, scale factor of the system decreases due to the limited loop gain of the system with P-controller. Figure 5-5 showing two different fitted lines verifies that scale factor of the system reduces resulting in a higher displacement in the proof mass which causes poor linearity performance for the accelerometer system without I-controller.

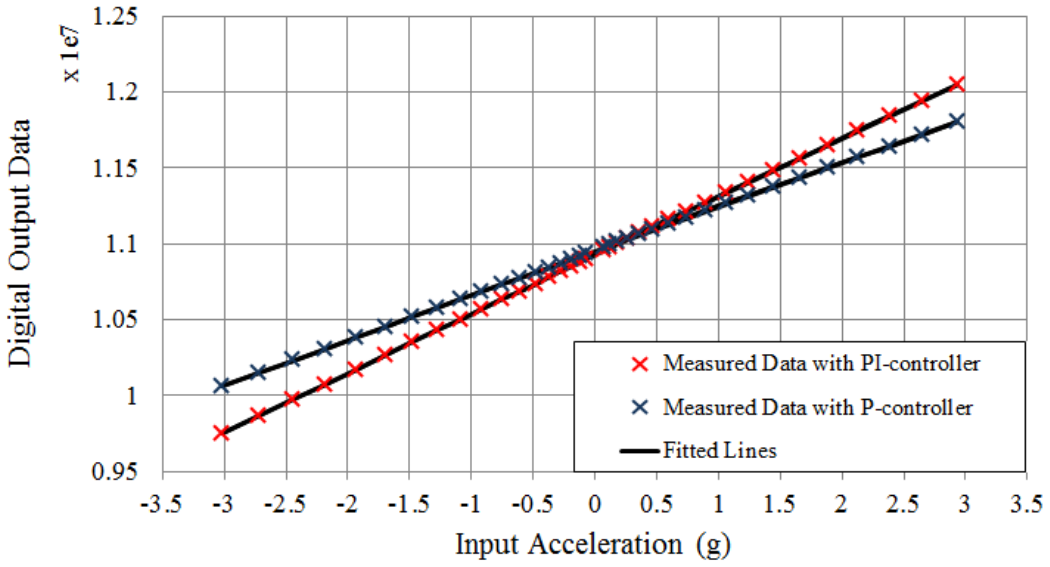

Figure 5-5: Response of the accelerometer system with both P-controller and PI-controller for varying input centrifugal acceleration and $C_{int} = 5\ pF$. For the data collected with P-controller, slope of the fitted line which corresponds to scale factor is less than slope of the data collected with PI controller due to the limited loop gain of the accelerometer system utilizing P-controller.

Figure 5-6 and Figure 5-7 present the residuals of the accelerometer system with PI-controller for positive and negative input accelerations. Residuals are also plotted for 3 different integration capacitance values $C_{int} = 1pF, 5pF \; and \; 9pF$ in order to observe effect of the different loop gain configurations. Also, Figure 5-8 and Figure 5-9 shows the residuals of the accelerometer system with P-controller for positive and negative input accelerations. Similarly, linearity test is conducted for 3 different integration capacitance values.

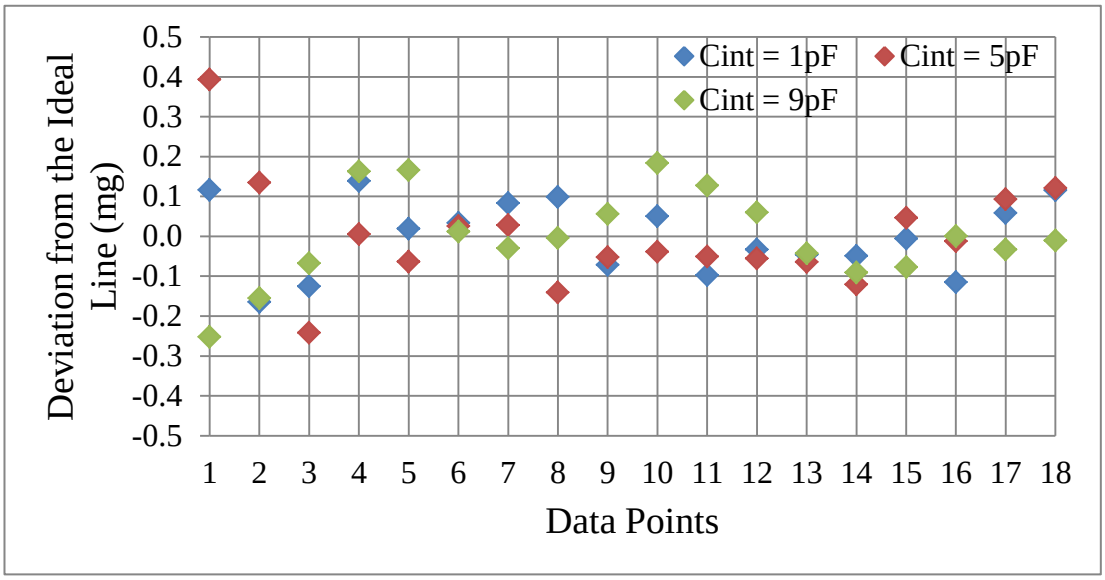

Figure 5-6: Residuals for the accelerometer system including PI controller with input acceleration varying from 0g to 3g. The linearity test is conducted for 3 different integration capacitance values to observe non-linear off the system with varying loop gain and maximum deviation is registered as 0.39 mg.

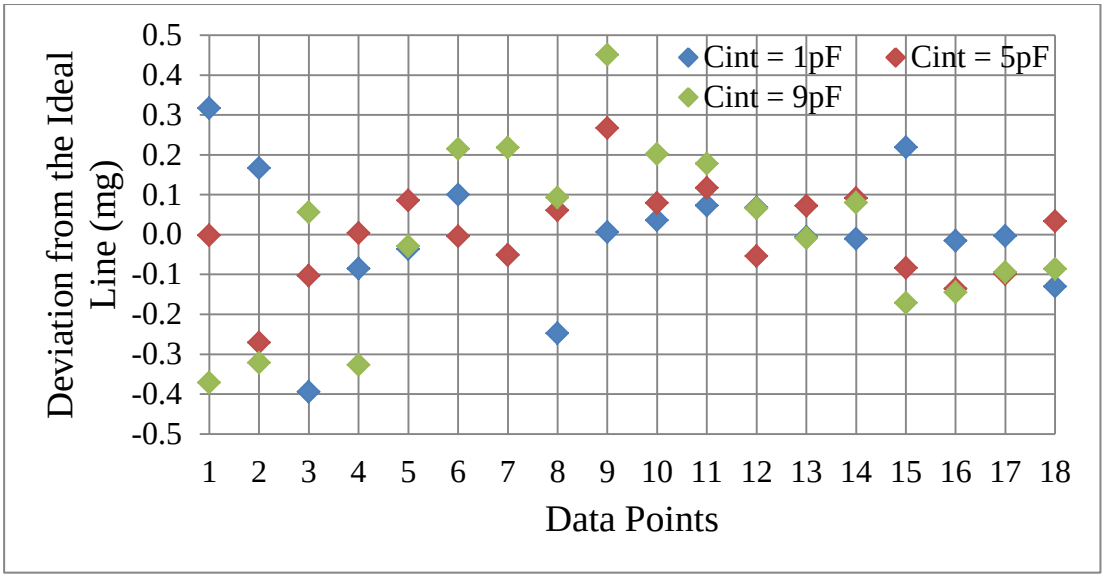

Figure 5-7: Residuals for the accelerometer system including PI controller with input acceleration varying from 0g to -3g. Maximum deviation is registered as 0.45 mg.

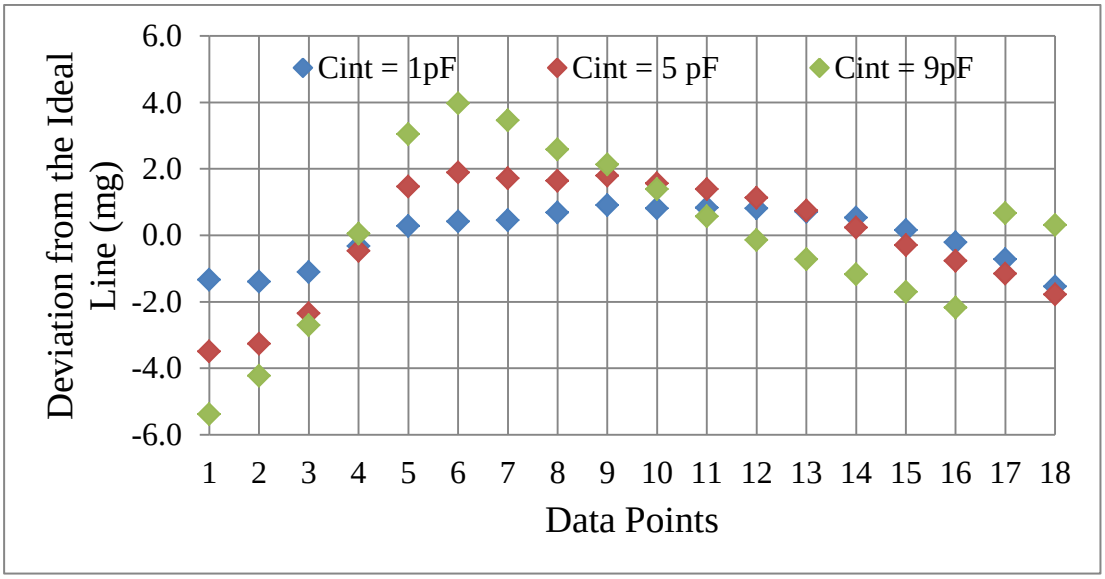

Figure 5-8: Residuals for the accelerometer system including P controller with input acceleration varying from 0g to 3g. Maximum deviation is registered as 5.38 mg for $C_{int} = 9pF$ configuration.

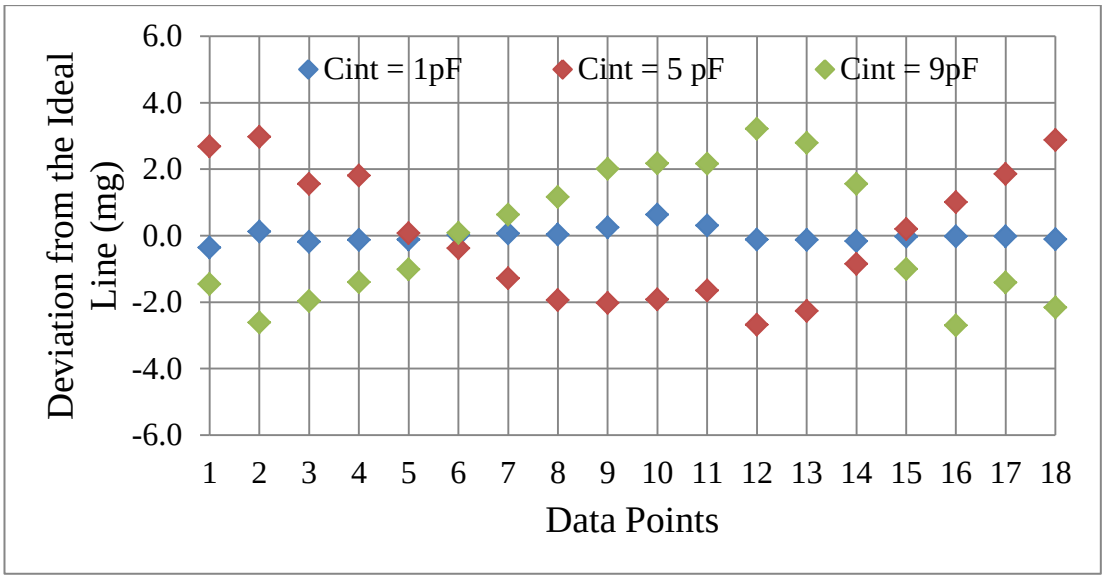

Figure 5-9: Residuals for the accelerometer system including P controller with input acceleration varying from 0g to -3g. Maximum deviation is registered as 3.22 mg for $C_{int} = 9pF$ configuration.

It can be seen that while the residuals are varying between -0.5 mg to 0.5 mg with the PI-controller, the maximum deviation from the ideal line increases up to 5.38 mg for the system including only P-controller. Apparently, additional I-control action boosts the loop gain of the system and increases the linearity.

The non-linearity of the system monotonically increases as the loop gain of the system decreases. This observation verifies that while the accelerometer sensor is the main non-linearity source, loop gain is the major concern for the linearity performance of the accelerometer system without I-controller. On the other hand, residuals observed in Figure 5-6 and Figure 5-7 for the system including PI controller are scattered around zero randomly. So, it can be concluded that, the non-linearity of the accelerometer sensor is reduced by I-controller action.

Remaining residuals scattered around zero for the accelerometer system including PI controller may be related with the time and temperature dependent drift of the accelerometer sensor, external vibrations or the non-linearity of the rate table. Also, misalignment of the accelerometer package with respect to center of the rate table may affect the linearity performance of the system randomly due to the cross-axis sensitivity of the accelerometer sensor. Additionally, the simulations show that the

non-linearity of the system depends on the output offset and for the tested package the output offset is found to be 0.60g which may be the main source of non-linearity for the accelerometer including PI controller.

These non-idealities may have contributed to the non-linearity of the system including PI controller. Although, the perfect linear system is not achieved with PI controller, test results show that non-linearity of the accelerometer system is reduced by keeping the proof mass at a stationary position, resulting in significant amount of improvement up to 20 times in the linearity performance.

The centrifugal acceleration is limited with the maximum acceleration of 3g due to the limited angular velocity that can be supplied by the rate table as well as the limited table diameter. With increased input range, it is expected to obtain same amount of residual values for the system with PI-controller resulting in better linearity performance. On the contrary, non-linearity performance of the system with P-controller is expected to get worse, since the residual increases approximately proportional to square of input acceleration as depicted in Figure 2-7.

The purpose of the linearity performance test is to obtain linearity of the accelerometer taking the advantage of the PI controller and show a significant amount of improvement in the linearity performance by comparing the test result of the accelerometer with and without I-controller action. To establish a fair comparison, Table 5-2 gives the non-linearity results of the system in ppm with and without the I-controller for different integration capacitance values.

Table 5-2: Linearity performance of the accelerometer system for both P-controller and PI controller with varying loop gain configuration.

Package#1	P-controller Nonlinearity (ppm)		PI-controller Nonlinearity (ppm)	
C_{int}	Positive g	Negative g	Positive g	Negative g
1 pF	523	207	58	129
5 pF	1190	983	137	89
9 pF	1827	1065	88	144

Apparent improvement in the linearity performance can be seen for the system taking advantage of the I-controller. Particularly, for the low loop gain configuration, enhancement up to 20 times is achieved in the linearity. Also, 10 times improvement is observed in the positive direction while 1.5 times enhancement is achieved in negative direction with maximum loop gain configuration. It is important to point out that there is a difference in the enhancement of the linearity performance for positive and negative direction. The effect of output offset on the linearity performance for two directions is illustrated with the simulation results in the Table 4-4. So, the 0.60g output offset of Package #1 may have cause the difference in the enhancement of linearity performance for two directions given in Table 5-2.

The improvement in the linearity performance of the accelerometer utilizing PI-controller is presented with the performance test conducted on a single accelerometer package (Package #1). However, it is important to verify repeatability of linearity enhancement with different accelerometer packages in which readout circuit is integrated with the MEMS accelerometer sensor. Hence, the linearity performance test is also conducted on a second accelerometer package (Package #2), which is prepared identical to the first sensor package, and subjected to the same test procedures. The linearity performance of this second accelerometer package (Package #2) is summarized in Table 5-3.

Table 5-3: Linearity performance of the Package #2 for both P-controller and PI controller with varying loop gain configuration.

Package#2	P-controller Nonlinearity (ppm)		PI-controller Nonlinearity (ppm)	
C_{int}	Positive g	Negative g	Positive g	Negative g
1 pF	150	152	38	36
5 pF	445	179	43	35
9 pF	783	531	40	88

While the improvement in the linearity performance is 4 times for maximum gain configuration, this enhancement increases up to 20 times with low loop gain configuration for Package #2 similar to the linearity test result of the Package #1.

With the linearity measurement of the Package #1 and Package #2, it is verified that, the repeatable linearity performance improvement can be observed for the accelerometer system almost achieving a perfect linear system taking advantage of a PI-controller.

5.4 Noise and Bias Drift Measurement

IEEE Standard 1293 [52], states that noise floor of the accelerometer system should be determined by power spectral density (PSD) and Allan Variance graph of the acceleration data collected at zero-g condition. So, data acquisition board is fixed to the stationary optical table at zero-g condition and also placed into the Faraday cage in order to prevent the effect of undesired electromagnetic noise sources. Figure 5-10 shows the accelerometer noise measurement test setup that is fixed to optical table. High resolution processed acceleration data are collected to determine the noise floor of the accelerometer system according to the IEEE Standard.

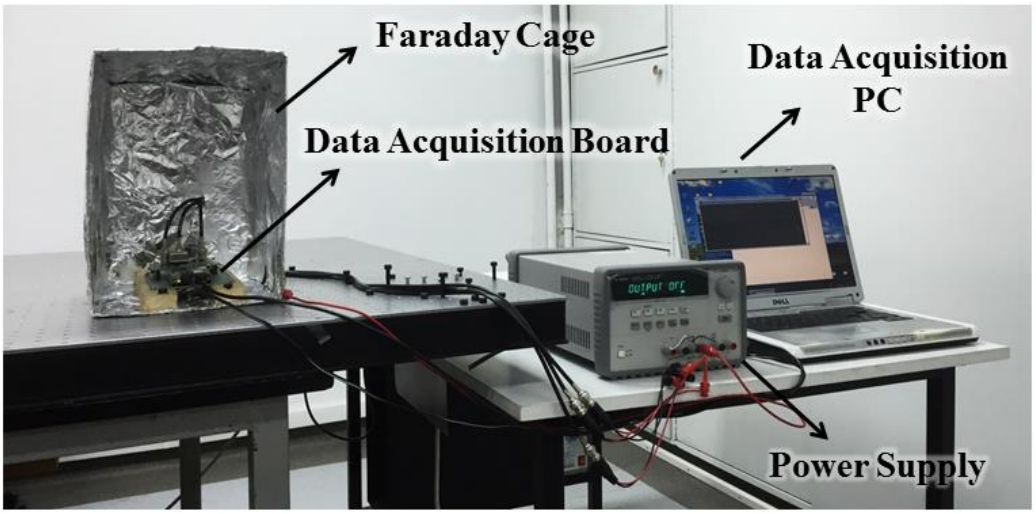

Figure 5-10: Data acquisition board is placed into the Faraday cage in noise measurement test setup to avoid electromagnetic interference.

I-controller gain, proportional gain, feedback voltage, sampling frequency and feedback capacitance are fixed to $K_I = 25000, K_P = 2/3, V_{fb} = 6\,V$ $t_s = 500kHz\ and\ C_{fb} = 0.4\,pF$ during the noise measurement of the Package #1.

Digital output of the accelerometer is collected for approximately 15 minutes. The digital output of the accelerometer is converted to the actual acceleration by using scale factor to determine white noise floor.

Figure 5-11 presents the acceleration equivalent noise PSD of the Package #1 utilizing PI-controller under zero-g condition. Noise floor of the accelerometer package can be found to be -98.3 dB corresponding to 12.16 $\mu g/\sqrt{Hz}$.

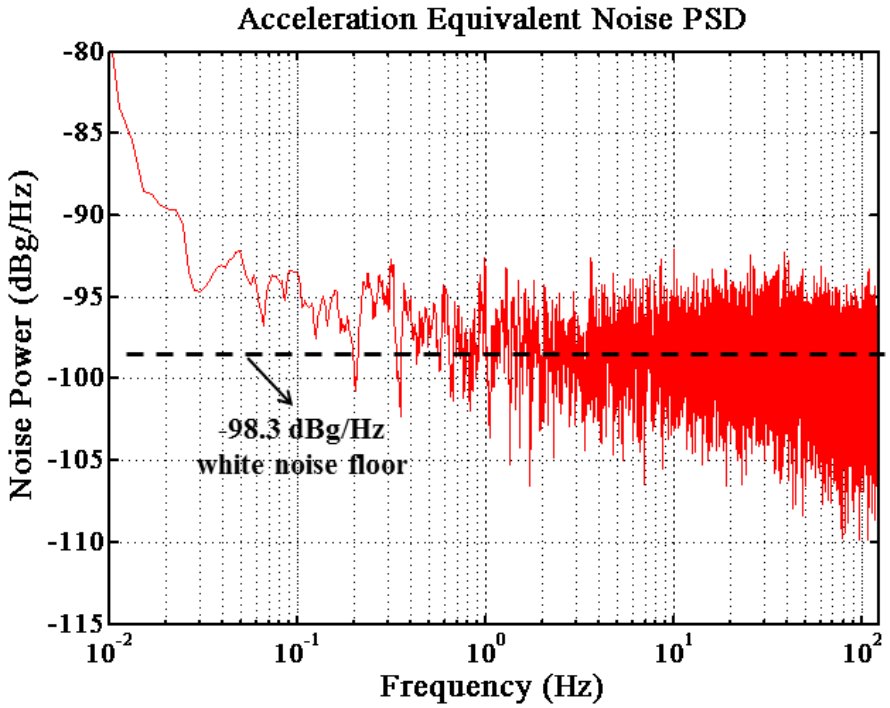

Figure 5-11: Power spectral density of the Package #1 with PI-controller showing approximately -98.3 dB which corresponds to 12.16 $\mu g/\sqrt{Hz}$ white noise floor.

The white noise floor estimation can also be performed by analyzing the peak to peak noise of the acquired sensor data. By assuming flicker noise is not dominant at the baseband frequency and acquired data has white noise with Gaussian distribution, white noise floor of the output can be determined by the Equation 5.2.

$$a_n = \frac{1}{6.6}\frac{a_{PP}}{\sqrt{f_B}} \qquad 5.2$$

where a_{PP} and f_B are the peak to peak noise and signal bandwidth respectively.

Figure 5-12 presents the transient acceleration output of the Package #1 normalized around zero. Sampling frequency of the 1-bit digital data is adjusted to be 500 kHz, however after decimation process of the FPGA signal bandwidth reduces down to 122 Hz. Also, peak to peak acceleration can be found to be 0.94 mg from the transient acceleration output. Finally, white noise floor can be extracted using Equation 5.2 as 12.89 $\mu g/\sqrt{Hz}$ which is close to the result obtained with PSD.

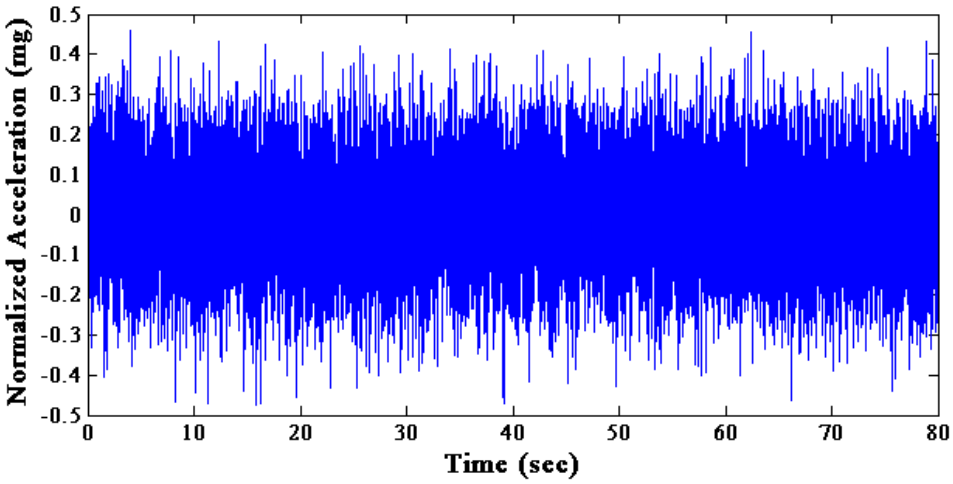

Figure 5-12: Acceleration output of the Package #1 including PI controller under zero-g condition. Offset of the output is subtracted from acquired data to normalize acceleration output around zero.

In order to determine bias stability and white noise floor of the accelerometer Allan Variance analysis should be performed on the accelerometer output. Figure 5-13 presents a typical Allan Variance graph given in [53] for an accelerometer. In Allan Variance graph, white noise appears on the line with the slope of -0.5. The reading of the line with the slope of -0.5 at $\tau = 1$ gives the velocity random walk (VRW) for the accelerometer system. And it defines the double sideband white noise floor of the accelerometer. Since previous analyses use single sideband power spectral density, it should be multiplied by $\sqrt{2}$ to find one sideband white noise floor. Also, bias drift of the accelerometer can be found using Allan Variance graph where the slope is zero.

Figure 5-14 shows the Allan Variance plot of the output acceleration data of Package #1 acquired under zero-g condition with and without including I-controller. The velocity random walk and bias instability can be found to be 9.04 $\mu g/\sqrt{Hz}$ and 5.8 μg respectively for the accelerometer system including PI-controller. Single side band white noise floor can be also extracted as 12.78 $\mu g/\sqrt{Hz}$ by multiplying the velocity random walk with $\sqrt{2}$. Thus, the approximate white noise floor of 12.5 $\mu g/\sqrt{Hz}$ is verified by using three different methods applied on the data acquired from accelerometer utilizing PI-controller.

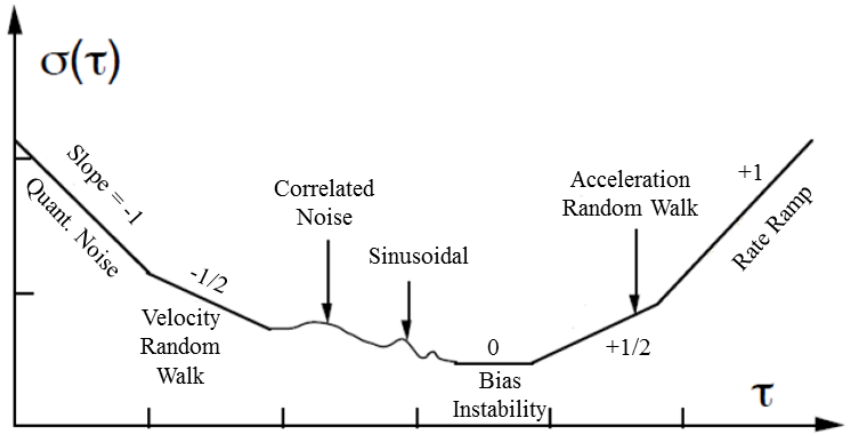

Figure 5-13: A typical Allan Variance plot showing various slopes for different error sources [53].

In order to compare the noise performance of the accelerometer with and without I-controller, the Allan Variance graph of the data collected from accelerometer utilizing P-controller is also given in Figure 5-14. Accelerometer system utilizing P-controller achieves 8.97 $\mu g/\sqrt{Hz}$ and 7.2 μg velocity random walk and bias instability which are very close to the results obtained with the accelerometer employing PI-controller. With this comparison, it is verified that additional I-controller block does not affect the noise performance of the system while providing high linearity performance.

As a summary designed 5th order accelerometer system including PI-controller achieves approximately 12.5 $\mu g/\sqrt{Hz}$ white noise floor which is limited by the Brownian noise (expected to be around 11.4 $\mu g/\sqrt{Hz}$) of the accelerometer sensor and 5.8 μg bias instability performance in the $\pm 28.8\, g$ input acceleration range corresponding to 127 dB dynamic range for this configuration and without further system parameter optimization. Also, it is important to emphasize that additional I-controller block does not elevate the white noise floor of the system as expected.

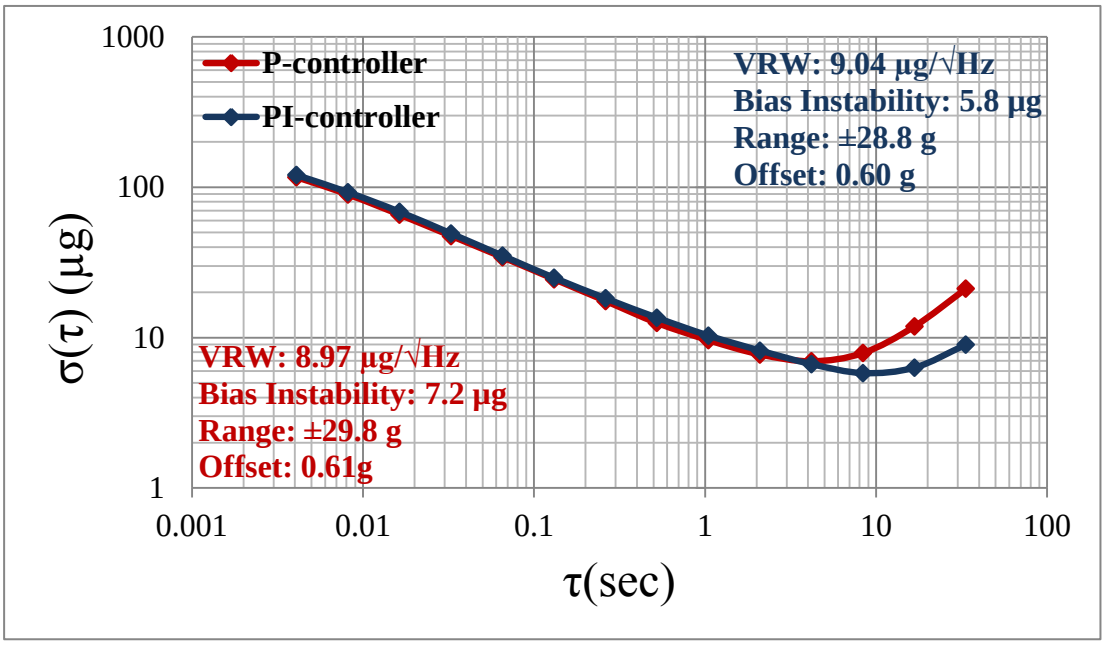

Figure 5-14: Allan Variance plot for the output of the Package#1 with and without including I-controller. The plot proves that additional I-controller block does not affect the system noise performance.

The noise measurement results show that electronic noise and feedback voltage noise has small amount of contribution on the overall white noise floor of the accelerometer system. However, while the feedback voltage noise is inevitable due to the direct voltage to force conversion, it is possible to suppress additional electronic noise by adjusting the effective spring constant of the accelerometer by manipulating feedback voltage. Next section illustrates the experimental method to suppress electronic noise by adjusting feedback voltage amplitude.

5.4.1. Feedback Voltage Optimization

Although the electronic noise is not the dominant noise source in the test results presented in the section 5.4, it is important to verify the experimental method showing the suppression of the electronic noise with the help of electrostatic spring softening effect. To illustrate and verify this experimental method, firstly the electronic noise should be increased intentionally until it dominates the overall noise floor. Then, it needs to be suppressed via feedback voltage optimization by utilizing softening effect.

Front-end amplifier employed in the readout circuit takes advantage of correlated double sampling which is the method used for flicker noise suppression. This flicker noise suppression feature of front-end amplifier can be disabled/enabled by user via serial programming interface. While correlated double sampling method is normally enabled to suppress the electronic noise especially for low frequencies, deactivation of this feature results in elevated flicker noise floor. Since the deactivated correlated double sampling feature gives rise to the electronic noise at low frequencies, the experimental feedback voltage optimization can be verified by suppressing additional flicker noise while operating the readout chip without correlated double sampling.

The main purpose of the experimental method utilizing spring softening effect is to adjust the effective spring term $k - k_e$ to approximately 0 N/m. Equation 2.33 states that the closed loop output of the accelerometer system can be calculated by using gain coefficients and effective spring term $k - k_e$. Since the gain coefficients which are adjusted by user are already known, and steady state closed loop response of the accelerometer for 1g step input can be obtained by subtracting the acceleration data acquired under 0g and 1g, effective spring constant $k - k_e$ can be calculated using Equation 2.33. Note that subtraction of the acceleration data under 0g and 1g gives scale factor of that accelerometer. After finding effective spring constant for specific feedback voltage, k_e can be manipulated by altering feedback voltage to reduce effective spring constant according to the Equation 2.18.

In order to find effective spring constant of Package #1 with $V_{fb} = 6V$, scale factor stability test result presented in Figure 5-3 is used. Remember that, Figure 5-3 gives the scale factors of the accelerometer system for different gain configurations, and

this measurement results can be used in the calculation of the effective spring constant. Although the scale factor measured for specific gain configuration is enough for the calculation, utilization of scale factors for different gain configurations increases the calculation accuracy.

To utilize the scale factors for different gain configurations in the effective spring constant calculation at once, fitting which insures minimum error power is applied to the scale factor test results presented in Figure 5-3 with the help of Equation 2.33. As a result of this fitting effective spring term is found to be $k - k_{e,6V} = 6\ N/m$ for $V_{fb} = 6V$.

Since mechanical spring constant k and electrostatic spring constant $k_{e,6V}$ for $V_{fb} = 6V$ are both unknown. Scale factor stability test and the fitting with minimum error power are repeated for $V_{fb} = 6.15V$. Figure 5-15 presents the scale factor stability test results for the accelerometer system utilizing P-controller and PI-controller. Also line which is fitted to the scale factor stability results of accelerometer utilizing P-controller is provided in Figure 5-15. The Equation 2.33 is used for fitting, and effective spring constant is found to be $k - k_{e,6.15V} = 4.9\ N/m$ for $V_{fb} = 6.15V$.

The electrostatic spring constant is proportional to V_{fb}^2, and it can be expressed as

$$k_{e,V_{fb}} = \alpha V_{fb}^2 \qquad 5.3$$

Hence, two equations $k - k_{e,6V} = 6\ N/m$ and $k - k_{e,6.15V} = 4.9\ N/m$ for two different feedback voltage levels can be combined using Equation 5.3 to extract all unknown terms. With this approach, mechanical spring constant is found to be $k = 27.72\ N/m$. In addition, optimum feedback voltage which is zeroing effective spring term is calculated as $V_{fb,opt} = 6.78V$.

In order to present the suppression of the electronic flicker noise with the optimum feedback voltage and compare the noise spectrum of the accelerometer for two different feedback voltage levels, acceleration data is collected using noise measurement test setup and acquired acceleration data is analyzed with the Allan Variance method. Accelerometer is configured to $C_{int} = 1pF,\ K_P = 2/3,$

$t_s = 500kHz$ and $C_{fb} = 4pF$ and feedback voltage is set to 6V and 6.78V respectively for the noise measurement. Also, it is important to remind that, correlated double sampling feature of the front-end amplifier is intentionally disabled to increase flicker noise level.

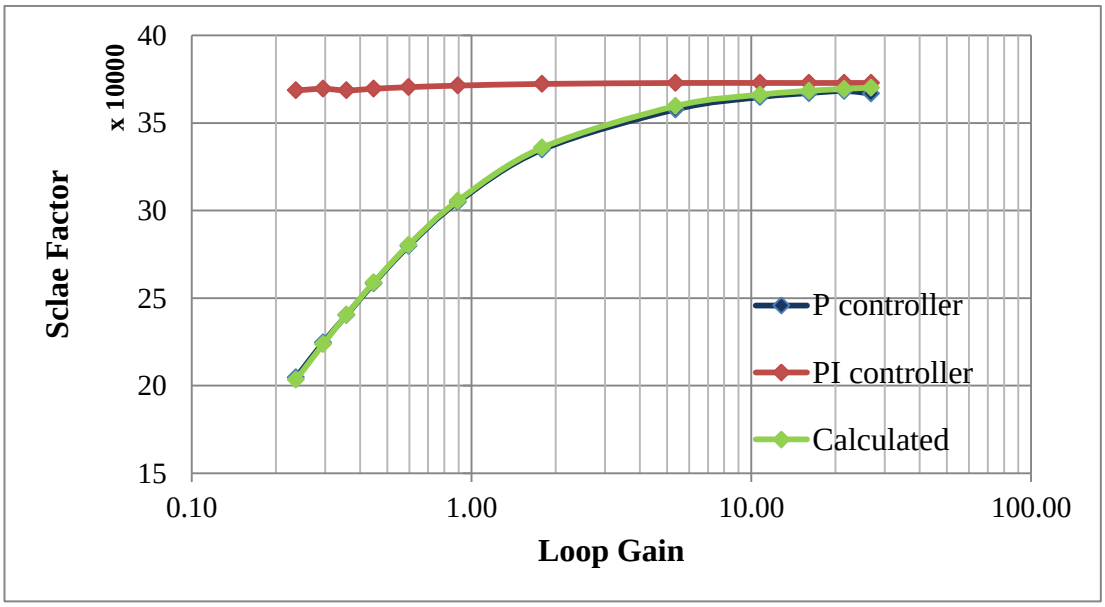

Figure 5-15: Scale factor of the accelerometer system (Package#1) utilizing both P-controller and PI-controller for 12 different loop gain configurations. Fitting is applied to the scale factor test results of accelerometer system utilizing P-controller according to the Equation 2.33, and effective spring constant is found to be 4.9 N/m.

Figure 5-16 shows the Allan Variance plot of the Package #1 for $V_{fb} = 6V$ and $V_{fb} = 6.78V$ which is the optimum feedback voltage zeroing effective spring term. While the bias instability point is found to be 18 µg with $V_{fb} = 6V$, it reduces down to 6.9 µg verifying realization of flicker noise suppression at low frequency with the help of spring softening effect. On the other hand, although the output range of the accelerometer is increased up to $\pm 37.1\ g$ by adjusting $V_{fb} = 6.78V$, white noise floor of the accelerometer system remains same compared to the $V_{fb} = 6V$ configuration since mechanical Brownian noise is still the dominant white noise source for both cases.

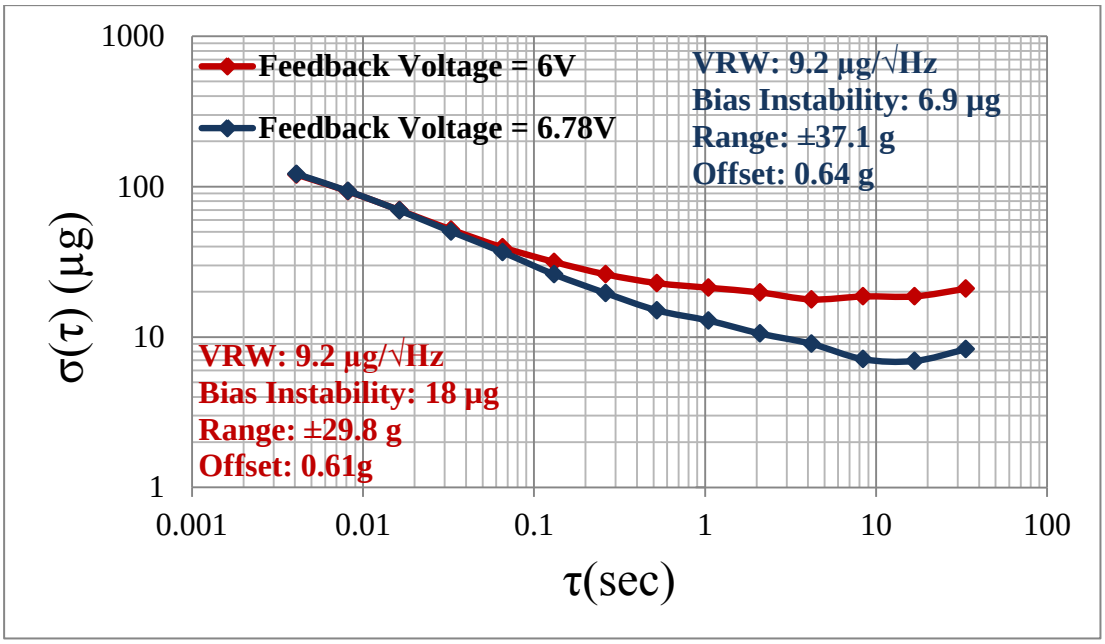

Figure 5-16: Allan Variance plot of the Package #1 showing electronic flicker noise suppression by adjusting feedback voltage. Note that, correlated double sampling feature which eliminates flicker noise is disabled intentionally to illustrate effect of feedback voltage on the noise suppression.

As a summary, if an accelerometer sensor with high spring constant is utilized in the accelerometer system, then the resulting output-referred electronic noise becomes dominant. Also, the effect of the electronic noise is likely to get dominant with the increasing stationary accelerometer sensor capacitance and parasitic capacitance at the sensor to readout interface. In order to overcome these problems, it is demonstrated with the noise performance test that it is possible to suppress the effect of electronic noise substantially by adjusting the feedback voltage with the help of electrostatic spring softening effect.

5.5 Bias Repeatability Measurement

Bias repeatability is the one of the most important performance criterion for the high-performance accelerometer systems, and according to the IEEE Standard, bias repeatability measurement should be conducted to determine the repeatability of the accelerometer bias across cool-down and shut-down.

Test procedure includes repetitive up-down, four-point or multipoint test to determine the scale factor and bias of the accelerometer system. At the end of each test, the system should be de-energized and waited for a constant period of time to cool down. At the end of repetitive bias measurements, rms deviation of the bias from the mean value should be calculated in order to find bias repeatability of the accelerometer system.

Up-down, four-point or multipoint tests are used for accurate bias repeatability measurement. By increasing the number of measurement points, the accelerometer model coefficients can be included in the calculation of bias repeatability performance to enhance the accuracy of bias repeatability measurement. However, these test procedures require high precision dividing head for the bias repeatability measurement. Thus, repetitive bias measurement is conducted by using alternative method suggested by IEEE Standard for the implemented accelerometer system. In this method, accelerometer system is kept at fixed position across cool-downs and shut-downs. Similar to the first method rms deviation of the bias is calculated to determine the bias repeatability performance.

Faraday cage is utilized for isolating the accelerometer test setup from electromagnetic noise sources during the bias measurement. Accelerometer bias data is acquired for 15 minutes and system is de-energized to let the accelerometer system cool-down for 20 minutes. This bias measurement is repeated for 5 times, and average of the acceleration data is calculated for the last 5 minutes of the collected data in order to avoid turn on behavior of the accelerometer system. Then, bias deviation of the system is calculated based on the mean bias value of the first test and rms deviation is calculated using the extracted bias deviations.

Since, accelerometer system should be turned on and off 5 times in approximately 3 hours for the bias repeatability measurement of single system configuration, test procedure is automated. Accelerometer data acquisition board is already connected to the PC via USB cable in order to transfer high resolution acceleration information. In order to automate the data acquisition, power supply is also connected to the PC via GPIB cable, and C++ code is written to send turn on/off command to power supply and start/stop command to the accelerometer system by considering start up

sequence. With the written program bias repeatability tests are conducted easily without requiring extra labor.

Bias repeatability test is conducted for the Package #2 with different feedback voltage levels and both with and without I-controller in order to observe effect of the I-controller on the bias repeatability performance of the system. Accelerometer system is configured as for $C_{int} = 1\,pF, C_{fb} = 0.8\,pF, K_P = 1$ and $K_I = 8300$ during the bias repeatability test. Table 5-4 presents the bias repeatability test results of the Package #2. Note that, since the bias error of the each test is calculated based on the bias of the first test, bias error values in the first row appears to be zero.

Table 5-4: Bias repeatability performance of the Package #2 with different feedback voltage levels and with and without I-controller.

Package #2	**P Controller**			**PI Controller**		
V_{FB} (V)	**6.62**	**6.93**	**7.33**	**6.62**	**6.93**	**7.33**
Bias Error #1 (mg) (Reference bias)	0.00	0.00	0.00	0.00	0.00	0.00
Bias Error #2 (mg)	-0.38	-0.03	-0.51	-0.06	-0.07	0.35
Bias Error #3 (mg)	-0.36	0.06	-0.73	-0.11	0.02	0.04
Bias Error #4 (mg)	-0.18	-0.07	-0.52	0.01	0.22	0.14
Bias Error #5 (mg)	-0.24	-0.12	-0.83	0.06	0.21	0.24
Bias Error (mg)	**0.27**	**0.07**	**0.59**	**0.06**	**0.14**	**0.20**

With the conducted test, bias repeatability performance of the accelerometer package utilizing PI controller is found to be below 1 mg for all conditions. The purpose of the bias repeatability test is to observe the effect I-controller, since performance of the whole system would be affected by offset drift of the additional I-controller block.

According to the bias repeatability test results given in Table 5-4, the bias repeatability performance of the each configuration is close to each other and randomly varying. Thus, it can be concluded that, there is no apparent effect of additional I-controller block and feedback voltage level on the bias repeatability performance of the accelerometer system.

5.6 Temperature Test

In order to measure the temperature dependency of the accelerometer system, the data acquisition board is placed into the temperature oven. Also, temperature sensor is located near the data acquisition board to perform temperature reading with an Agilent 34401A digital multimeter. The temperature oven is set to sweep from 0 °C to 80 °C with 10 °C steps, and both the acceleration data acquisition and temperature reading are performed at each step using Package #1 and the temperature sensor.

Accelerometer readout circuit is configured to be $K_I = 25000, K_P = 2/3,$ $V_{fb} = 6\,V,\ C_{int} = 5\,pF,\ t_s = 500kHz\ and\ C_{fb} = 0.4\,pF$ and temperature test is conducted for accelerometer system utilizing P-controller and PI-controller separately.

Figure 5-17 shows the bias temperature sensitivity of $792\ \mu g/°C$ for the accelerometer system utilizing PI-controller. Also Figure 5-18 presents the temperature sensitivity of the accelerometer with P-controller as $779\ \mu g/°C$ which is close to the temperature sensitivity of the accelerometer system utilizing PI-controller.

It is worthy to note that the temperature dependent output of the accelerometer system can be easily fitted by the first order linear model. Thus, linear model of the temperature dependent acceleration output can be used for the compensation over the full temperature range.

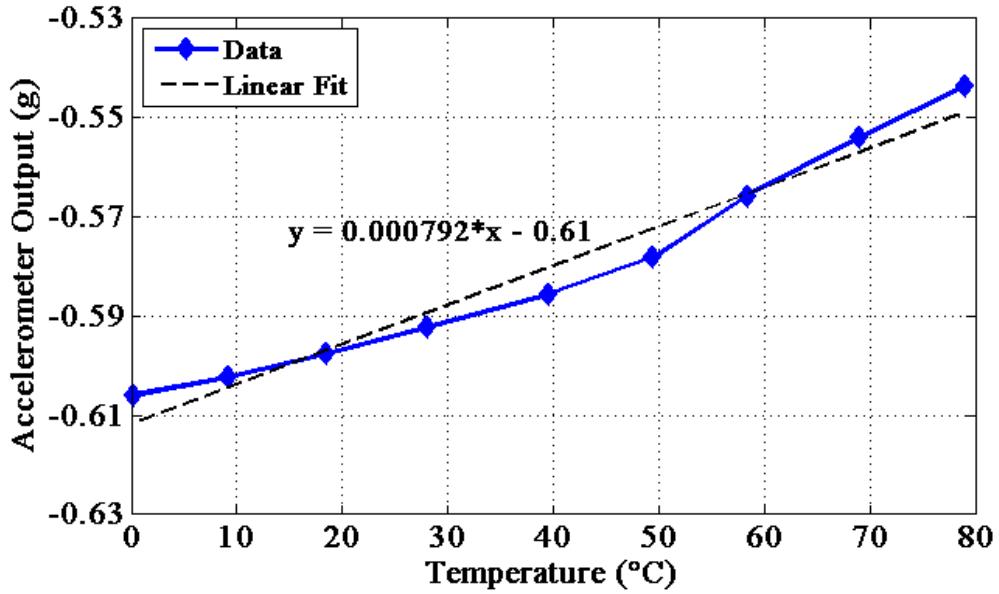

Figure 5-17: Temperature dependent output of the accelerometer system utilizing PI controller. Temperature sensitivity of the output can be extracted as 792 µg/°C using linear fit.

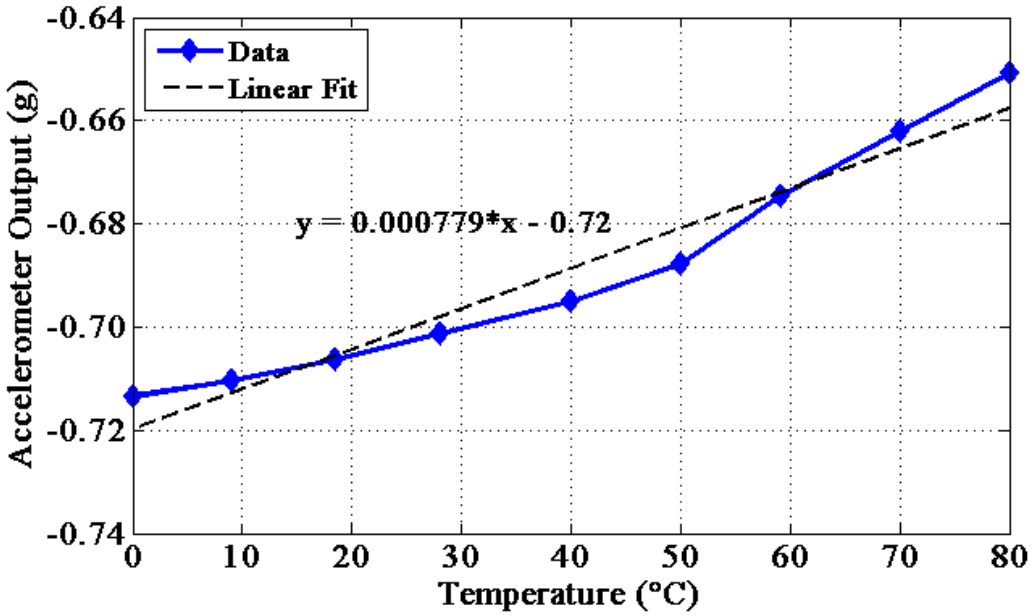

Figure 5-18: Temperature dependent output of the accelerometer system utilizing P controller. Temperature sensitivity of the output can be extracted as 779 µg/°C using linear fit.

5.7 Summary

In this chapter, scale factor stability test result is given to verify the functionality of the implemented readout circuit integrated with the MEMS accelerometer sensor. Also, effectiveness of the I-controller is demonstrated prior to the linearity performance test of the readout circuit with this test.

The main focus in this thesis is to enhance linearity performance of the accelerometer system without degrading other performance parameters. Thus, primarily linearity performance of the accelerometer system is measured with and without I-controller by applying centrifugal acceleration using rate table for the ±3 g input range. It is shown that accelerometer system taking advantage of I-controller improves linearity performance significantly and almost achieves perfect linear system. Best linearity result is obtained with the Package #2 showing 38 ppm and 36 ppm non-linearity for positive and negative input accelerations respectively by improving the non-linearity performance 4 times compared to the accelerometer system without I-controller. Also, 20 times enhancement in the linearity performance is achieved by including I-controller in the loop for the low loop gain configurations.

After proving linearity enhancement of the accelerometer system taking advantage of I-controller, noise, drift, bias repeatability and temperature tests are conducted on the accelerometer system with and without I-controller. All the test results show that linearity improvement is achieved without degrading other performance parameters. White noise floor of 12.5 $\mu g/\sqrt{Hz}$ which is limited by mechanical Brownian noise is obtained for the ±28.8g input range while bias instability is extracted as 5.8 μg. Also, repeatability of the bias and temperature sensitivity of the accelerometer is approximately found to be $0.15\,mg$ and $792\,\mu g/°C$ respectively for the implemented readout circuit utilizing PI-controller.

Apart from these, experimental feedback voltage optimization method is established and suppression of flicker noise is illustrated by using optimum feedback voltage amplitude zeroing effective spring constant for the systems that suffer from high spring constant, high stationary sensor capacitance or parasitic capacitance.

CHAPTER 6

CONCLUSIONS AND FUTURE WORK

The main focus of this thesis is to improve the linearity performance of the electro-mechanical sigma delta accelerometer by including PI controller while keeping other performance parameters such as noise, bias instability, bias repeatability and bias temperature coefficient constant. With the designed readout circuit, 5^{th} order accelerometer system achieves best non-linearity performance as 38 ppm in the ±3 g measurement range for ±28.8 g expected full scale output range. Table 6-1 compares the non-linearity performances obtained in this work with the various accelerometer systems in the literature.

Table 6-1: Non-linearity performance comparison of various accelerometers in the literature.

Accelerometer	**Sensing Mech.**	**Controller**	**Non-Linearity (ppm)**	**Measurement range**	**Full Scale Output**
This Work	Sigma Delta	PI	38	±3 g	±28.8 g
L. Aaltonen [36]	Continuous Time	PID	140	±0.75 g	±1.2 g
Y. Liang [38]	Switched Cap.	PID	500	-	±3 g
Y. Liu [39]	Switched Cap.	PID	600	±1 g	±2 g
T. Smith [35]	Sigma Delta	PD	1500	-	±1 g
H. Xu [40]	Sigma Delta	-	1500	±1 g	±1.2 g
M. Yucetas [37]	Switched Cap.	PD	3300	-0.7 g to +1.4 g	±1.4 g

The implemented 5th order accelerometer system utilizing PI controller is the best accelerometer in the literature in terms of non-linearity. Also, the utilization of the PI controller in an electromechanical sigma-delta modulator is presented in this work, and enhancement in the linearity performance is demonstrated with the test results for the first time in the literature. The additional results of this study can be summarized as follows:

1. Although capacitive MEMS accelerometer sensors are preferable due to their high sensitivity, high reliability and low cost, non-linearity may be serious problem for these sensors. In order to solve this problem and eliminate the force to displacement non-linearity of the sensor, PI controller is implemented and employed in the sigma delta interface circuit in a standard 0.35 µm CMOS technology. PI controller is implemented using capacitor bank which allows the readout circuit to operate with various capacitive MEMS accelerometers independent from mechanical parameters.
2. The designed readout circuit is integrated with the MEMS accelerometer sensor in 16 pin metal package and functionality verification of the package is demonstrated with the scale factor stability tests. Linearity performance test of the packages show that linear operation below 150 ppm can be obtained with the readout circuit employing PI controller independent from mechanical sensor and readout circuit parameters. With the linearity test results, while 4 times enhancement in the linearity is achieved for the high loop gain configuration ($C_{int} = 1pF$) , improvement in the linearity increased up to 20 times for low loop gain configuration ($C_{int} = 9pF$) for Package #2. Also remember that linearity measurements are performed for the ±3 g input acceleration range due to the angular velocity limit and diameter of rate table.
3. In order to evaluate the performance of the readout circuit with and without I-controller, noise, bias drift, bias repeatability and temperature tests are conducted. Noise and bias instability of the accelerometer system is measured approximately as 12.5 $\mu g/\sqrt{Hz}$ which is limited with the mechanical Brownian noise and 5.8 μg respectively for ±28.8 g input range by employing I-controller in the loop. Also, while turn on/off bias repeatability of the system is extracted below 1 mg, bias temperature coefficient is found

to be approximately $800\ \mu g/°C$ when the I-controller is utilized. Similar results are observed for the accelerometer system without I-controller. These results prove that linearity of the accelerometer is significantly improved without sacrificing from other performance parameters.

4. In order to achieve low noise and bias instability performance with the mechanical sensor utilizing high parasitic capacitance and high spring constant, importance of the feedback voltage is emphasized and experimental feedback voltage optimization method is described. Enhancement in the bias instability performance of the accelerometer is demonstrated by adjusting suitable feedback voltage amplitude and intentionality disabling correlated sampling feature of front-end amplifier to increase flicker noise level. Bias instability of the accelerometer is decreased to $6.9\ \mu g$ from $18\ \mu g$ although the input acceleration range is increased from ±29.8g to ±37.1g with the help of feedback voltage optimization. Since overall input-referred noise is dominated by the mechanical Brownian noise, enhancement in the electronic noise performance could not be demonstrated with this test.
5. The dedicated test setup for linearity tests of the accelerometer is developed at METU using rate table. Since, transfer of digital accelerometer data to PC is not possible due to the slip rings of the rate table, FPGA code is prepared to store acceleration data in the SDRAM utilized in the commercial FPGA board during the linearity test. C++ code is written to transfer stored acceleration data to the PC. Also, bias repeatability test are automated by controlling power supply and start-up sequence of the accelerometer with the code written in C++.

Major achievement of this thesis is the demonstration of linearity improvement of the varying gap type MEMS accelerometer by utilizing PI controller in the sigma delta readout circuit. However there are still some performance parameters that need to be improved further. Bias instability, long term bias stability, bias temperature coefficient, scale factor temperature coefficient and bias repeatability of the accelerometer are the important parameters to consider for various applications that target navigation grade performance.

Thus, research topics can be listed as follows in order to enhance aforementioned important performance parameters:

1. Integration of the MEMS accelerometer and readout circuit in a hybrid package is critical issue. Adhesives which are used during the packaging of the components may pose significant amount of stress on the mechanical sensor and readout circuit resulting in degraded bias repeatability and long term stability performance. Thus, simulations should be conducted to explore the effects of the packaging related stress and suitable packaging method and adhesive should be chosen.
2. Temperature compensation should be performed with the on-chip circuit or post processing in order to eliminate the effect of the temperature on the scale factor and accelerometer bias.
3. Since noise and drift on the feedback voltage directly contributes to overall noise, bias instability and long term stability performance of accelerometer, this voltage source can be integrated within the CMOS readout circuit by designing a high performance DC-DC regulator.
4. With the current CMOS readout circuit, it is not possible to damp the accelerometer sensor inside vacuum environment due to the mechanical resonance peak even in closed loop operation. Derivative controller can be implemented to suppress mechanical resonance and obtain stable operation with reduced Brownian noise floor.
5. Scale factor temperature coefficient is an important parameter to achieve navigation grade performance. Thus, temperature dependency of scale factor can be evaluated by establishing a proper test setup.

REFERENCES

[1] History of the transistor (the "Crystal Triode"). The porticus Centre. Phoenix, Az, USA. Available online: http://www.porticus.org/bell/belllabs_transistor.html (accessed on 28 June 2015).

[2] Yole Development Market Research and Strategy Development Company, "Status of the MEMS Industry 2015," Available online: http://www.i-micronews.com/images/Flyers/MEMS/Yole_Status_of_the_MEMS_Industry_April_2015_web.pdf (accessed on 28 June 2015).

[3] SAFRAN Colibrys, "Single Axis Analog Accelerometer," MS9000 datasheet, 2015.

[4] Honeywell, "Q-Flex QA-2000 Accelerometer," QA2000-030 datasheet, 2005.

[5] Innalabs, "Quartz Accelerometer," Al-Q-2001 datasheet, 2015.

[6] J. Chae, H. Kulah, and K. Najafi, "Hybrid Silicon-On-Glass (SOG) Lateral Micro-Accelerometer with CMOS Readout Circuitry," The 15th IEEE International Conference on Micro Electro Mechanical Systems (MEMS '02), pp. 623-626, Las Vegas, NV, USA, Jan. 2002

[7] B. V. Amini, R. Abdolvand, and F. Ayazi, "Sub-Micro-Gravity Capacitive SOI Microaccelerometers," Proceedings of the International Conference on Solid State Sensors, Actuators and Microsystems (Transducers '05), pp. 515-518, June 2005.

[8] M. A. Lemkin, M. A. Ortiz, N. Wongkomet, B. E. Boser, and J. H. Smith "A 3-Axis Surface Micromachined ΣΔ Accelerometer," International Solid-State Circuits Conference, pp. 202-203, Feb. 1997.

[9] A. M. Marcus, T. D. Nghia, and C. G. James, "Die Attach Stress Isolation," US8803262 B2, August 2012.

[10] D. Bertrand, B. Sophie, S. Michel, and D. Yves, "Microelectromechanical System," US7170140 B2, Jan. 2007.

[11] L. M. David, "Accelerometer Strain Isolator," US6634231 B2, Oct. 2003.

[12] M. Ali, "Correction of Temperature and Acceleration Effects on MEMS Gyro Output Signals," M.Sc. Thesis, Middle East Technical University, December 2014.

[13] Y. Jeong and F. Ayazi, "A Novel Offset Calibration Method to Suppress Capacitive Mismatch in MEMS Accelerometer," The 9th Samsung ElectroMechanics '1nside Edge', Suwon, Korea, Nov. 2013.

[14] P. Lajevardi, V, P. Petkov, and B. Murmann, "A ΣΔ Interface for MEMS Accelerometers using Electrostatic Spring-Constant Modulation for Cancellation of Bondwire Capacitance Drift," IEEE International Solid-State Circuits Conference, pp. 196-198, Feb. 2012.

[15] C. Lang, V. Petkov and U. Gomez, "Cancelling Low Frequency Errors in MEMS Systems," US7786738 B2, August 2010.

[16] IEEE Standard for Inertial Sensors Terminology, IEEE Std 528-2001, November 2001.

[17] N. Yazdi, F. Ayazi, and K. Najafi, "Micromachined Inertial Sensors," Proceedings of the IEEE, Vol. 86, No. 8, pp. 1640-1659, August 1998.

[18] U. Sönmez, "Capacitive CMOS Readout for High Performance MEMS Accelerometers," M.Sc. Thesis, Middle East Technical University, Feb. 2011.

[19] W. Henrion, L. DiSanza, M. Ip, S. Terry, and H. Jerman, "Wide Range Direct Digital Accelerometer," IEEE Solid-State Sensor and Actuator Workshop, pp. 153, June 1990.

[20] C. Lu, M. Lemkin, and B. E. Boser, "A Monolithic Surface Micromachined Accelerometer with Digital Output," IEEE International Solid-State Circuits Conference, pp. 160-161, Feb. 1995.

[21] J. Wu, G. K. Fedder, and L. R. Carley, "A Low-Noise Low-Offset Capacitive Sensing Amplifier for a 50-μ$g/\sqrt{Hz}$ Monolithic CMOS MEMS Accelerometer," Journal of Solid State Circuits, Vol. 39, Issue 5, pp. 722-730, May 2004.

[22] V. P. Petkov and B. E. Boser, "A Fourth Order ΣΔ Interface for Micromachined Inertial Sensors," Journal of Solid State Circuits, Vol. 40, Issue 8, pp. 1602-1609, August 2005.

[23] H. Kulah, J. Chae, N. Yazdi, and K. Najafi, "Noise Analysis and Characterization of a Sigma-Delta Capacitive Microaccelerometeer," Journal of Solid State Circuits, Vol. 41, Issue 2, pp. 352-361, Feb. 2006.

[24] J. Raman, E. Cretu, P. Rombouts, and L. Weyten, “An Unconstrained Architecture for Systematic Design of Higher Order ΣΔ Force Feedback Loops,” IEEE Transactions on Circuits and Systems, Vol. 9, Issue 3, pp. 297-305, March 2009.

[25] STMicroelectronics, “High Performance Ultra Low Power 3-Axis Accelerometer with Digital Output for Industrial Applications,” IIS328DQ datasheet, April 2015.

[26] Analog Devices, “Precision, ±5 g, Dual Axis, High Temperature iMEMS Accelerometer,” ADXL206 datasheet, 2011.

[27] Bosch, “Digital Triaxial Acceleration Sensor,” BMA280 datasheet, August 2014.

[28] Y. Dong, P. Zwahlen, A. M. Nguyen, F. Rudolf, and J. M. Stauffer, “High Performance Inertial Navigation Grade Sigma-Delta MEMS Accelerometer,” IEEE Position Location and Navigation Symposium (PLANS), pp. 32-36, May 2010.

[29] Y. Dong, P. Zwahlen, A. M. Nguyen, R. Frosio, and F. Rudolf, “Ultra-High Precision MEMS Accelerometer,” International Conference on Solid State Sensors, Actuators and Microsystems (Transducers ’11), pp. 695-698, June 2011.

[30] P. Zwahlen, Y. Dong, A. M. Nguyen, F. Rudolf, J. M. Stauffer, P. Ullah, and V. Ragot, “Breakthrough in High Performance Inertial Navigation Grade Sigma-Delta MEMS Accelerometer,” IEEE Position Location and Navigation Symposium (PLANS), pp. 15-19, April 2012.

[31] F. Rudolf, S. Gonseth, R. Brisson, and P. Krebs, “New Generation of Hogh Performance/High Reliability MEMS Accelerometers for Harsh Enviroment,” IEEE Position Location and Navigation Symposium (PLANS), pp. 7-11, May 2014.

[32] Y. Dong, M. Kraft, and W. R. White, “Higher Order Noise Shaping Filters for High Performance Micromachined Accelerometers,” IEEE Trans. on Instrumentation and Measurement, Vol. 56, Issue 5, pp. 1666-1674, October 2007.

[33] G. K. Fedder and R. T. Howe, “Multimode Digital Control of a Suspended Polysilicon Microstructure,” Microelectomechanical Systems, Vol. 5, Issue 4, pp. 283-297, December 1996.

[34] Y. Terzioglu, S. E. Alper, K. Azgin, and T. Akin, “A Capacitive MEMS Accelerometer Readout with Concurrent Detection and Feedback Using Discrete Components,” IEEE Position Location and Navigation Symposium (PLANS), pp. 12-15, May 2014.

[35] T. Smith, O. Nys, M. Chevroulet, Y. DeCoulon, and M. Degrauwe, “A 15 b Electromechanical Sigma-Delta Converter for Acceleration Measurements,” Solid-State Circuits Conference, pp. 160-161, February 1994.

[36] L. Aaltonen and K. Halonen, “Continuous-time Interface for a Micromachined Capacitive Accelerometer with NEA of 4μg and Bandwidth of 300 Hz,” Sensors and Actuators A: Physical, Vol. 154, Issue 1, pp. 46-56, August 2009.

[37] M. Yucetas, J. Salomaa, A. Kalanti, L. Aaltonen, and K. Halonen, “A Closed Loop SC Interface for a ±1.4g Accelerometer with 0.33% Nonlinearity and 2μ $g/\sqrt{Hz}$ Input noise Density,” Solid-State Circuits Conference, pp. 320-321, February 2010.

[38] Y. Liang, L. Xiaowei, C. Weiping, and Z. Zhiping, “High Resolution Interface Circuit for Closed Loop Accelerometer,” Journal of Semiconductors, Vol. 32, Issue 4, April 2011.

[39] Y. Liu, Y. Wang, S. Gao, and L. Shao, “A Low Noise CMOS Interface ASIC for Capacitive MEMS Accelerometer,” International Conference on Mechatronic Science, Electric Engineering and Computer, pp. 438-441, August 2011.

[40] H. Xu, X. Liu, and L. Yin, “A Closed Loop ΣΔ Interface for a High-Q Micromechanical Capacitive Accelerometer with $200\,ng/\sqrt{Hz}$ Input Noise Density,” Journal of Solid-State Circuits, Vol. 50, Issue 9, pp. 2101-2112, September 2015.

[41] H. Inose, Y. Yasuda and J. Marakami, “A Telemetering system by Code Modulation, Delta-Sigma Modulation,” IRE Transaction on Space Electronics and Telemetry, Vol. SET-8, Issue 3, pp. 204-209, Sept. 1962.

[42] R. Schreier and G. Temes, “Understanding Delta-Sigma Data Converters,” IEEE Press Piscataway, NY, 2005.

[43] I. E. Ocak, “Tactical Grade MEMS Accelerometer,” PhD. Thesis, Middle East Technical University, 2010.

[44] W. L. Lee, “A Novel Higher Order Interpolative Modulator Topology for High Resolution Oversampling A/D Converters,” M.Sc Thesis, Massachusetts Institute of Technology, Cambridge, MA, 1987.

[45] Burak Eminoğlu, “Weekly Progress Report be110724,” Vol. 135, Middle East Technical University, 2011.

[46] O. S. Incedere, “A Low Power Capacitive Integrated CMOS Readout Circuitry for High Performance MEMS Accelerometer,” M.Sc. Thesis, 2013.

[47] K. Ogata, “Modern Control Engineering,” Prentice Hall, NJ, 2009.

[48] R. Gregorian, “High Resolution Switched Capacitor D/A Converter,” Journal of Microelectronics, Vol. 12, Issue 2, pp. 10-13, April 1981.

[49] K. S. Kundert, “Simulating Switched-Capacitor Filters with SpectreRF,” Designer’s Guide Consulting Inc., Available online: http://www.designers-guide.org/analysis/sc-filters.pdf (accessed on 28 June 2015).

[50] Tunjar Askarli, “Weekly Progress Report ta111023,” Vol. 49, Middle East Technical University, 2011.

[51] Linear Technologies, “LT1762 Series 150 mA, Low Noise, LDO Micropower Regulators,” LT1762 datasheet, 1999.

[52] IEEE Standard Specification Format Guide and Test Procedure for Linear Single-Axis, Non-Gyroscopic Accelerometers, IEEE Std. 1293-1998 (R2008), Dec. 2008.

[53] IEEE Standard Specification Format Guide and Test Procedure for Single-Axis Interferometric Fiber Optic Gyros, IEEE Std. 952-1997 (R2008), Dec. 2008.